UNIVERSITY OF STRATHCLYDE
DEPARTMENT OF PHYSICS

On Mechanisms of Laser-Coupling to Fast Electrons in Ultraintense Laser-Solid Interactions

by

Ross J. Gray

in partial fulfilment of the requirements for the degree of Doctor of Philosophy in Physics

2013

Copyright Declaration

Signed:

Date:

Abstract

This thesis reports on experimental investigations of the interaction of intense ($> 10^{18}$ W/cm^2) laser pulses with solid density targets. This interaction has been known for many years to generate high energy (fast) electrons, ions, x-rays and γ-rays as well as powerful shock waves and gigagauss magnetic fields. Proposed applications for such interactions include their implementation as a compact source of high energy ions to be used in the treatment of cancers and as a source of high energy electrons to induce the necessary high energy-density conditions required to achieve nuclear fusion, therefore acting as a new, clean energy source. For both applications the process of electron generation via the absorption of the laser pulse is critical and is required to be as efficient as possible, either for ion acceleration in order to reach the highest ion energies or for laser driven nuclear fusion in order to maximise energy gain of the reaction. The work in this thesis seeks to address some of these issues by investigating the processes of electron generation and the key parameters which can be controlled to optimise such processes.

Across three different experiments, by modifying parameters such as laser incidence angle, plasma density profile, laser polarisation, target thickness and laser intensity, control over fast electron generation process is demonstrated. In the first of these experiments spatial control over the electron generation is demonstrated. Large laser incidence angles are used to drive fast electrons along the target surface as opposed to the along the laser axis direction using the growth of strong quasi-static electric and magnetic fields which form on the target surface. In the second experiment a controlled plasma density gradient is used to enhance the coupling efficiency of the laser into high energy electrons. This enhancement

is demonstrated by both experimental results and in simulations. The simulations show that the enhancement is driven by self-focusing in the underdense region of the plasma density profile, an effect which becomes less effective at longer density scale lengths due to the onset of laser filamentation. In the final experiment an enhancement in electron generation is demonstrated due to the onset of relativistic induced transparency (RIT). Both experimentally and in simulations the onset of this process is shown to be sensitive to target thickness, laser intensity and polarisation. With the correct combination of these three parameters RIT occurs, resulting in an enhancement of over an order of magnitude in accelerated electron numbers.

Acknowledgements

I would suggest that, unfortunately, the majority of people go through life never knowing what it is they really would like to do. For these people a job is just a job and Monday to Friday is that unpleasant gap reminding them what a weekend is for. For a lucky few however, and I would include myself in this group, we find a passion, a calling. The work is not just what we do but who we *are*. Research, the development of new technologies and the prospect of revealing new, fundamental laws of nature is, for me, just such a calling. The pursuit of such work would be impossible alone.

The completion of this thesis and the work presented within, could not have been possible without the help and support of a number of people. I would first like to thank my supervisor, Paul McKenna, for his continued encouragement and support. He has encouraged me to explore new ideas, even initially flawed ones, simultaneously enabling me to develop my skills as a scientist and demonstrating what it means be one. I would also like to thank David Carroll and Xiaohui Yuan, from whom I have learned more than I could easily relate in this short passage. I would additionally like to thank Mark Quinn, Olivier Tresca, David MacLellan, Haydn Powell and Mireille Coury. I could not have hoped for better colleagues to work with on a daily basis. Thanks also goes to all of the staff at the Central Laser Facility, without their dedication and professionalism the work enclosed would simply not be possible.

Finally I would like to give thanks to all of my family. In particular my parents, Pauline and James, and my brother Simon. Without their scarifies, their continued support and encouragement I would certainly not be here. My grandparents once gave me a book, inside the front cover they had written a

phrase, the origin of which is disputed, “stand for something or you will fall for anything”. With their help, the others acknowledged here and others who are not, I found something to stand for. The pages which follow attempt to demonstrate this.

Role of Author

The author analysed the majority of the data presented in this thesis, had a leading role in both planning and executing all experiments and contributed to writing to all of the publications resulting from the data presented herein.

Chapter 5: The author played a leading role in planning and executing this experiment (as deputy TAO). The image plate was scanned by M. Coury and prepared by O. Tresca. The experiment was setup by the author and D.C Carroll, who was TAO and took the lead on lining up targets. X.H Yuan aided planning and initial design as well as initial data analysis. The author developed the analysis software for the main diagnostic, as well as performing the analysis itself. The proton maximum energy cut-off energy model was adapted from a model originally written by M.N Quinn.

Chapter 6: The author played a significant role in planning and executing this experiment. Image plates were scanned by the author as well as contributing to the experimental setup. D.C Carroll and X.H Yuan took the lead role in the execution of this experiment. The data analysis was performed by both the author and X.H Yuan. Hydrodynamic and PIC modelling was the lead by the author. Visualisation software for both types of modelling was developed by the author.

Chapter 7: The author played a leading role in the planning, design and execution of this experiment (as deputy TAO). The author and P. McKenna developed the initial concept of the MuSE detector. The author had a leading role in developing an initial prototype design of this diagnostic. During the experiment the author took a lead role in the setup and execution as well as

preliminary analysis. Further analysis and the development of analysis software was also carried out by the author. The author had a leading role in setting up and executing EPOCH on a new HPC cluster at Strathclyde.

Publications

1. **Surface transport of energetic electrons in intense picosecond laser-foil interactions**

   R. J. Gray, X. H. Yuan, D. C. Carroll, C. M. Brenner, M. Coury, M. N. Quinn, O. Tresca, B. Zielbauer, B. Aurand, V. Bagnoud, J. Fils, T. Kuehl, X. X. Lin, C. Li, Y. T. Li, M. Roth, D. Neely and P. McKenna, *Appl. Phys. Lett.* **99**, 171502 (2011)

2. **Enhanced Laser-to-Electron Energy Coupling in Solid Density Plasmas Using a Controlled Plasma Density Gradient**

   R.J. Gray, X.H. Yuan, D.C. Carroll, C.M. Brenner, M. Burza, M. Coury, K.L.Lancaster, X.X. Lin, Y.T. Li, M.N. Quinn, O.Tresca, C.-G. Wahlström, D. Neely, and P. McKenna (in preparation)

3. **Laser absorption to fast electrons in the transition to the relativistic induced transparency regime**

   R.J Gray, H. Powell, D.C Carroll, D.A Maclellan, G.S Scott, N. Booth, C.D Murphy, C.S Brady, C.P Ridgers, D. Neely and P. McKenna (in preparation)

4. **The effect of low temperature resistivity evolution on fast electron transport through warm dense matter**

   D. A. MacLellan, A. P. L. Robinson, D .C. Carroll, R. J. Gray, H. Powell, N. Booth, G. G. Scott, X. H. Yuan, D. Fei, M. Burza, C.-G. Wahlstrm, D.

Neely, M. P. Desjarlais and P. McKenna (in preparation)

5. **Fast electron transport patterns in intense laser-irradiated solids diagnosed by modeling measured multi-MeV proton beams**

   D. A. MacLellan, D .C. Carroll, R. J. Gray, N. Booth, B. Gonzalez-Izquierdo, H. Powell, G. G. Scott, D. Neely and P. McKenna (at press)

6. **The influence of proton isochoric heating on fast electron transport in ultraintense laser solid interactions**

   D. A. MacLellan, A. P. L. Robinson, D .C. Carroll, R. J. Gray, H. Powell, N. Booth, G. G. Scott, X. H. Yuan, D. Fei, M. Burza, C.-G. Wahlstrm, D. Neely, M. P. Desjarlais and P. McKenna (in preparation)

7. **Exotic dense matter states pumped by relativistic laser plasma in the radiation dominant regime**

   J. Colgan, J. Abdallah, Jr, A. Ya. Faenov, S. A. Pikuz, E. Wagenaars, N. Booth, O. Culfa, R. J. Dance, R. G. Evans, R. J. Gray, T. Kaempfer, K. L. Lancaster, P. McKenna, A. L. Rossall, I. Yu. Skobelev, K. S. Schulze, I. Uschmann, A. G. Zhidkov, and N. C. Woolsey (in preparation)

8. **Injection and transport properties of fast electrons in ultraintense laser-solid interactions**

   M. Coury D. C. Carroll, A.P.L. Robinson, X. H. Yuan, C. M. Brenner, M.Burza, R. J. Gray, K. L. Lancaster, Y. T. Li, X. X. Lin, D. A. MacLellan, H. Powell, M. N. Quinn,1 O. Tresca, C.-G. Wahlström, D. Neely, and P. McKenna (submitted *Phys. Plasmas* 2013)

9. **Effect of Lattice Structure on Energetic Electron Transport in Solids Irradiated by Ultraintense Laser Pulses**

   P. McKenna, A. P. L. Robinson, D. Neely, M. P. Desjarlais, D. C. Carroll, M. N. Quinn, X. H. Yuan, C. M. Brenner, M. Burza, M. Coury, P. Gallegos,

R. J. Gray, K. L. Lancaster, Y. T. Li, X. X. Lin, O. Tresca, and C.-G. Wahlström, *Phys. Rev. Lett.* **106**, 185004 (2011)

10. **Refluxing of fast electrons in solid targets irradiated by intense, picosecond laser pulses**

    M N Quinn, X H Yuan, X X Lin, D C Carroll, O Tresca, R J Gray, M Coury, C Li, Y T Li, C M Brenner, A P L Robinson, D Neely, B Zielbauer, B Aurand, J Fils, T Kuehl and P McKenna, *PPCF* **53**, 025007 (2011)

11. **Controlling the properties of ultraintense laser-proton sources using transverse refluxing of hot electrons in shaped mass-limited targets**

    O. Tresca, D. C. Carroll,X. H. Yuan, B. Aurand, V. Bagnoud, C. M. Brenner, M. Coury, J. Fils, R. J. Gray, T. Kuehl, C. Li, Y. T. Li, X. X. Li, M. N. Quinn, R. G. Evans, B. Zielbauer, M. Roth, D. Neely and P. McKenna, *PPCF* **53** 105008 (2011)

12. **Controlling fast-electron-beam divergence using two laser pulses**

    R. H. H. Scott1, C. Beaucourt, H.-P. Schlenvoigt, K. Markey, K. L. Lancaster, C. P. Ridgers, C. M. Brenner, J. Pasley, R. J. Gray, I. O. Musgrave, A. P. L Robinson, K. Li, M. M. Notley, J. R. Davies, S. D. Baton, J. J. Santos, J.-L. Feugeas, Ph. Nicola, G. Malka, V. T. Tikhonchuk, P. McKenna, D. Neely, S. J. Rose and P. A. Norreys, *Phys. Rev. Lett.* **109**, 015001 (2012)

13. **Influence of laser irradiated spot size on energetic electron injection and proton acceleration in foil targets**

    M. Coury, D. C. Carroll, A. P. L. Robinson, X. H. Yuan, C. M. Brenner, M. Burza, R. J. Gray, M. N. Quinn, K. L. Lancaster, Y. T. Li, X. X. Lin, O. Tresca, C.-G. Wahlström, D. Neely, and P. McKenna, *Appl. Phys. Lett.* **100**, 074105 (2012)

14. **Spatially resolved X-ray spectroscopy using a flat HOPG crystal**

    X.H. Yuan, D.C. Carroll, M. Coury, R.J. Gray, C.M. Brenner, X.X. Lin, Y.T. Li, M.N. Quinn, O. Tresca, B. Zielbauer, D. Neely, P. McKenna, *Nuclear Instruments and Methods* **653**(1) pp145-149 (2011)

Contents

List of Figures

List of Tables

Chapter 1

Introduction

The conceptions of nature which we call "physics" are a product of two factors. The first, is the accumulated facts and knowledge built up over previous generations. The second is the method used to develop this knowledge. Where hypothesis and experiment are implemented to test a previously held understanding to it's limits, to take it as far as it will go. The process of gaining new knowledge does not necessarily come from understanding when something is true. Instead, only when our understanding breaks down do we gain the deepest insights into the physical underpinnings of nature. In the words of T.S Elliot "only those who will risk going too far can possibly find out how far one can go".

I will not speculate whether this sentiment was in the mind of Theodore Maiman when he built the first laser over fifty years ago [1]. Nevertheless, his discovery is increasingly used as a way to drive matter into extreme states never before created on this planet. As the achievable intensity of lasers increase, the theory of how matter behaves at high temperatures and densities continues to be revised and refined. The properties, processes and dynamics of matter compelled into this state by short pulse, high intensity lasers is the subject of this thesis.

The inherent properties of lasers are near ideal as a driver for investigating high energy density physics as laser light is naturally monochromatic, highly directional and can easily be tightly focused. The result is a non-thermal source of radiation with a low input energy which can be focused to produce extremely high energy densities. Through various developments in laser technology the

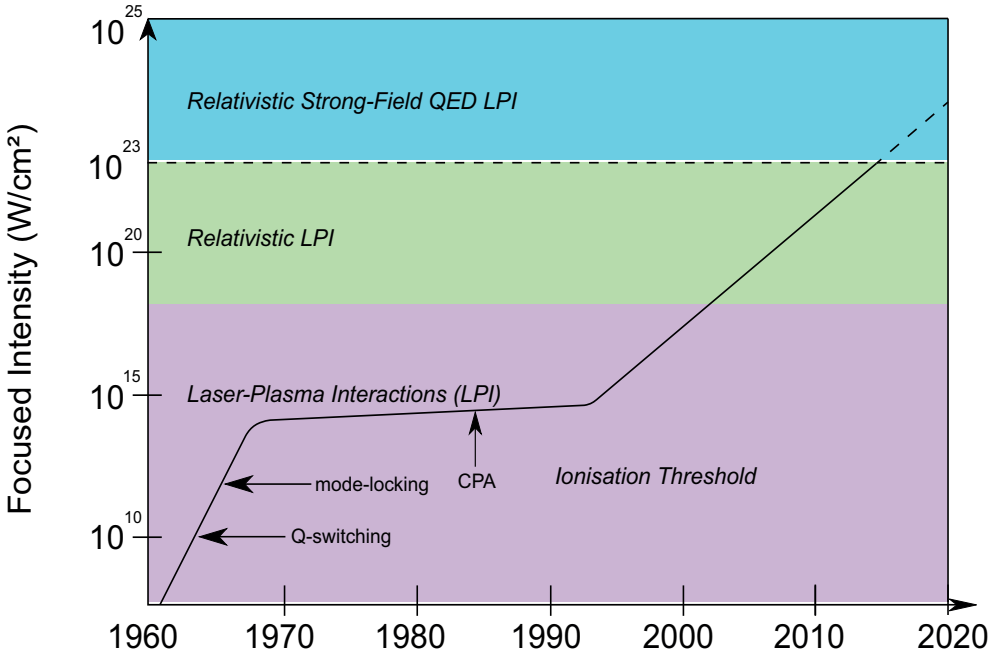

Figure 1.1: Increase in peak laser intensity since 1960

achievable laser power has increased to the point where intensities beyond 10^{21} W/cm^2 are readily achievable (see figure 1.1). In the interaction with matter such high laser intensities produce record breaking magnetic and electric field strengths, beams of relativistic electrons, high energy ion beams and intense x-ray, gamma-ray and neutron emission. All of these products of the interaction can be easily measured. However, controlling the process in such a way that useful sources of radiation are generated is the challenge.

Great strides of progress have been made in this area in recent years and realistic, achievable applications of major significance should be realised within a lifetime. Two fields in particular, which serve as the motivation for this thesis, have garnered great interest in the past decade. Namely laser-driven ion acceleration and the fast-ignition (FI) approach to inertial confinement fusion (ICF). Both will be covered in more detail in the following section.

1.1 Laser-Solid Interactions: An Historical Context

This field of physics lies at such a broad intersection of other fields - from laser physics, plasma, atomic, material and nuclear - that it is difficult to define a true starting point. However, it would be fair to say that a seminal moment occurred in 1972 when Nuckolls *et al.* [2] published their paper proposing the use of intense laser beams to compress a pellet containing deuterium and tritium, in the aim of meeting the requirements of the Lawson criterion [3] and thus achieving nuclear fusion - a technique which has since been called inertial confinement fusion (ICF). The scheme relies on the uniform irradiation of a spherical fuel pellet using multiple laser pulses at intensities of $\sim 10^{14}$ W/cm^2. In this approach, the laser energy (at UV or X-ray wavelengths, in order to minimise fast electron generation and maximise absorption) is absorbed by the pellet, resulting in extremely high temperatures, pressures and an expanding coronal plasma. Consequently, the outer shell of the fuel pellet is accelerated inward, in a manner reminiscent of rocket propulsion, resulting in extremely high pressures and temperatures at the target core. If the compression is highly uniform in both space and time then the predicted conditions are sufficient for fusion reactions to be initiated. Importantly, the pulse length of the lasers suggested for this application were nanoseconds in duration and therefore the laser-plasma interaction was dominated by the hydrodynamic motion of the plasma. In a sense, this was the downfall of this initial attempt at this scheme as it proved to be highly susceptible to the growth of hydrodynamic instabilities which acted against the uniform compression of the fuel pellet. Out of necessity more advanced schemes to achieve ICF energy were developed.

It was not until over a decade later with the invention of the Chirped Pulse Amplification (CPA) technique [4] that a major departure from the nanosecond, hydrodynamics dominated laser-plasma interaction took place. CPA enabled the amplification and compression of otherwise long, low energy laser pulses without exceeding the damage threshold of either the laser optics or the gain medium. For

the first time this enabled very short (<1 ps) and high energy (up to 100's of J) laser pulses with intensities exceeding 10^{18} W/cm^2 to be created. The implications for laser-plasma interactions were revolutionary for two reasons. First, electrons ponderomotively accelerated by the laser field would have relativistic velocities at such intensities (henceforth called "fast electrons") and as a result the effect of the Lorentz factor on the plasma dynamics and, importantly, the laser pulse propagation through the plasma was now a consideration. The second major implication was that the interaction was now so short that the plasma expansion at the rising edge of the pulse was minimal and the interaction occurred with a target which was either at critical density or was overcritical. The condition of having a very small region of underdense plasma has interesting implications for the way that energy was transferred to electrons given that the laser could not directly interact with the majority of the plasma. To date there is significant disagreement about the processes occurring directly at the interaction region of the target, addressing this key physics is the focus of this thesis.

Such interactions, now being capable of generating fast particles, garnered increasing amounts of interest as compact sources of fast particles. As it was twenty years earlier with nanosecond laser-plasma interactions, a seminal moment for short pulse interactions was centered around the potential of ICF. In 1994 Tabak *et al.* [5] described a novel scheme for inertial confinement fusion using a combination of both short and long pulse lasers which has subsequently been named fast ignition (FI). This scheme is presented in three phases. First a deuterium-tritium fuel capsule is compressed by direct irradiation using nanosecond pulses of laser light surrounding the target, assembling the fuel into a high density configuration. Second, a short laser pulse with intensity >10^{18} W/cm^2 is fired into the expanding plasma now surrounding the fuel pellet. In the intense laser field electrons oscillate with relativistic velocities. As such the electron mass increases by a factor gamma, the Lorentz factor and the plasma frequency (the oscillations per unit time completed by the plasma electrons) decreases similarly. The result is to increase the critical density, the density at which the plasma frequency is equal to the laser frequency, allowing the laser to propagate further into

the plasma than would otherwise be possible. In the third phase, the laser reaches a plasma density beyond which it can no longer propagate - the relativistically corrected critical density - and is absorbed, generating a beam of fast electrons. The electrons accelerated from the critical density surface then deposit their energy in the high density core raising it to the ≈5 keV temperature required for ignition (see Fig.1.2).

This approach (FI), as compared to central hot spot igniton (CHS), has a number of key advantages. Principally the gain is predicted to be significantly higher in the case of fast ignition. This is due to the change in drive energy. Since no central hot spot is required the implosion velocity and therefore the compression drive can be reduced. The requirement for the absorbed energy of the heating beam is ≈20 kJ delivered in a radius of ≈20 μm on times scales of ≈ 20 ps. A petawatt scale laser is therefore required. The compression laser drive is on the order of ≈200 kJ, which compares favourably with the megajoule scale lasers required for CHS. Typical gains of up to 1000 are expected for the FI approach.

In the years following the publication of Tabak *et al.* [5], and as high power petawatt-class laser systems came on-line, the feasibility of the electron generation phase of this scheme was tested experimentally. Initial experimental evidence suggested that the fast electron beam should be collimated. For example, the experimental results of Borghesi *et al.* [6] demonstrated, by optical probing of glass targets, that well collimated channels of electrons propagate through the target. Work by Davies *et al.* [7], Bell and Kingham [8] and others also showed via numerical simulations that, given the right conditions, beam collimation mediated by the self-induced magnetic field should be expected for intensities exceeding 10^{19} W/cm^2. However later experimental results including those of Santos *et al.*[9], Lancaster *et al.* [10], Stephens *et al.* [11], Yuan *et al.* [12] and Green *et al.* [13] , using various techniques, demonstrate divergence angles actually exceed 30° for the laser intensities required for fast ignition. It is now widely accepted that the fast electron beam is initially highly divergent. If the fast electron divergence is large and the stand off distance, the distance from the electron source to the hot

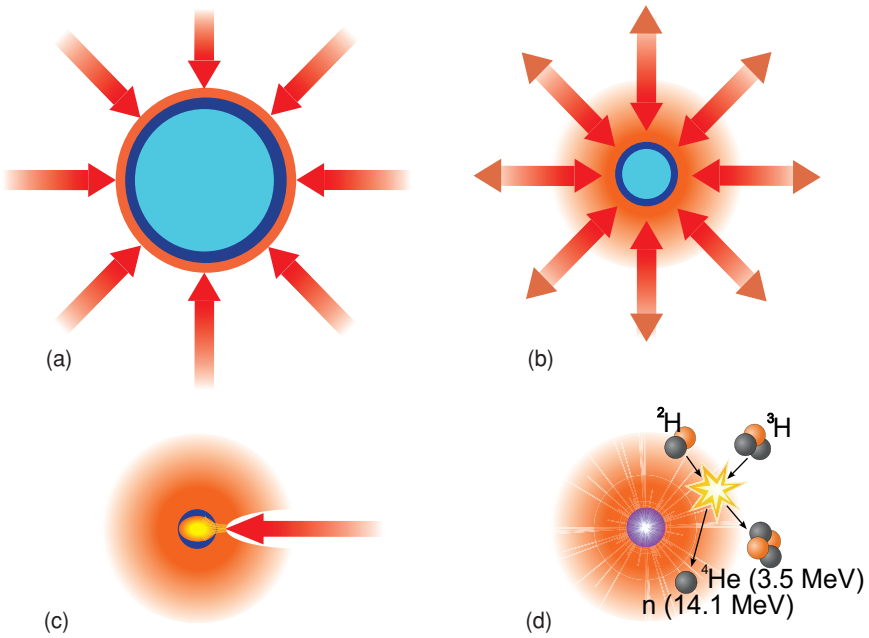

Figure 1.2: Phases of the FI scheme: (a) Initial target ablation with nanosecond laser pulses. (b) The resulting compression of the fuel pellet. (c) Short pulse laser penetrates through the coronal plasma, accelerating electrons at the critical surface. (d) Fast electrons heat the fuel core to ignite the fuel. The resulting alpha particles then propagate a "burn wave" through the target, consuming the majority of the fuel in subsequent fusion reactions.

spot, is also large then the energy coupling to the fusion reaction will be poor for purely geometrical reasons. Achieving ignition with any reasonable gain under these circumstances is then put beyond reach.

A number of avenues have been explored over the past decade or more to compensate for the intrinsic electron beam divergence. One approach is to change the stand off distance by increasing the laser intensity so that the effective critical density is increased, due to the relativistic transparency effect described earlier, thereby enabling the beam to propagate further into the plasma. The major issue with this approach, even from the very early suggestion, was the difficulty in keeping the resulting channel clear of the blow-off plasma during the compression of the fuel pellet and the susceptibility of the beam to instabilities as it propagates through the plasma.

An inventive approach along similar lines is the use of a hollow gold cone which is attached to the fuel pellet. The short pulse laser is then fired into the gold cone, avoiding the coronal plasma altogether [14]. The fast electron beam

is instead generated in the interaction of the laser with the cone tip. An image of the proposed target design is shown in Fig.1.3. By avoiding the interaction with the plasma and enabling the laser pulse to penetrate much closer to the fuel core it was hoped that the electron coupling could be much improved. Indeed, to some extent, this is what was observed. In experiments in 2002 [15] a deuterated polystyrene fuel pellet was compressed and a short pulse PW laser fired into the cone opening. An enhancement in the number of neutrons by three orders of magnitude was observed when the short pulse laser was present compared to when it was not. More recent work building on cone guided fast ignition involves the use of resitivity gradients to collimate the otherwise divergent source of fast electrons [16, 17]. Although work continues on the development of both of these general schemes, both have drawbacks due to the additional alignment requirements (arising from the departure from the symmetry of the spherical target) and additional target fabrication costs (assuming a potential IFE power station consuming 5 targets a second for a year, 157 million such targets would be required).

The most attractive approach is, of course, the simplest. The ideal would be the use of simple targets and the development of techniques which result in the self-collimation of the fast electron beam, the self-induced uniform transport of fast electrons to the core and the optimum coupling of laser energy to fast electrons. The search for optimised coupling is the focus of this thesis, and as such, this topic will be covered in greater detail in the following chapters.

The issues with fast electron divergence aside there are other applications for intense laser-solid applications which are relevant today. A major motivation in this field is the potential applications of laser generated ion beams. The ability to produce a high energy, high flux particle beam over a distance which is as much as 7 orders of magnitudes smaller (microns compared to hundreds of meters) than conventional accelerators is very attractive. This is especially true for applications such as the use of protons and heavy ions in cancer treatment. While it is not practical, nor financially viable, for the majority of hospitals to operate a cyclotron, the compact size (and radiation shielding) potentially made possible

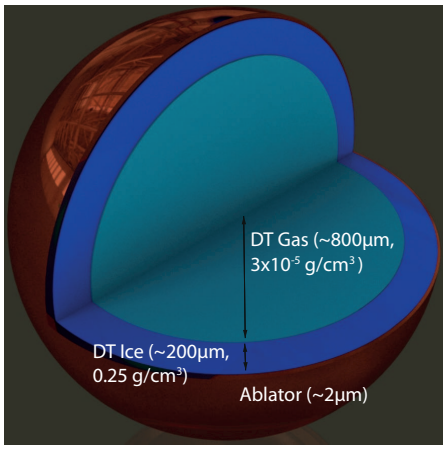

(a)

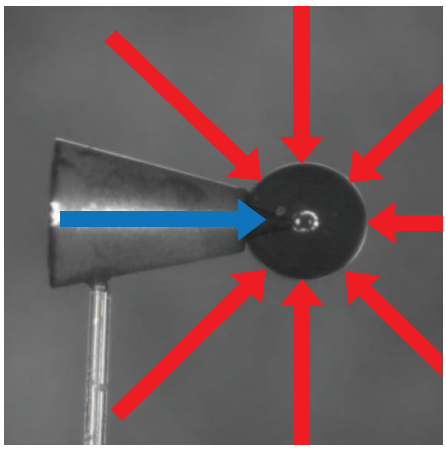

(b)

Figure 1.3: (a) Proposed fuel composition for fast ignition target. (b) Proposed target for cone guided fast ignition concept, also shown are the compression beams (red) and the ignition beam(blue).

by laser-ion sources could make such facilities much more widely available.

It was known for some time, even with nanosecond lasers, that intense laser-plasma interactions result in the production of energetic ions. However, the beams produced under these circumstances are typically sub-MeV and of poor laminarity. It was not until the last years of the 1990's that a breakthrough was made using sub-nanosecond high power laser pulses (facilitated by CPA). The results of Hatchett *et al.* [18], Clark *et al.* [19] and Snavely *et al.* [20] especially, in which beams of protons with maximum energies exceeding 50 MeV emitted normal to the rear surface of the target were observed, showed the potential of laser driven proton acceleration. Indeed, it was also shown that beams of heavier ions are accelerated to high energies. The source of the majority of

these high energy protons and heavy ions was shown to be the atoms at the rear surface of the target, which were either constituents of the target material or contaminant layers. The ionisation and acceleration is driven by the formation of a very large (TV/m) quasi-electrostatic field at the target-vacuum interface as a direct consequence of a portion of the fast electrons accumulating at the rear surface due to space-charge confinement. Target Normal Sheath Acceleration (TNSA) as it later became known is the dominant ion acceleration mechanism at currently available laser intensities. The TNSA mechanism is directly dependent on properties of the fast electron beam, including it's temperature, propagation divergence angle and number density [21, 22]. As such, the focus for developing these sources has been on controlling the ion beam indirectly by controlling the fast electron beam generation and transport properties. This includes changes to the target dimensions [23, 24], material [25] and the use of more complex target geometries [26]. Taking a further step back, the laser properties too have been given much consideration in their relationship to the accelerated ions. The maximum ion energy scaling with laser intensity has been measured by Robson *et al.* [27] among others. The conditions, too, at the front surface of the target have been explored by demonstrating that is there a strong sensitivity to the initial plasma conditions on absorption to fast electrons and, therefore, their subsequent energy transfer to ions [28, 29].

In recent years a new acceleration mechanism which bypasses the complication of having to control the fast electron generation and propagation has been predicted [30]. Radiation Pressure Acceleration (RPA) as it is known relies on the radiation pressure of the laser to accelerate electrons into the target inducing a charge separation field which then also accelerates ions. If the target is sufficiently thin, the laser pressure can be large enough to push through the entire target, breaking off the accelerated region in the process. If this transition is sufficiently smooth a potential exists to reach very high maximum ion energies at moderate laser intensities. Besides high ion energies this mechanism also has the possibility of producing relatively monoenergetic energy spectra. The promise of this mechanism is significant and recent experimental evidence for the mechanism

has been produced [31] . For this effect to become dominant, however, the peak laser intensity must increase beyond what is available with current systems.

In all, the past 50 years has seen an exciting range of fields open up, hand in hand with the development of new lasers technologies reaching ever increasing peak laser intensities. On the horizon is the prospect of laser-driven sources of fusion energy and laser-driven sources of relativistic ions. The challenges that remain, in both areas, are large. In both FI and laser-driven ion acceleration controlling the generation and transport of fast electrons is the key requirement for these applications to be realised. This thesis details experimental work with related numerical simulations carried out by the author (with collaborators), exploring newly developed techniques which demonstrate tentative control of fast electron generation by modifying processes occurring at the front side of the target.

1.2 Thesis Outline

In the following chapter the fundamental underpinnings of laser-plasma interactions in general and laser-solid interactions in particular are introduced. **Chapter 3** will cover in more detail the physics relevant to laser absorption and fast electron generation, providing a review of previous work investigating this issue. The methodology and results of recent investigations into fast electron generation in intense laser-solid interactions are reported in **Chapters 4-7** as follows:

- **Chapter 4** - Methodology: Lasers, diagnostics and simulation
- **Chapter 5** - Surface transport of energetic electrons in intense picosecond laser-foil interactions
- **Chapter 6** - Enhanced laser-to-electron energy coupling in solid density plasmas using a controlled plasma density gradient
- **Chapter 7** - Laser absorption to fast electrons in the transition to the relativistic induced transparency regime

- **Chapter 8** - Summary and conclusions

Chapter 2

Foundations of Laser-Solid Interactions

The physical picture of intense laser-plasma interactions intersects a wide range of fields from nuclear to solid state and from quantum electrodynamics to hydrodynamics. In order gain useful insight into the physics underpinning these interactions we must not only understand the important processes which are relevant from the perspective of these sub-fields but also the overlap between them and the regime in which each area becomes important.

In this chapter the current physical picture which underpins laser-plasma interactions shall be described, from the laser itself to the electron motion in the laser field and the implications that this energy transfer between laser and electron has for the system as a whole, including the resulting generation of magnetic fields, high energy photons and ions.

2.1 High power lasers

The practicalities of the generation of the type of short, intense laser pulse required for these interactions will be covered in the **chapter 4** but for the moment some figures and parameters to aid the forming picture of laser-solid interactions shall be introduced.

The term laser-plasma interaction is perhaps a little nondescript, more specif-

ically the interest is in intense, short pulse laser interactions with a high density plasma slab. *Intense*, typically refers to intensities greater than 10^{18} W/cm^2 but less than 10^{22} W/cm^2. *Short* typically refers to a parameter space which encompasses pulses from 10 fs to 10 picoseconds in duration. In essence, it is the high energy density nature of these interactions which produce interesting physics and, as such, intensity and wavelength are the key parameters.

The laser pulses themselves are often spatially and temporally Gaussian in profile. The temporal nature of the laser pulse is typically described by the laser pulse duration, which is essentially the full width half maximum (FWHM) of the Gaussian pulse envelope. The Gaussian nature of the spatial profile can be characterised by three parameters: the beam waist size, w_0, the Rayleigh range and the Gouy phase. The first of these is the spot radius. The Rayleigh range is the distance over which the spot radius increases by a factor $\sqrt{2}$ and is useful in determining the wavefront radius of curvature. The Gouy phase is an addition to the phase of the laser pulse as it passes through focus.

Another important parameter of the laser pulse to consider is the polarisation direction. Throughout this thesis three polarisations types will be referred to namely; S- , P- and Circular polarisation. Circular polarisation is clearly the polarisation mode where the electric field direction changes as pulse propagates, but the magnitude of the electric field is constant. The other two types refer to cases of linear polarisation. P-polarised pulses are polarised such that the electric field oscillates in the plane of incidence. Conversely, S-polarisation refers to the electric field oscillating perpendicular to the plane of incidence. The more general case of elliptical polarisation is not used in any of the following results, as such a description is not provided here.

Finally, consider a realistic laser pulse, in reality the temporal-intensity profile is more complicated than that shown in the idealised case of Fig.2.1(a). In addition to the slowly-varying Gaussian envelope, some degree of so-called Amplified Spontaneous Emission (ASE) exists. This ASE is a background component of the laser radiation which, most significantly, proceeds the main laser pulse often by several nanoseconds. It has an intensity, often, 10^6 or more times lower than the

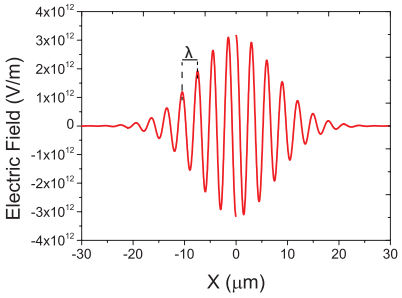

(a)

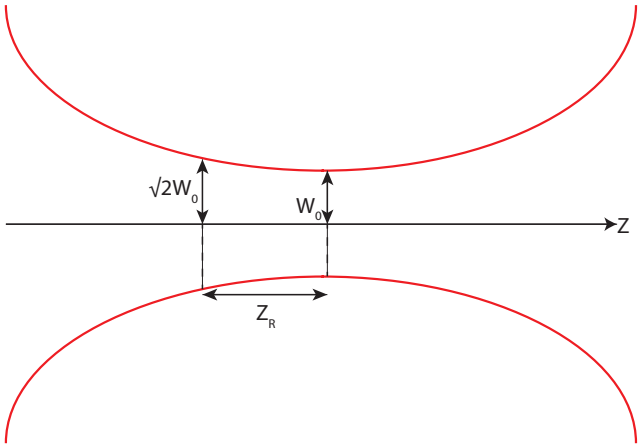

(b)

Figure 2.1: (a) Idealised Gaussian of the type used in laser plasma interactions (b) Schematic of focusing Gaussian beam

main laser pulse. However, given that the intensities present in the laser-plasma interactions detailed here always exceed 10^{18} W/cm^2 this suggests ASE as high as 10^{12} W/cm^2. Intensities at this level are nevertheless large enough to ionise matter and as such this ASE level must also be considered when thinking about short pulse laser solid interactions. The implications of this will be discussed in the following section and the practical details of how ASE forms is covered in **chapter 4**.

2.2 Laser induced ionisation processes

Now that the parameters of the laser pulses generally considered in this thesis have been introduced a discussion can begin on the interaction of these intense laser pulses with, initially, solid density matter.

Consider a solid density slab of a material, for clarity say copper. The laser pulse is focused onto this target. The first part of the laser pulse to irradiate the target is the ASE which arrives on the order of a few nanoseconds ahead of the main pulse. At this point one of two things can happen. One, the ASE level is too low to induce ionisation and ionisation only takes place due to high intensity prepulses or at the rising edge of the pulse (this would be called a high contrast pulse). Two, the ASE is sufficient to induce ionisation and a plasma begins to form.

There are two main mechanisms through which ionisation can take place. It can be best described if by noting that the electric field strength in a hydrogen atom, E_a, is equivalent to

$$E_a = \frac{e}{4\pi\epsilon_0 a_B^2} \tag{2.1}$$

$$\approx 5.1 \times 10^9 V/m \tag{2.2}$$

and where ϵ_0 is the permittivity of free space and a_B is the Bohr radius. The so-called atomic unit of intensity, I_a can then be calculated using

$$I_a = \frac{\epsilon_0 c E_a^2}{2} \tag{2.3}$$

$$\approx 3.51 \times 10^{16} W/cm^2 \tag{2.4}$$

where c is the speed of light in vacuum. Above this intensity any target material will be ionised, forming a plasma. However this intensity is quite high, and is certainly larger than the ASE level described above, consequently there must be processes which cause ionisation at lower intensities. These non-linear ionisation processes can be described in the context of laser intensity. At the lower end when ionisation by the laser pulse becomes just possible a process known as multi-photon ionisation takes place, the threshold intensity for this process is $\approx 10^{10}$ W/cm^2. Instead of a single high energy photon causing ionisation, as

is the case in the photoelectric effect, if the intensity is high enough then the photon rate is large enough to cause ionisation by excitation through absorption of multiple photons. The kinetic energy of the electron freed by this process can be calculated by analogy to the equation for the photoelectric effect.

$$E_f = (n+s)\hbar\omega_L - E_{ion} \tag{2.5}$$

where n is the number of photons needed to induce ionisation and s is the excess number of photons absorbed, $\hbar$ is Planck's constant, ω_L is the angular frequency of the absorbed photons and E_{ion} is the ionisation potential. Ionisation of a hydrogen atom with a laser of 1 μm wavelength would require the absorption of $\approx$12 photons.

The final ionisation mechanism that will be described here becomes important for higher intensities. Consider an electron trapped in the Coulomb potential generated by the ion and then introduce an external field due to the laser, the resulting potential can be calculated to be

$$V(x) = \frac{-Ze^2}{x} - e\epsilon x \tag{2.6}$$

where ϵ is the laser electric field. The application of the external field means that the Coulomb potential of the atom is suppressed. This results in two possibilities. From a quantum mechanical perspective the lowered potential barrier means that the probability of finding the electron outside of the potential well is increased and therefore the ion is more likely to become ionised. This is the so-called over-the-barrier ionisation mechanism. For stronger fields where the barrier is completely suppressed this is called barrier suppression ionisation. In general, as will be the case in this thesis, the whole process is referred to as field ionisation by barrier suppression (FIBS).

The appearance intensity of a given ion species can be denoted as

$$I_{app} = 4 \times 10^9 \left(\frac{E_{ion}}{eV}\right)^4 Z^{-2} W/cm^2 \tag{2.7}$$

So for the copper target used as an example at the beginning of this section it is

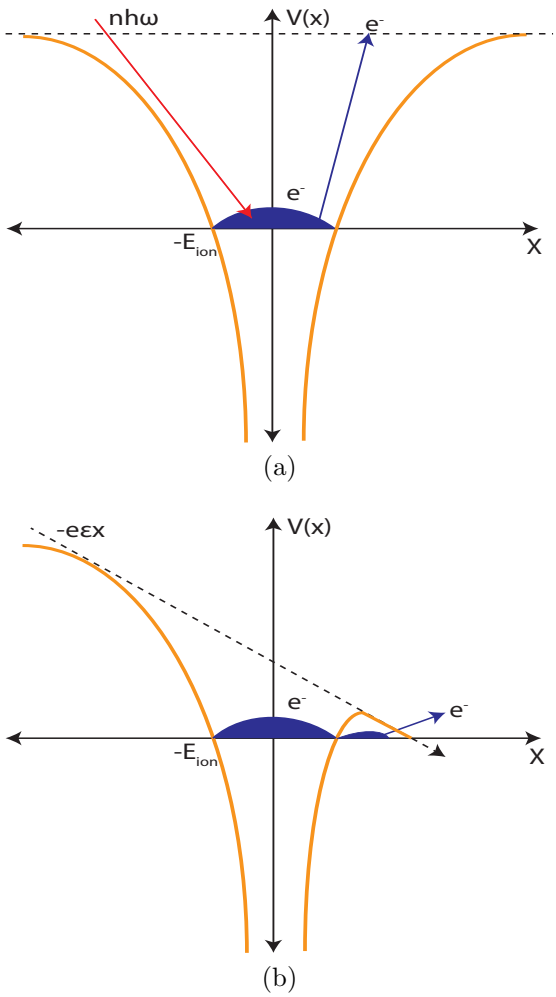

Figure 2.2: (a) Multi-photon ionisation. Multiple photons provide electrons enough energy to escape the atomic potential (b) Field ionisation by barrier suppression. The external laser field suppresses the atomic potential enabling the electron to escape over the suppressed barrier or tunnel through it.

possible to calculate that the Cu^+ ion would be expected to be produced at laser intensities as low as 1.65×10^{10} W/cm^2. For hydrogen, due to the lower atomic number and higher binding energy FIBS does not take place until laser intensities reach 1.4×10^{14} W/cm^2.

The two ionisation processes, multi-photon and FIBS, have been helpfully delineated by Keldysh *et al* [32] who introduced a parameter γ.

The Keldysh parameter is calculated from

$$\gamma = \omega_L \sqrt{\frac{2E_{ion}}{I_L}} \tag{2.8}$$

where I_L is the laser intensity. If $\gamma > 1$ then multi-photon ionisation dominates

and for $\gamma < 1$ FIBS dominates. The two schemes are shown in Fig.2.2

In addition to direct field ionisation by the laser there are other processes by which bound electrons may be freed. Perhaps the most important to consider is the so-called collisional ionisation process. As seen previously, electrons can be provided enough energy to not just escape the atomic potential but can have excess kinetic energy. This excess energy can be high enough such that in collisions with other atoms additional electrons can be freed. For laser-solid interactions where the bound electron density is very high collisional ionisation is dominant once electrons are initially freed by the multi-photon ionisation process.

Having now described the processes by which single atoms can be ionised in a strong laser field, the next section will consider the effect of the ionisation of the whole region of the focal spot and the effect that the resulting expanding plasma has on laser-plasma interactions.

2.3 Laser induced plasma expansion

The rapid generation of a hot plasma by the laser ASE interacting with the solid target results in an expansion of that plasma, directed out to vacuum. The extent of this 'preplasma' as it is known, plays a critical role in determining the absorption dynamics of the main pulse (see following section and **chapter 6**). As such it is useful to have a parameter to characterise this preplasma. This is typically called the plasma density scale length, L, and can be estimated from the laser pulse duration, τ_L, and the ion sound speed, c_0, as follows

$$L \simeq c_0 \tau_L \tag{2.9}$$

where c_0 is

$$c_0 = \sqrt{\frac{k_B(Z^* T_e + T_i)}{m_i}} \tag{2.10}$$

where k_B is Boltzmann's constant, Z^* is the ionisation state, T_e is the plasma electron temperature, T_i is the plasma ion temperature and m_i is the ion mass.

It is, however, more typical to estimate this parameter using hydrodynamic simulations and then make a fit to the resulting electron density profile.

This electron density profile is typically exponential in form and can be described by

$$n_e(X) = n_0 exp(-L/X) \tag{2.11}$$

where $n_e(X)$ is the electron density at a position X along the axis of expansion and n_0 is the initial solid electron density. If the electron density profile is available, from hydrodynamic simulations for example, it is trivial to solve this equation to extract the density scale length.

There are a host of other effects which are relevant for a plasma expanding into vacuum in the presence of an intense laser pulse, such as profile steepening, which leads to a more complex density profile. However, for the scope of this thesis the above section holds the most relevance.

The consequence of driving this rapid thermal expansion of the preplasma into vacuum is to induce a strong shock wave directed into the target foil. This shock wave propagates through the target with a velocity which can be calculated from [33]

$$v_s = \frac{c_0}{2}(\sqrt{1+x}+1) \tag{2.12}$$

where x is given by

$$x = \left(\frac{4\alpha}{\rho_0 c_0^2}\right) P \tag{2.13}$$

where α is an empirical material constant and P is the external pressure, in Pa, applied to the material. This pressure is related to the laser intensity, I by

$$P \propto I^{2/3} \tag{2.14}$$

For ASE intensities of $\approx 10^{12}$ W/cm^2 the shock velocity is of the order of μm/ns. After a few nanoseconds exposure to the ASE the shock will reach the rear surface

of the target, causing it to decompress. This changes significantly the dynamics of the laser-solid interaction. As such there is a limit imposed on the minimum target thickness that can be used for a given laser contrast. As shall be discussed in **chapter 7** contrast is critically important when investigating target thickness on the nanometer-micron scale. Also of interest is the role played by the preplasma density scale lengths in effecting in a positive or negative sense the laser absorption efficiency into the plasma.

One additional effect which is important to consider is the consequence of having a electron density gradient in one direction and a temperature gradient (due to the intensity gradient in the perpendicular direction). This results in so-called thermoelectric magnetic field generation in the preplasma region which can be seen from the source term

$$\frac{\partial \mathbf{B}}{\partial t} = \frac{\nabla T_e \times \nabla n_e}{e n_e} \tag{2.15}$$

where T_e is the electron temperature. This effect can lead to pinching of the underdense plasma which is ablated from the target surface [34].

Now that the important physics that takes place during the nanoseconds of ASE has been detailed, including; ionisation, plasma expansion and shock formation, a discussion can now take place concerning the key physics involved as the main pulse arrives onto this partially preheated, pre-expanded target.

2.4 Laser-to-electron energy absorption mechanisms

A sensible place to start when considering laser-to-electron energy absorption mechanisms is the interaction of an intense, infinite plane wave with a single electron

2.4.1 Motion of a single electron in a plane wave

The force experienced by an electron is described by the well known Lorentz equation:

$$\frac{d\mathbf{p}}{dt} = -e(\mathbf{E} + \frac{\mathbf{v}}{c} \times \mathbf{B}) \tag{2.16}$$

where

$$\mathbf{p} = \gamma m_e \mathbf{v} \tag{2.17}$$

where e is the charge on the electron, $\mathbf{E}$ is the laser electric field, $\mathbf{B}$ is the magnetic field of the laser, $\mathbf{v}$ is the electron velocity, $\gamma = 1/\sqrt{1-(v^2/c^2)}$ and m_e is the electron rest mass.

The effect of the electric and magnetic fields on the electron can be considered individually by considering the electron velocity in the field. Using equation 2.16 the particle velocities are described in the following way

$$m_e \frac{d\mathbf{v}}{dt} = -e(\mathbf{E} + \frac{\mathbf{v}}{c} \times \mathbf{B}) \tag{2.18}$$

$$m_e \frac{d(\mathbf{v_{(1)}} + \mathbf{v_{(2)}})}{dt} = -e(\mathbf{E} + \frac{\mathbf{v_{(1)}} + \mathbf{v_{(2)}}}{c} \times \mathbf{B}) \tag{2.19}$$

taking $\mathbf{v_{(1)}}$ and $\mathbf{v_{(2)}}$ to be on the order of ≈ 1 and $\approx v/c$, respectively, then

$$m_e \frac{d\mathbf{v_{(1)}}}{dt} = -e\mathbf{E} \tag{2.20}$$

and

$$m_e \frac{d\mathbf{v_{(2)}}}{dt} = \frac{v_{(1)}}{c} \times \mathbf{B} \tag{2.21}$$

Assuming $x = 0$, the following can be written:

$$\mathbf{v_{(1)}} = \frac{e\mathbf{E_0}}{m_e \omega_L} sin(\omega_L t) \tag{2.22}$$

for $\mathbf{v_{(2)}}$, since $\mathbf{B} = \mathbf{E_0} cos(\omega_L t)$ it can be shown that

$$\frac{d\mathbf{v_{(2)}}}{dt} = \frac{\mathbf{v_{(1)}}}{m_e c}\mathbf{E_0} cos(\omega_L t) \tag{2.23}$$

$$= \frac{e^2 \mathbf{E_0}^2}{m_e \omega_L} cos(\omega_L t) sin(\omega_L t) \tag{2.24}$$

$$= \frac{e^2 \mathbf{E_0}^2}{2 m_e^2 \omega_L} sin(2\omega_L t) \tag{2.25}$$

and therefore it can be shown that

$$v_{(2)} = \frac{e^2 E_0^2}{4 m_e^2 \omega_L} cos(2\omega_L t) \tag{2.26}$$

Note that the electron velocity oscillates in the laser field at twice the laser frequency. At this point a useful dimensionless parameter called the dimensionless light amplitude, a_0, can be defined, where

$$a_0 = \frac{eE_0}{m_e c \omega_L} \tag{2.27}$$

$\mathbf{v_{(1)}}$ and $\mathbf{v_{(2)}}$ can then be redefined in terms of a_0 as

$$\mathbf{v_{(1)}} = a_0 c sin(\omega_L t) \tag{2.28}$$

$$\mathbf{v_{(2)}} = \frac{a_0^2 c}{4} cos(2\omega_L t) \tag{2.29}$$

Clearly as a_0 becomes greater than unity then the significance of the magnetic field in determining the electron velocity becomes rapidly more important. The laser intensity, I_L at which this switch occurs can easily be calculated by considering the Poynting vector, S

$$I =< S >= \frac{c}{8\pi} E_0^2 = \left(\frac{m_e \omega_L c a_0}{e}\right)^2 \tag{2.30}$$

In more practical units a_0 can then be defined as

$$a_0 = 0.85 \left(\frac{I_L \lambda}{1.37 \times 10^{18} W cm^{-2}} \right)^{0.5} \tag{2.31}$$

Two regimes of laser plasma interaction can therefore be defined, (1) when the electron velocity is much less than c then a_0 is much less than 1 and (2) in the relativistic regime as the electron velocity approaches c, $a_0 \geq 1$. It is widely accepted, that for laser intensities $> 1.37 \times 10^{18}$ Wcm^{-2} the relativistic regime of laser-plasma interactions has been entered for $\lambda_L \approx 1\mu$m. The next section will focus on extending this description to include not a simply a single electron in a plane wave but a plasma in a realistic, inhomogeneous, laser pulse.

2.4.2 Electron motion in inhomogeneous laser fields

The previous section provided details of electron motion in an infinite plane wave and provided insight into how those dynamics change as relativistic effects become increasingly important. However a realistic laser pulse such as that described in section 2.1 has both, in time, a fast oscillating component of a sinusoidal waveform as well as a slowly oscillating intensity envelope and, in space, a Gaussian intensity profile. Therefore the approximations from the previous section cannot be used.

Instead it is necessary to consider what is termed the *ponderomotive force*, which is defined by Gibbon [35] as the time averaged gradient of the electron oscillation, which was defined previously. The non-relativistic version of this force can be written as

$$\mathbf{F_p} = \frac{e^2}{4 m_e \omega_L^2} \nabla \mathbf{E^2} \tag{2.32}$$

Recall the picture described in the previous section of the electron oscillating in the laser field but gaining no net energy. In the realistic case, where the ponderomotive force applies instead, the electron still oscillates in the field but every half cycle it is pushed toward a region of lower intensity. In the second half of the cycle, now that the electron is in a lower intensity region, it feels a reduced return force resulting in a net gain of energy. In the non-relativistic regime

electrons are ejected perpendicularly from the laser axis. Using the previously defined a_0 parameter we can extend the ponderomotive force into the relativistic regime.

It can be shown that

$$\mathbf{F_p} = -m_e c^2 \nabla \sqrt{1 + a_0^2/2} = -m_e c^2 \nabla \gamma \tag{2.33}$$

where $\gamma = \sqrt{1 + a_0^2/2}$ and m is the relativistically corrected mass of the electron in the laser field.

The kinetic energy gained by the electron over the laser cycle can be calculated simply from the *ponderomotive potential*

$$U_p = (\gamma - 1) m_e c^2 \tag{2.34}$$

Unlike in the classical regime, in the relativistic regime the electron trajectory is modified from being ejected perpendicular to the oscillating laser field. Instead it can be shown that, in the single electron case that is currently being dealt with, since the energy is transferred from the EM field to the electron via the momentum transfer of multiple photons it can be said that the momentum in the parallel direction is conserved.

$$p_\parallel = n\hbar k = \frac{n\hbar\omega_L}{c} = \frac{U_p}{c} = (\gamma - 1)mc \tag{2.35}$$

In addition it can be shown that

$$p_\parallel = \frac{p_\perp^2}{2mc} \tag{2.36}$$

and the emission angle can be shown to be

$$tan\theta = \frac{p_\perp}{p_\parallel} \tag{2.37}$$

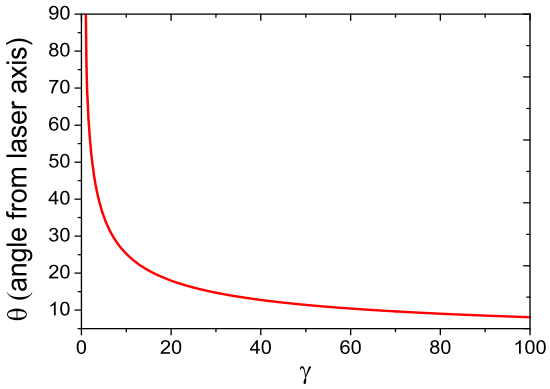

Figure 2.3: Emission angle of a single electron interacting with a laser pulse. As the γ factor increases the emission angle becomes closer to the laser axis.

or alternatively,

$$cos\theta = \sqrt{\frac{\gamma - 1}{\gamma + 1}} \tag{2.38}$$

From this it is clear that as E_0 increases so does a_0, causing an increase in γ and, from Eq. 2.38, as γ increases the ejection angle relative to the laser axis decreases resulting in propagation of electrons closer to the laser axis. This is illustrated in Fig. 2.3. In the following sections the acceleration of electrons along the laser axis, via this heating mechanism as well as other electron heating mechanisms is discussed.

2.4.3 Laser propagation in plasmas

The previous two sections have dealt with, initially, the motion of an electron in an infinite plane wave laser field and, later, with the motion of a single electron in an spatially and temporally inhomogeneous laser field. In reality of course, the laser interacts with a plasma, containing a very large number of electrons as well as large number of positively charged nuclei. This acts to significantly complicate the laser absorption dynamics.

It is useful, before discussing laser induced electron heating mechanisms directly, that the idea of the plasma is properly established. Specifically it is important to define the parameters of a 'laser-plasma' created from a solid. The

density profile of such a plasma was previously discussed in section 2.3, at this time no comment was made specifically on the propagation of the laser pulse through this density profile.

It is possible to define two regimes of laser-plasma interactions by examining the plasma dispersion relation for a relativistic electromagnetic wave

$$\omega_L^2 = c^2 k_0^2 + \omega_p^2 \tag{2.39}$$

where ω_p is the relativistically corrected plasma frequency, k_0 is the laser wave vector. In the case that $\omega_L = \omega_p$ then Eq.(2.39) goes to zero and the laser stops propagating in the plasma and is absorbed or reflected. Stating the plasma frequency, ω_p, explicitly shows how plasma electron density is related to the changing plasma density gradient

$$\omega_p^2 = \frac{n_e e^2}{\epsilon_0 \gamma m_e} \tag{2.40}$$

where n_e is the plasma electron density. Using the condition previously stated, a density can be defined above which the laser pulse will no longer propagate. This is known as the critical density

$$n_{crit} = \frac{\gamma m_e \epsilon_0 \omega_L^2}{e^2} \tag{2.41}$$

For $n_e > n_{crit}$ the laser will not propagate any further into the plasma, this regime is known as *overdense*. For $n_e < n_{crit}$ the laser will continue to propagate through the plasma, interacting with plasma electrons as it goes. This regime is known as *underdense*. As has been stated, the interest here is primarily in the interaction of the laser pulse with initially solid density targets. As such the interaction is dominated by overdense phenomena. However, as will be shown in **chapter 6** laser pulse propagation physics in the underdense region of the plasma formed at the front side of the solid can play a critical role in laser-electron energy conversion and the interaction dynamics.

Note also the presence of the factor γ in Eq.(2.40) and Eq.(2.41). As has been previously discussed, this factor acts to increase the mass of the electrons in the

plasma as they oscillate in the laser field to relativistic velocities. In the context of the critical plasma density however this factor acts to increase this density. This effect, where the electron oscillation in the laser field allows the laser to propagate to higher densities than is classically possible, is known as relativistic induced transparency (RIT). This subject will be the focus of discussion in **Chapter 7**.

Another effect which occurs due to the increasing electron mass is known as relativistic self focusing. The effect is best explained by considering the plasma refractive index which is given by

$$\eta = \sqrt{1 - \frac{n_e}{n_{crit}}} = \sqrt{1 - \frac{\omega_p^2}{\omega_L^2}} \tag{2.42}$$

As has already been established the gamma factor scales with intensity. Consider the Gaussian profile of the incoming laser pulse. This profile has an intensity maximum, which corresponds to a γ maximum on axis. In the wings the intensity is lower as is, consequently, the factor γ. This therefore results in the lowest plasma frequency being on axis and highest being in the wings of the profile. From Eq. 2.42 the lower the plasma frequency the higher the refractive index. In terms of the phase velocity of the pulse then this relation results in the wings of the pulse travelling faster in the plasma than the peak of the pulse. This results in an effect similar to a positive lens, the laser begins to "self-focus" in the plasma. Combined with what has already been stated about the scaling of the critical density as the laser intensity is increased this self-focusing effect can lead to induced transparency as well as changes in the laser absorption into the plasma. This subject will be returned to in **Chapter 6**.

Now that some of the basic features of a relativistic laser pulse propagating in a plasma have been established, the mechanisms via which energy is transferred into electrons can be discussed.

2.4.4 Absorption mechanisms in high density plasmas

In the example given in section 2.4.1 the electron gains no net energy as it oscillates in the laser field. For net energy to be gained there has to be a process

whereby the laser transfers energy to the electron and is then unable to recover that energy in the second half of the laser cycle. The ponderomotive force is an example of this for single electrons. However, in a high density plasma there are a number of mechanisms which rely on the plasma itself to provide a medium for net energy gain to occur. These processes can be broken into two main types.

The first is so called collisional absorption mechanisms. These mechanisms rely on the plasma electrons initially gaining energy from the laser field but colliding with plasma ions and thereby losing that energy to the plasma before the laser recovers it. This, of course, relies on the mean free path of electrons being less than the extent of the plasma. Inverse bremsstrahlung is an example of a collisional absorption mechanism. However for the intensities discussed here, ranging up to 10^{20} W/cm^2 the electrons are essentially collisionless, at least within the plasma skin-depth, which means other processes become more important. The collisional regime of absorption mechanisms is important for intensities up to $\approx 10^{15}$ W/cm^2, as such this mechanism is important in transferring laser energy to electrons during the ASE phase of the laser pulse.

The second type of absorption mechanism is collisionless absorption. This occurs when the electron oscillations in the laser field are so large that the electron is driven past the critical density surface. As a consequence this electron is no longer influenced by the laser field and carries away net energy. There are a number of processes which enable this to happen, but there are three which are particularly relevant: resonant absorption; vacuum heating; and $\mathbf{J} \times \mathbf{B}$ heating.

Resonant absorption

In resonant absorption the electric field of a p-polarised laser pulse resonantly excites plasma oscillations at the critical density surface. A necessary condition of this is that the oscillations are only driven when the laser electric field is parallel to the density gradient. In order for electrons to be driven in this direction the incoming pulse has to have oblique incidence and be p-polarised i.e in the plane of propagation. The laser electric field acts to drive electrons into the plasma beyond the critical density, this is illustrated in Fig.2.4. At this point the laser

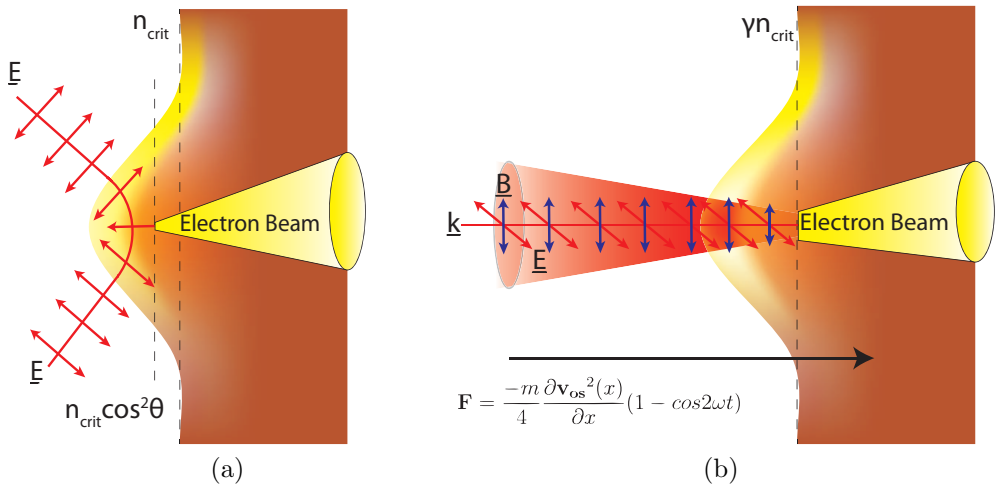

Figure 2.4: (a) Schematic of resonant absorption. Oblique incidence and p-polarisation of laser pulse induces electron injection in the direction of the density gradient at the turning point. (b) Relativistic $\mathbf{j} \times \mathbf{B}$ acceleration. Electrons are injected into the target, at twice the laser frequency, along the laser k-vector.

field is evanescent and thus the restoring force on the electrons is weaker.

The condition on oblique incidence modifies the point of reflection from n_{crit} to $n_{crit}cos^2\theta$. This can be best explained by again considering the dispersion relation outline shown in Eq. 2.39 but modifying the laser k-vector transverse to the density gradient to include the incidence angle which becomes $k_y = (\omega_L/c)sin\theta$ and consequently the dispersion relation can be re-expressed as

$$\omega_L^2 = \omega_p'^2 + k_x^2c^2 + \omega_L^2 sin^2\theta \tag{2.43}$$

when $k_x^2 < 0$ the laser has been reflected, this condition occurs when $n_e > n_{crit}cos^2\theta$. The plasma wave which forms due the laser can either grow over many laser cycles until it breaks, injecting electrons into the target, or if the laser field is sufficiently intense, over one laser cycle. Typically resonant absorption is dominant for long density scale lengths and intensities beyond 10^{12} W/cm^2 but less than 10^{17} W/cm^2.

Vacuum Heating

Vacuum heating is very similar to the resonant absorption mechanism except that the plasma oscillations are driven in a plasma with a very sharp density

gradient. It is known by a number of names in the literature including Brunel heating, not-so-resonant resonant absorption and, of course, vacuum heating. For very sharp density gradients the electron oscillation amplitude is larger than the plasma density scale length. As such electrons are pulled out into vacuum in the first part of the cycle these electrons are then driven back into the plasma by the same field in the second part of the cycle. Given the abrupt density change the electrons very quickly oscillate beyond the plasma skin depth and are no longer affected by the laser field, carrying away energy in the process [36]. Unlike in the resonant absorption process the steep density gradient plasma cannot support an oscillation which grows over many cycles. Instead, electrons in this case are injected once per cycle.

Relativistic $\mathbf{j} \times \mathbf{B}$ Heating

Perhaps the most relevant electron heating mechanism for the results discussed in this thesis is the so called $\mathbf{j} \times \mathbf{B}$ heating mechanism. Originally proposed by Kruer and Estabrook (1985), the mechanism is reliant on the fast oscillating $\mathbf{v} \times \mathbf{B}$ component of the Lorentz force. In comparison to the vacuum and resonant absorption processes which require oblique incidence and short (in the case of vacuum) and long density scale lengths (for resonant), $\mathbf{j} \times \mathbf{B}$ is optimised for normal incidence and will work for reasonably long density scale lengths. As such, for the conditions reported in the following sections this absorption mechanism will typically be dominant.

Recall sections 2.4.1 and 2.4.2 where the fast oscillating $\mathbf{v} \times \mathbf{B}$ component begins to dominate the electron motion for intensities beyond 10^{18} W/cm^2 and that as the electrons become more and more relativistic they are accelerated at angles closer to the laser axis. This process works in much the same way, electrons are ejected from regions of high intensity by the ponderomotive force, but are, in addition, rapidly heated by the fast oscillating component. This force is directed in the laser k-vector direction and can be expressed as

$$\mathbf{F} = \frac{-m_e}{4} \frac{\partial {\mathbf{v_{os}}}^2(x)}{\partial x} (1 - cos2\omega_L t) \tag{2.44}$$

where $\mathbf{v_{os}}$ is the electron quiver velocity. The first set of terms on the right hand side of the equation act to drive electrons away from regions of highest intensity. This is the ponderomotive force described in section 2.4.2. The second set of terms on the right hand side of the equation is the $\mathbf{j} \times \mathbf{B}$ component. This force oscillates electrons at $2\omega_L$, driving them along the laser k-vector direction. The oscillation of these electrons close to n_{crit} results in some being driven into the overdense region of the plasma, resulting in the electron carrying away energy from the laser pulse.

Note the fast oscillating component goes as $2\omega_L$, injecting electrons into the plasma at twice the laser frequency. This is in contrast to the vacuum or resonant heating mechanisms which inject electrons at the laser frequency. In addition where previously an incidence angle was required, $\mathbf{j} \times \mathbf{B}$ heating is optimised for normal incidence angles and will work for both s- and p-polarised laser pulses, but not for circular polarisation.

In the circular polarisation case the oscillating component goes to zero resulting in a reduced heating of electrons in the plasma. This can be seen by considering the ellipticity of the incoming laser. In a more generalised version of Eq.(2.44) the oscillating component becomes $(1 - \epsilon^2/1 + \epsilon^2)cos2\omega_L t$. Where ϵ is the ellipticity ($0 < \epsilon < 1$). For linear polarisation the ellipticity is 0 and the expression becomes that shown in Eq.(2.44). For circular polarisation, however, the ellipticity is 1, which causes this term to vanish. As will be shown in **chapter 7** this can have quite dramatic effects on the dynamics of the laser-plasma interaction.

2.5 Fast electron transport

In the previous sections the discussion centred around the mechanisms which transfer energy from the laser to electrons at the critical density surface. At densities larger than this the laser no longer propagates while the electrons which have been accelerated continue into the target. Such is the energy and number of electrons generated during this interaction that the peak current of the electron

beam is on the order of mega-amperes (MA). Classically for such high currents it was noted by Alfén [37] that the self induced magnetic field of the electron current acts to turn the electrons back toward the source. When the current is above a limiting value it can no longer propagate. This value can be estimated from

$$J_A = \frac{4\pi}{e\mu_0} p \tag{2.45}$$

where p is the electron momentum and μ_0 is the permittivity of free space [38]

For a 1 MeV electron beam this limit is 47.5 kA (assuming an infinitely wide beam) which is orders of magnitude less than the predicted magnitude of the fast electron current. As such it would reasonable to expect propagation of a current on the order of tens of kA. However, experimentally electron currents much larger than this are known to propagate. Some other effect must therefore mitigate this limit.

Indeed, the work by Alfvén considered the net current, not simply the current flowing in one direction. As the electron beam enters the plasma the initial space charge field established by the electron displacement draws an equal and spatially localised return current, sourced from the plasma bulk. This return current is significantly colder than the forward going beam but contains more electrons, creating an effective net current which is lower than the Alfvén limit. This current balance is often expressed simply as

$$\mathbf{j_{fast}} + \mathbf{j_{return}} \approx 0 \tag{2.46}$$

The spatially localised nature of the return current compared to the forward going current was emphasised by Bell *et al.* [39]. In this work they demonstrate that the self generated magnetic field of a "naked" cylinder of electrons with a temperature $T_e \approx 100$ keV would be of the order of 4 Gigagauss. Over the expected propagation length they calculate the energy content of the magnetic field to be greater than the total absorption laser energy. Obviously, therefore it must be that the return current is spatially overlapped with the forward going

current in order to mitigate the formation of otherwise impossibly large magnetic fields.

Magnetic fields of a smaller order can still form however if the return current does not exactly match the forward current. In this case it is the electric field of the fast, forward current which induces a radial magnetic field from Faraday's law

$$\mathbf{E} = \eta_{\mathbf{e}}\mathbf{j}_{\mathbf{return}} \tag{2.47}$$

$$\frac{\partial \mathbf{B}}{\partial t} = -\nabla \times \mathbf{E} = \nabla \times (\eta_e \mathbf{j}_{\mathbf{return}}) \tag{2.48}$$

$$\nabla \times \mathbf{B} = \mu_{\mathbf{0}}(\mathbf{j}_{\mathbf{fast}} + \mathbf{j}_{\mathbf{return}}) \tag{2.49}$$

where η_e is the resistivity of the plasma. Clearly if the current is not neutralised then the net current is

$$\mathbf{j}_{\mathbf{fast}} + \mathbf{j}_{\mathbf{return}} = \frac{\nabla \times \mathbf{B}}{\mu_0} \tag{2.50}$$

$$\mathbf{j}_{\mathbf{return}} = \frac{-\nabla \times \mathbf{B}}{\mu_0} - \mathbf{j}_{\mathbf{fast}} \tag{2.51}$$

$$\frac{\partial \mathbf{B}}{\partial t} = -\nabla \times \left(\frac{\eta_e}{\mu_0} \nabla \times \mathbf{B} - \eta_e \mathbf{j}_{\mathbf{fast}} \right) \tag{2.52}$$

$$\frac{\partial \mathbf{B}}{\partial t} = -\nabla \times \left(\frac{\eta_e}{\mu_0} \nabla \times \mathbf{B} \right) + \nabla \times (\eta_e \mathbf{j}_{\mathbf{fast}}) \tag{2.53}$$

For the plasma conditions present inside the target the η_e/μ_0 term in Eq.2.53 is ≈ 1 and so the equation simplifies to

$$\frac{\partial \mathbf{B}}{\partial t} = \nabla \times (\eta_e \mathbf{j}_{\mathbf{fast}}) \tag{2.54}$$

$$\frac{\partial \mathbf{B}}{\partial t} = \eta_e (\nabla \times \mathbf{j}_{\mathbf{fast}}) + \nabla \eta_e \times \mathbf{j}_{\mathbf{fast}} \tag{2.55}$$

The two terms on the RHS of Eq.(2.55) act as two different sources of magnetic field generation inside the target. The first, $\eta_e(\nabla \times \mathbf{j}_{\mathbf{fast}})$, is due to current density

variation across the fast electron beam. As there is a higher current density on-axis compared to the wings of the beam, there is a radial force, directed inward, which acts to pinch the beam. Current density modulations within the beam also produce this force, which then re-enforces the modulation leading to beam break up.

The second term on the RHS of this equation occurs due to resistivity gradients in the plasma. In other words, in a plasma of uniform material, due to temperature gradients. Since the current density is highest on-axis and the return current, which is collisional (unlike the fast current), is spatially localised with the forward going current, the greatest heating will occur on axis. Much like the current density gradient off axis there will, therefore, also be a temperature gradient which results in a resistivity gradient, as the resistivity varies with temperature. The magnetic field induced by this gradient, depending on the sign, acts to either push fast electrons off axis, leading to an expansion of the beam or pinch, leading to a reduction in the beam size. These two terms acting in conjunction, results in a complex evolutionary behaviour over the duration of the beam. This effect has in fact been explored in order to improve fast electron transport by using the competing effects, through careful choice of initial temperature or target material [16] or structure [25] to produce a higher quality electron beam.

At this point it is useful to introduce the concept of the inherent divergence of the propagating fast electron beam. This problem attracts significant research interest and remains a stumbling block for immediate applications of laser-solid interactions.

As discussed in the previous sections the fast electron beam is not collimated. There are a number of factors which determine the fast electron divergence. One of these is the formation of a competing azimuthal pinching magnetic force and a diffusive resistively generated magnetic force. In addition there is also the angle at which the electron is ejected from the laser field, as shown in Fig.2.3. The fast electron divergence is typically measured as a half-angle. Experimental studies suggest that this half angle is of the order of 25° for intensities of 10^{20} W/cm^2 [13], however accurate measurement of this angle remains difficult especially due

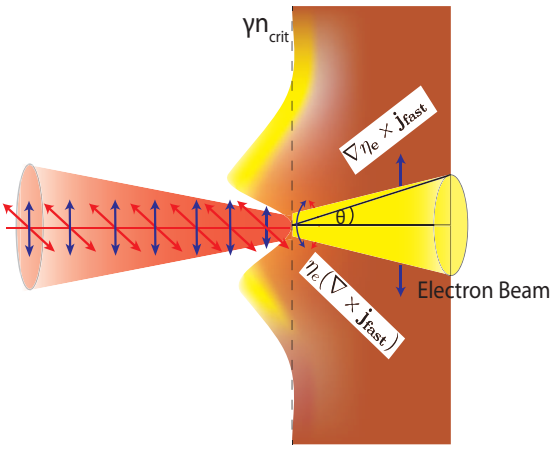

(a)

Figure 2.5: Schematic of the divergent fast electron beam. The pinching and diffusive self-generated magnetic fields contribute to divergence, as well as the electron motion in the laser field.

to the time integrated nature of most diagnostics [40]. A schematic of the effect of fast electron divergence is shown in Fig.2.5.

2.5.1 Fast electron spectrum

The collisionless absorption mechanisms discussed in section 2.4.4 inevitably leads to a certain fraction of electrons being super-heated in the laser field as compared to the average plasma temperature. The energy extracted from the field by a given electron can be stochastic, leading to a large spread in electron energies. It was shown by Bezzerides *et al.* [41] that averaging over these energies leads to a Maxwellian distribution. For relativistic intensities however this distribution can become modified from the single temperature Maxwellian to a two temperature Maxwell-Juttner distribution.

Measurements of x-ray emission from the target suggest that the absorbed fraction of laser energy into the fast electron spectrum is 20%-40% for intensities up to 10^{20} W/cm^2 [42]. Assuming $\approx 5 \times 10^{13}$ electrons are produced by a 100 J laser pulse, the mean energy of the fast electron spectrum is $k_B T_e = 2.5$MeV. This mean energy is often termed the fast electron temperature.

The way in which $k_B T_e$ scales with laser intensity has been an area of research for a number of years. There are a range of possible scaling functions which apply

under different conditions. The most widely cited are perhaps the Beg *et al.* [43] and the Wilks [44] scaling.

The Beg scaling is derived empirically from measurements of γ-ray emission and scales as $215[I_{18}\lambda_\mu^2]^{1/3}$. Where the intensity, I_{18} is in units of 10^{18} W/cm^2 and λ_μ is in microns. Whereas the Wilks scaling is derived analytically and increases as $511[(1+0.73I_{18}\lambda_\mu^2)^{1/2}-1]$, where the intensity and wavelength is in the same units as the Beg scaling. In both cases k_BT_e scales with some function of $I_{18}\lambda_\mu^2$.

The fact that there are a number of proposed scaling laws which fit the experiment data within a limited range of parameters highlights, somewhat circuitously, the key point. It has so far proved extremely difficult to get a good measure of the fast electron spectrum inside the target. Current experimental methods work for a limited range of energies and are often time integrated. Moreover, measurements of the escaping spectrum have been shown to differ significantly from the initial spectrum due to modifications caused by sheath fields which form on the surface of the target [45]. Research in this area is ongoing but it currently remains one of the most opaque aspects in laser-solid interactions.

2.6 Laser driven ion acceleration

For the vast majority of this chapter the ion motion in the plasma has been largely ignored. In general, this approach is justified due to the combination of the significantly larger ion mass (compared to electrons) and the short time scales (sub-picoseconds) which has been the focus of the discussion. The ions do however begin to move on time scales of tens of picoseconds or when the fields are so large that the increased inertia of the ions is overcome.

As was briefly outlined in the introduction chapter, the properties of laser-driven ion beams have gained significant interest due their potential to act as a compact, high energy and comparatively inexpensive source of ions. There are a number of well established mechanisms which accelerate ions in laser-plasma interactions some of which are beyond the scope of this thesis. One mechanism of ion acceleration however has particular relevance to this thesis and is described

below.

2.6.1 Target normal sheath acceleration

Target normal sheath acceleration (TNSA) is an ion acceleration mechanism which has become solidly established in the past 10 years. Indeed, it has been demonstrated in this period to be a mechanism of some resilience. Across a wide range of laser intensities, pulse lengths, target materials and thicknesses essentially the same process takes place.

In the last section the transport of fast electrons through the target bulk to the rear surface of the target was considered. This beam of electrons, as already established, has a broad energy spectrum and an inherently large divergence angle.

As these electrons reach the rear surface of the target, the highest energy ones escape causing the build up of a net positive charge. Further electrons are then turned around as the field increases. Due to the plasma nature of the target free electrons inside it move to screen the rest of the remaining material from the strong electric field which builds up. This inevitably leads to the formation of a sheath region on the rear surface of the target.

Electrons which arrive at the rear surface of the target after the formation of this sheath region can be reflected back into the target. For similar reasons a sheath region is also set up on the front surface of the target. Consequently fast electrons can be trapped inside the target, reflux back and forth between surfaces [46]. Due to the inherent divergence of the electron beam this in reality results in a progressive motion of electrons towards the target edges. This so called 'lateral' spreading of electrons is of significance for electron transport, as shall be demonstrated in the following chapters, and can significantly change the dynamics of ion acceleration [23, 47].

The sheath at the rear surface extends over a distance of the so-called Debye

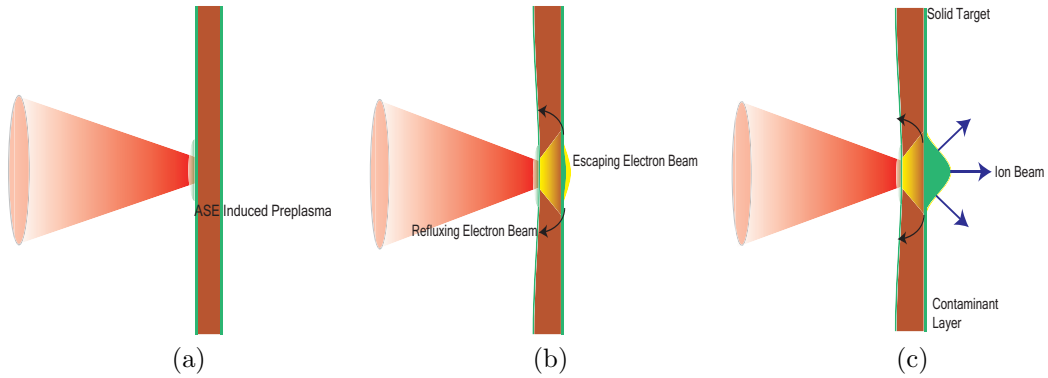

Figure 2.6: (a) Laser pulse arrives on target with the ASE inducing the formation of a preplasma (b) Fast electrons are generated from the front surface and transported through the target. Some of the electrons escape and others are reflected by the forming sheath and begin to reflux within the target (c) Sheath is fully formed, ionising and accelerating ions from the rear surface of the target.

length and can be expressed as

$$\lambda_D = \sqrt{\frac{\epsilon_0 k_B T_e}{n_e e^2}} \tag{2.56}$$

The field which forms in this sheath region is however extremely strong (on the order of TV/m). Much like the laser interaction with atoms at the front surface of the target this field is strong enough to induce the FIBS ionisation mechanism producing positively charged ions. In addition, once these ions form, the sheath field is strong enough to accelerate them over the sheath extent (λ_D) to energies of tens of MeV. The magnitude of this sheath field is given by

$$E_{sheath} = \sqrt{\frac{2}{e_N}} \frac{T_e}{e\lambda_D} \tag{2.57}$$

where e_N is Euler's number and the other terms hold their previous definitions.

Compositionally the accelerated ion beam consists of a number of ion species. Perhaps unexpectedly the majority of ions accelerated come not from the bulk target layer but a thin, so-called 'contaminant' layer which forms on the rear surface of the target. This layer consists of hydrocarbons and water vapour which is present in the atmosphere and builds up on the target surface. Due to the favourable charge-to-mass (q/m) ratios of the ion species in this layer (for example hydrogen has a $q/m = 1$) they are preferentially accelerated and reach the

highest ion energies. Experimental measurements show that it is typically three ion species (hydrogen, carbon and oxygen), in various charge states which dominate the composition of the ion beam. Previous studies have shown however it is possible to increase the number of accelerated ions of the bulk material by partially removing this layer through ohmic heating to remove surface contaminants [48, 49].

The ion beam itself has three other important characteristics, namely the energy spectrum, divergence and emittance. Starting with the spectrum first, the typical energy spread for ions accelerated by the TNSA mechanism is exponential. The model by Mora [21], which is covered in more detail in **Chapter 5** demonstrates that the energy spectrum is described by the exponential function.

$$dN/dE = [n_{e0}c_s t_{acc} S_{sheath}/(ET_e)^{1/2}]exp(-(2E/T_e)^{1/2}) \tag{2.58}$$

where E is the ion energy. The sound speed c_s is

$$c_s = (Z_i T_e/m_i)^{1/2} \tag{2.59}$$

where Z_i is the ion charge and m_i is the ion mass. The sheath area, S_{sheath} is given by

$$S_{sheath} = \pi(r_0 + dtan\theta)^2 \tag{2.60}$$

where r_0 is the the laser focal spot radius and θ is the fast electron half angle of divergence. Finally the acceleration time t_{acc} is empirically derived [22] as $t_{acc} \approx 1.3\tau_{laser}$, where τ_{laser} is the laser pulse length.

The accelerated ion beam, as well as being spectrally broad, is divergent. This can be understood by considering the sheath electric field at the rear of the target. This field is strongest on axis and decays transversely with a Gaussian form. Given that the ions are accelerated at angles normal to the sheath, the ion divergence is therefore energy dependent. This effect is illustrated in Fig.2.7.

As a consequence of the divergent nature and Gaussian like source of the

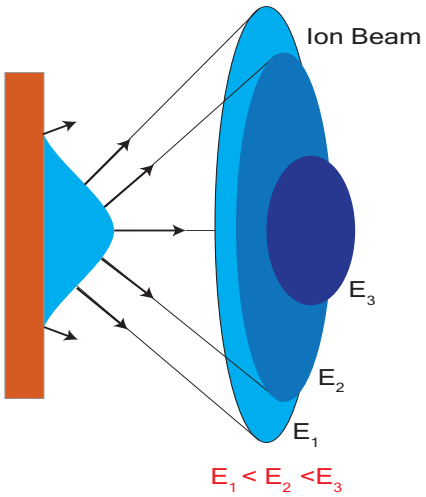

(a)

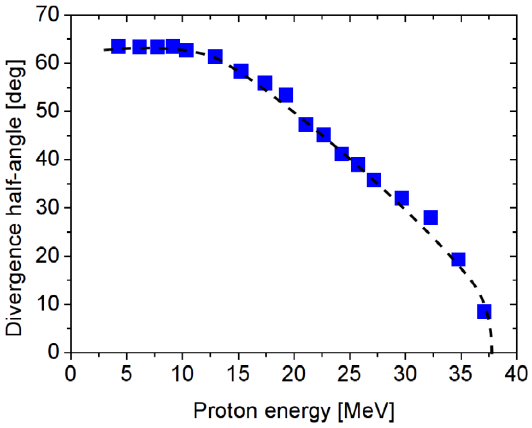

(b)

Figure 2.7: (a) Schematic showing how the divergence of the ion beam is a result of the sheath profile, and that this divergence is energy sensitive. (b) Plot of the half angle divergence of protons with energy.

ion beam and the fact the ions are accelerated over a very short period of time (limiting thermal spreading), laser-driven ion beams have a very good laminarity. In other words the ion trajectories do not cross over. In combination with the other characteristics outlined above the overall result of the TNSA mechanism is an ion beam of very high spatial quality, short temporal duration but large spectral spread.

2.7 Summary

In summary, it has been demonstrated that there are a broad range of effects, covering a wide area of physics. Including quantum effects present in the ionisation processes, fluid effects in the expanding plasma, electromagnetic effects in the absorption of laser energy into electrons and plasma effects which determine how those electrons propagate through the target. It is the combination of these various areas which create an extremely complex interaction which is dominated by collective effects. In the following chapters it will be shown that gaining an understanding of these interactions requires a combined approach consisting of experiments as well as numerical and analytical modelling.

Chapter 3

A review of laser-electron energy conversion in laser-solid interactions

In the previous chapter the discussion centred around some of the well established physics underpinning laser-solid interactions. This chapter focuses on some of the recent developments in laser-solid interactions and, in particular, the parameters which drive changes in the conversion of laser energy to fast electrons are reviewed. The aim of this review is to establish the current state of the art in the field, while simultaneously putting into context the work carried out by the author (with collaborators) which is presented in the following chapters.

3.1 Fast electron generation: Mechanisms, parameters and progress

The conversion of laser energy into fast electrons is facilitated by a host of absorption mechanisms, as discussed in **chapter 2**. The efficacy of these mechanisms depends of a range of parameters including laser intensity, polarisation, incidence angle and preplasma density scale length. In the late 1980s when short pulse lasers became available, somewhat in contrast to long pulse lasers which for

many years had the clear application of laser fusion, routes to new applications of laser-plasma interactions were being actively sought. In the literature much of the focus is on the use of such interactions as ultra-fast x-ray sources to be used in pump-probe type experiments. The intensities in these early days were not yet capable of generating relativistic particles or high energy, directed ion sources. Much of the work focused on clearly establishing the differences between the long pulse and short pulse regimes, before investigating new paths to applications. In particular it is important to note that, perhaps the key expected difference between long and short pulse interactions is the plasma density profile. In long pulse irradiation of a solid, the plasma forms and has enough time to significantly expand into vacuum resulting in very long density scale lengths. In the short pulse interaction the expansion is typically much less, resulting in energy deposition at significantly higher electron densities.

One of the first studies of laser energy absorption in the short pulse regime was that of Kieffer *et al.* [50], who in 1989 demonstrated changes in absorption for a 1 ps pulse interacting with a solid density target across an intensity range from 10^{10} W/cm^2 to 10^{15} W/cm^2. Using a combination of an Ulbricht sphere, for scattered light, and a backscatter calorimeter for the specular light they demonstrate a number of effects now considered fundamental to laser-solid interactions. First they show for low intensities $I < 10^{11}$ W/cm^2 that the interaction is mirror-like, with little absorption and essentially no plasma formation. At normal incidence, for $10^{11} \leq I \leq 10^{12}$ W/cm^2 the absorption increases significantly up to 50%, as a plasma is rapidly formed due to the onset of the FIBS ionisation mechanism described in the previous chapter. Beyond this intensity up to 10^{15} W/cm^2 the absorption remains relatively constant, staying at least above 40%. By changing to oblique incidence a polarisation dependent absorption effect is detected. Comparing s-polarised light to p-polarised for intensities beyond 10^{15} W/cm^2, p-polarised light is shown to be absorbed more effectively. This difference, is attributed to the onset of the resonance absorption mechanism, also described in the previous chapter. Also worth noting is the detection of "hot" electrons on the order of 200 eV. Other experiments within a few years of this (such as that by Meyerhoffer *et*

al.[51]), under similar conditions, show comparable results. Moreover, for slightly higher intensities they observe superthermal electron temperatures up to 10 keV. These experiments, therefore, by covering a large intensity range demonstrate a number effects which are critical to providing a perspective on absorption and fast electron generation in laser-solid interactions. Namely, the coupling can be very sensitive to the plasma on the front surface as well as the laser intensity and finally that the incidence angle and laser polarisation are important for some mechanisms.

After the introduction of the idea of fast ignition (FI) in 1994 by Tabak *et al.* [5], an interesting shift of focus occurs toward optimising fast electron generation in laser solid interactions. For FI a laser of pulse duration shorter than the fuel disassembly time of 10 ps is required. Additionally, since high electron temperatures are required for efficient heating of the completed fuel core the input energy must also be large, on the order of kJ. The combination of these two requirements and the fact that the laser is focused to a small area inevitably results in very high laser intensities for fast ignition, up to 10^{20} W/cm^2. A consequence of such high intensities is also to introduce relativistic effects in the laser-plasma interaction. Indeed in the FI scheme such effects are considered as a way of tunnelling the laser pulse through the coronal plasma and generating electrons closer to the high density region of the fuel. The combination then of an exciting application for laser-solid interactions, the requirement of this application for very high intensity pulses and the generation of beams of relativistic electrons encouraged the field to move towards studies of absorption and fast electron generation under such conditions.

One of the earliest studies which examined absorption and fast electron generation at relativistic intensities was that of Teubner *et al.* [52], in which an Eximer (KrF) laser exceeding an intensity of 10^{18} W/cm^2 is used. Unlike the previously highlighted studies the laser wavelength in this case is 248 nm, in the ultraviolet range of the spectrum. This is used in an attempt to exploit the electron temperature scaling with laser wavelength ($\approx I\lambda^2$) to produce electrons (when the intensity is scaled up) of the correct temperature for FI. In addition, the fact that

shorter wavelengths can propagate to higher densities would enable the source of electrons to be deeper into the coronal plasma, as required by the FI scheme.

In that experiment, Teubner *et al.* measure laser absorption of up to 70% for intensities beyond 10^{18} W/cm^2, for p-polarised laser pulses at incidence angles as high as 70-80°. They attribute this to the so-called anomalous skin effect mechanism which much like the vacuum absorption mechanism, bears the characteristics of resonance absorption but occurs in step-like plasma of very short density scale lengths and is optimised for large incidence angles. They also estimate that the electron temperature of the quasi-Maxwellian spectrum generated during this interaction is of the order 40 keV. At these intensities relativistic effects are just beginning to occur, and the $\mathbf{v} \times \mathbf{B}$ component of the Lorentz force is beginning to influence electron trajectories in the laser field. Much of the theoretical underpinning for this absorption mechanism came some years prior to the availability of laser intensities beyond the relativistic threshold. Wilks *et al.* [53] demonstrate, using particle-in-cell simulations, that, as discussed in the previous chapter, there is a oscillatory heating mechanism induced by the laser magnetic field for intensities $I > 10^{18}$ W/cm^2 which leads to the generation of very high (MeV) electrons. This collisionless electron heating mechanism ponderomotively accelerates electrons along the direction of the laser k-vector.

Laser pulses which were capable of testing this mechanism and accelerating electrons into the highly relativistic regime became available in the closing years of the 20^{th} century. Two early studies in particular demonstrated the onset of this regime, and indeed a good agreement with the predictions of Wilks *et al.* Using laser pulses up to 10^{19} W/cm^2 and magnetic electron spectrometers at angles of 22°, 135° (in the backward direction) and 0° (along the laser axis direction) Malka *et al.* [54] show MeV electrons directed along the laser axis direction. In addition they find that the mean energy of the electrons scale, in good agreement, with the temperature scaling predicted by the $\mathbf{j} \times \mathbf{B}$ ponderomotive model. The second of these two studies was conducted by Beg *et al* [43] and also demonstrates electron energies exceeding 1 MeV. However, unlike in the previous study where the laser intensity contrast was very poor by modern standards ($\approx 10^{-3}$), the contrast

in the Beg *et al.* experiment was close to 10^{-6} which results in a significantly smaller initial plasma density scale length. In this experiment they attribute the dominant absorption mechanism to be vacuum or resonant absorption and not necessarily the $\mathbf{j} \times \mathbf{B}$ process. It is important to note however that the electrons measured in both of these cases are those which escape the target. Accurately measuring the spectrum of the fast electrons which initially propagate inside the target remains a point of difficulty today. Another study, conducted by Wharton *et al.* [55], however attempted exactly this, a measurement of the in-target fast electron spectrum.

The experiment by Wharton used a 'sandwich' type target consisting of two layers of a test material (CH, Al or Cu) and a middle fluorescent layer of molybdenum. High energy electrons propagating through the target ionise molybdenum atoms in this layer by knocking out inner shell electrons. Electrons in higher shells then move into replace this electron, emitting an x-ray photon in the process, which is detected outside the target and used to estimate fast electrons numbers. By varying the depth of the fluorescent layer, electron energies were estimated. Wharton *et al.* find that there is an approximately 20-30% conversion of laser energy into forward-directed fast electrons, although with electron temperatures less than that reported by Malka *et al.* for similar laser parameters. In this case they also assume a $\mathbf{j} \times \mathbf{B}$ type process of electron generation.

Some years later the idea of resonance versus $\mathbf{j} \times \mathbf{B}$ acceleration was returned to by Santala *et al.* [56]. In this experiment, using 1 ps duration laser pulses, with intensities up to 3×10^{19} W/cm^2, the angular distribution of γ-rays produced by fast electrons as they propagate through millimeter thick copper backed tantalum targets was measured. The fact that the tantalum is both thick and high Z means that it acts as a very effective converter of MeV electrons into bremsstrahlung γ-rays. These γ-rays then enter an array of copper wedges placed in a semi-circle some centimeters from the target and centred on it. The high energy γ-rays induce a photoneutron reaction in the copper (converting ^{63}Cu to ^{62}Cu which is a β^+ emitter with a 10 minute half life). By measuring the resulting activity in each of these wedges a determination was made of the angular distribution of the

electrons generated at the front surface of the target.

Santala *et al.* changed the duration of the ASE pedestal in the laser pulse, effectively increasing the scale length of the initial plasma density profile. They report that as this scale length is increased the emission direction of the γ-rays, and thus the fast electrons, changes from the target normal to the laser axis direction. From this they determine that there is a change in the absorption mechanism for different density scale lengths. At short scale lengths the vacuum absorption mechanism dominates, injecting electrons along the target normal direction. As this density profile is changed the $\mathbf{j}\times\mathbf{B}$ mechanism begins to dominate and electrons are injected along the laser axis direction. To some extent this experiment helps explain the differences between the early results of Malka and Beg, given the substantial difference in intensity contrast. It also highlights the importance of not having an overly simplified view of the significance of different absorption process. Indeed a double distribution can clearly been seen in these results with electrons peaks along both the laser and target normal directions, suggesting the simultaneous acceleration of electrons by both the resonance and $\mathbf{j}\times\mathbf{B}$ mechanisms.

The decade following these results, with accessible laser intensities now exceeding 10^{20} W/cm^2, has seen a number of key developments in our understanding of laser absorption and fast electron generation. In particular, there has a been significant exploration of what might be termed 'secondary effects'. These include any effects which might enhance or modify the laser absorption or fast electron generation, such as the use of a controlled density gradient to induce relativistic self focusing [57] or other engineered conditions. Direct studies of the laser absorption mechanisms at this intensity level are more limited.

Ping *et al.* [58] reports one of the only studies to investigate absolute laser energy absorption for laser pulses $> 10^{20}$ W/cm^2, using an experimental setup not dissimilar to that used twenty years previously by Kieffer *et al.* [50], discussed earlier. An Ulbricht sphere was used to measure the scattered light while the back reflected light is measured using a calorimeter. Ping *et al.* demonstrate an overall increase in energy absorption with intensity. Scaling the laser intensity

from 10^{17}-10^{20} W/cm^2 they measure an increase in the absorbed fraction from 30% to, as high as, 90%. Using PIC simulations they also examine the dependence of absorption on the extent of the preplasma. With a limited preplasma they demonstrate moderately enhanced absorption. Also of note are measurements of the electron angular distribution. Much like Santala *et al.* there is a clear change in emission direction from target normal to the laser axis. While Santala *et al.* reported this change as a consequence of the changing level of preplasma, Ping *et al.* measure the change in direction as the laser intensity is increased. This change is attributed to the onset of the relativistic regime and the $\mathbf{j} \times \mathbf{B}$ acceleration mechanism. However, the changing level of preplasma with intensity cannot be easily decoupled. As Santala demonstrated, strong resonance heating does occur for relativistic intensities when the density gradient is sharp. In reality it is likely a combination of both effects which cause a change in the angular distribution of the fast electrons.

Overall, from the results presented which span both decades in time and multiple *decades* in intensity a complex picture of laser absorption and fast electron generation emerges. A single theory which can account simultaneously for all the aspects of absorption encountered in experiments does not yet exist. Presently the only recourse is to rely on an understanding which is essentially phenomenological in nature, nevertheless this does not prevent the exploitation of this limited understanding to refine key aspects of laser-solid interactions in the march towards useful applications.

In the next section the focus of the discussion will move on to some of the 'secondary effects' introduced earlier and studies which have exploited these effects to enhance laser absorption and fast electron generation.

3.2 Progress in schemes to enhance fast electron generation

The last section provided a description of the fundamental mechanisms of energy absorption and their sensitivity to laser intensity, polarisation and the initial

plasma density profile. Schemes which enhance absorption mechanisms through careful manipulation of these parameters would be inherently useful for applications such as fast ignition or laser-driven ion acceleration.

There are a number of routes one could take in attempting to enhance fast electron generation. In the literature there are certain commonalities which reveal three clear thematic areas. These themes consist of deliberate modifications to one or a combination of the following: laser parameters, plasma density profile or target parameters (such as material or structure).

3.2.1 The sensitivity of fast electron generation to large laser incidence angles

To a certain extent the previous section dealt with studies which have looked at driving changes in fast electron generation by increasing the laser intensity and changing the polarisation. However, other routes have been examined. Of particular relevance to the work presented in the following chapters are modifications made to fast electron generation by changes in the laser incidence angle.

Already established is the concept of looking at the angular distribution of the escaping fast electrons to reveal changes the mechanisms of fast electron generation, such as the work of Santala *et al.*[56]. In subsequent years there have been a host of studies which examined the angular distribution of the escaping fast electrons as the laser incidence angle is changed. For these studies it was important to examine not just the rear side, laser forward emission, but a full angular range of accelerated electrons.

One of the first to tackle this was Cai *et al.* [59]. Using sub-relativistic intensities of 10^{17} W/cm^2 and an array of thermoluminescent dosimeters (TLDs) surrounding the target to detect the escaping electrons they demonstrate the existence of a triple peaked distribution. One peak was measured along the target normal direction, due to resonance absorption, as would be expected at these intensities. The second was in the laser backward directions and the third was directed along the laser specular direction. This was taken a step further,

separately, by Li *et al.* [60] and Habara *et al.* [61], in both cases using stacked image plate detectors placed around the target. In the case of Li *et al.* a distinct change in the escaping electron distribution was measured as the incidence angle is increased. At 70° the emission appears as a jet of electrons directed along the target surface. At lower incidence angles the emission is predominantly along the laser axis direction. It is important to note however that the laser intensity in this case is barely in the relativistic regime and as already established there is a increasingly strong forward-directed component of fast electrons as the intensity is increased. The study of Habara *et al.* [61] following very closely after this and using a similar technique demonstrates this effect at higher intensities. Using intensities up to $\approx 1 \times 10^{19}$ W/cm^2 they find that as the intensity is scaled up for large incidence angles the specular component reported by Cai *et al.* [59] moves to become a strong surface directed component. In both of these studies then, at steep incidence angles, the angular distribution of escaping electrons is different from that established by Santala *et al.* and what might reasonably be expected from our understanding to date of the dominant $\mathbf{j} \times \mathbf{B}$ and resonant absorption processes.

Helpfully theoretical work by Nakamura *et al* [62], prior to these experimental studies, established a mechanism for this alteration in the standard fast electron generation processes. Nakamura *et al.* reports that for the $\mathbf{j} \times \mathbf{B}$ mechanism there is a strong component of fast electron directed along the laser direction. These electrons, as discussed in **chapter 2**, self-generate an azimuthal magnetic field. This generates a strong magnetic field along the target surface which increases with laser incidence angle. Electrons which would otherwise be injected into the target are instead reflected out into vacuum by this field. This causes a build up of negative space charge in vacuum and induces electrons to be accelerated back into the target surface region, enhancing the magnetic field. Consequently, these electrons which would normally form a component of the laser directed electrons are instead trapped on the target surface and oscillate along it spreading out to the target edge. According to Li *et al.*, above a certain incidence angle, the so-called critical angle, this field is reinforced so strongly that electrons can no longer

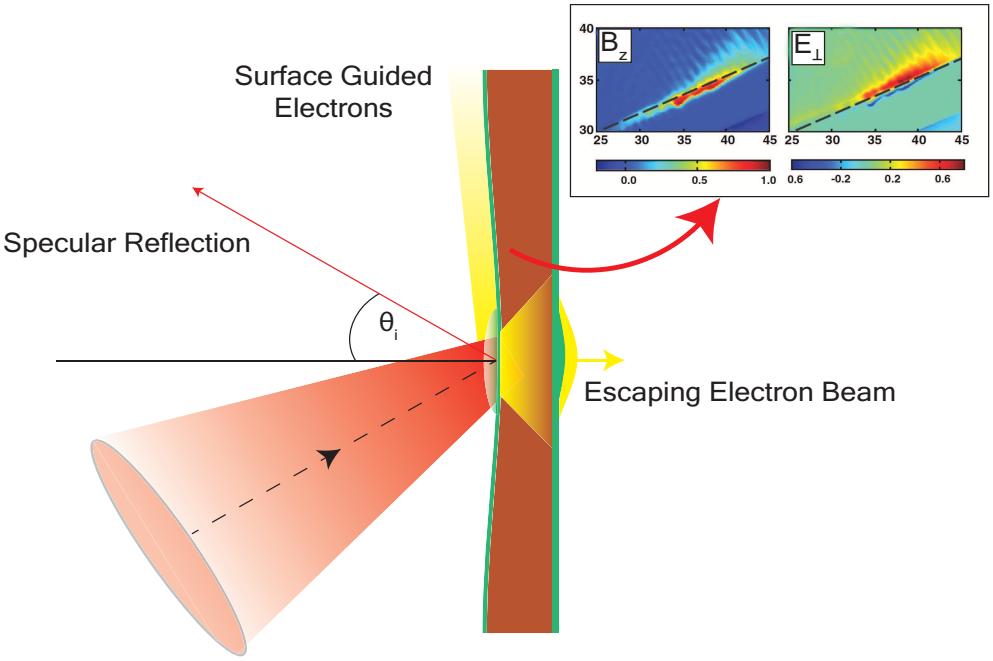

Figure 3.1: Schematic of the surface guiding mechanism as proposed by Nakamura *et al.* [62]. An obliquely incident laser pulse induces a strong magnetic field along the target surface, this field reflects electrons into vacuum. The resulting space charge field returns the electrons to the surface, reinforcing the magnetic field and trapping electrons along the target surface. The inset shows 2D-PIC simulations from Li *et al.* [60] of these quasi-static electric and magnetic fields.

penetrate into the target and instead are all directed along the target surface. A schematic of this effect is show in Fig.3.1.

This mechanism is a dramatic example of how small changes in the interaction conditions (changing incidence angle) can produce radical differences in the generation and transport of fast electrons. This effect will be returned to in **Chapter 5**.

3.2.2 Inducing changes in fast electron generation using controlled density gradients

Another parameter which has been shown to alter fast electron generation is the plasma density profile at the front surface of the target. As was clearly demonstrated in a number of studies highlighted in the opening section of this chapter, the density profile can be important in determining which absorption mechanism dominates. However, what has not yet been demonstrated is if this is

simply a binary switch over or if it is a gradual change, and indeed if an optimal density profile for given laser conditions exists. A number of authors have tried answer this question.

Theoretical work by Andreev *et al* [63] proposes a scenario in which a short pulse laser incident on a overdense plasma slab with no density gradient is poorly absorbed. Introducing a small density gradient is then shown to increase the absorbed fraction. It is then predicted that there exists a peak density gradient for a given set of laser parameters. Beyond this localised peak, at longer density scale lengths there is a small decrease in absorption and then a global increase as the density scale length is further increased. Furthermore, 2D effects are also shown to play a role in increasing absorption. For high laser intensities, the ponderomotive pressure at the relativistically corrected critical density surface induces a surface curvature due to the Gaussian nature of the laser focal spot. This curvature in effect introduces a range of additional incidence angles to the interaction which enables additional absorption mechanisms such as resonance or vacuum heating to take place.

Experimental evidence for a confirmation of such a complex scaling behaviour is limited. The one study which does indicate the onset of an optimum density scale length is that of McKenna *et al.* [28], where a controlled plasma expansion is driven by a secondary nanosecond pulse. Scanning this long pulse beam in intensity changes the initial plasma density profile. Measurements of ion acceleration, which are sensitive to absorption and fast electron generation, show a local maximum for a given long pulse intensity. This study shall be returned to in some detail in **Chapter 6**. Other studies, while not necessarily demonstrating this local peak do often show an overall enhancement in absorption. Separate studies by Ma *et al.* [64] (experimental), Ping *et al.* [58] (experimental) and Nuter *et al.* (simulations) all show a general increase in absorption and fast electron generation with increasing levels of preplasma.

3.2.3 Sensitivity of fast electron generation to target material parameters

While the previous section focused on driving changes in fast electron generation using a controlled density gradient, this section considers how the target material itself can effect, and even enhance, fast electron generation.

There are a number of target parameters which may drive changes. Both target material [55] and front surface structure [65, 66] have been demonstrated as possible routes towards enhanced fast electron generation. However in recent years an exciting new regime, which breaks somewhat with the regimes of absorption already described above, has been established.

For highly relativistic laser pulses and targets with nanometer scale thickness it is possible for the target to become relativistically transparent to the laser pulse. As the laser pulse interacts with the target, electrons are initially ejected from the focal spot by the $\mathbf{j} \times \mathbf{B}$ mechanism. The high intensity laser pulse causes a large number of electrons to reach relativistic velocities, therefore increasing their mass and decreasing the plasma frequency by the Lorentz factor γ. In conjunction with the overall more limited, compared to thicker targets, number of electrons available and some degree of target expansion the target rapidly becomes transparent. In this case, unlike conventional absorption mechanisms where the influence of the laser pulse is restricted to densities below that of the relativistic critical surface at the front of the target, the entire target bulk can feel the influence of the laser pulse. A number of early studies related to this mechanism have been conducted. For example, Henig *et al.* [67], motivated by the theoretical work of Yin *et al.* [68], experimentally demonstrate the onset of the transparency regime by measuring ion acceleration. They find for ultrahigh contrast pulses and targets of 30 nm irradiated with pulses of intensity 7×10^{19} W/cm^2 an exceptionally high cut-off energy of 185 MeV for C^{6+} ions. Supported by PIC simulations the onset of relativistic induced transparency leading to an enhancement in fast electron numbers and consequently the accelerating ion field is inferred. More recent studies of this regime [69–71] have further demonstrated

that it leads to an enhancement in fast electron generation. This effect will be returned to in detail in **Chapter 7**.

3.3 Summary

In summary, the absorption of short pulse high intensity laser light and subsequent energy conversion in solid density targets into high energy electrons is a complex dynamic process which is sensitive to a wide range of laser and target parameters. These parameters, in reality, often act in conjunction to produces effects which currently cannot be accounted for by a single theory of absorption into overdense plasmas. Nevertheless, after over twenty years of studying such coupling effects a great deal of progress has been made. The current state the art in the field shows that there is a great deal of potential to drive forward the prospect of applications of laser-solid interactions by exploiting, optimising and developing our current understanding of fast electron generation. The data to be presented in the following chapters stands as an example to that endeavour.

Chapter 4

Methodology: Lasers, diagnostics and simulation

In previous chapters the fundamental physics underpinning laser-solid interactions in general and the interaction at the target surface specifically were discussed. Such theoretical models, however, are worth little if they cannot be shown to be related to the real processes occurring in nature.

In this chapter we will initially describe some of the laser systems available in the United Kingdom and around the world with which ultra-intense laser-solid experiments are performed. From here some key diagnostic techniques, specifically relevant to the data presented in **Chapters 5-7** are detailed. In the final section of this chapter common numerical modelling techniques, often used in the analysis and deconvolution of experimental data, are discussed.

4.1 Overview

The values of any great society are moulded into the monuments they build. The pyramids symbolise ancient Egypt. The Colosseum, Rome. The Parthenon, ancient Greece. We live in an age of "big science" and future generations looking back will perhaps view our greatest monument, the structure which might symbolise our society as the Large Hadron Collider, the Saturn V rocket or even the National Ignition Facility (NIF) and be inspired to continue the scientific endeav-

our. Of course, "big science" has a role to play not only as symbolic monuments to the values of an enterprising society but as centres for pioneering research. The facilities in which laser-solid experiments are carried out certainly match this description, offering the potential for ground breaking research using some of the most intense sources of light on Earth.

Comparing such facilities to the "big science" projects of the recent past, although they often cost into the tens of millions of pounds, is perhaps not the best analogy. These facilities often involve tens or hundreds of people rather than the tens or hundreds of thousands of people involved in the development of the Saturn V rocket for example. Not that this reflects, in any way, upon the quality of science that can be undertaken at such facilities. On the contrary, such "intermediate scale" projects often provide the kind of flexibility and adaptability that is simply not possible on larger scale projects. The growth of the field of laser-solid interactions in the past decade is certainly attributable, at least in some part, to the flexible access provided by these institutions, which enables experimentalists to test new theories within months of being published.

Experiments at such facilities are often performed by a group of visiting researchers and last anywhere from a single week up to several months. Day-to-day running, including oversight of the diagnostics, preparation of the vacuum chamber and the request for laser shots often falls to an experienced student or post-doctoral researcher. General guidance and the overall vision for the experiment is provided by the principle investigator (PI) who is often, but not exclusively, a senior academic.

The early planning stages of the experiment attempt to reconcile the objectives set out in the experiment proposal with the reality of actually carrying out the measurements. The success of any experiment depends to a large extent upon how well this planning process is carried out and the extent to which fall back objectives and backup plans are built into the design. This process is in essence the attempt to reconcile the shared interest of achieving the scientific objectives of a given experiment with the realistic implications for a large facility with limited resources and multiple demands, from many research groups, on those resources.

No experiment should be so high in risk that it is a danger to the facility or the health of the experimenters or be so demanding that carrying out the experiment will be seriously detrimental to other, current and future, experiments. Yet, it must be that we always aim to do more and gain deeper insights than before, we must be in essence "an idealist without illusions". Coming to an arrangement which meets all of these points often takes many months of discussion and design.

Once begun, typical experiments involve 1-3 weeks of constructing the various diagnostics to be used on the experiment as well as constructing the optical and mechanical systems necessary to position the target at the focus of the laser. This point, where the best focus of the parabola is positioned, is often called the target chamber center (TCC) - although it is not necessarily the center of the chamber. Once this has been carefully defined, diagnostics can be installed, using this point as a reference for all other points in the chamber. Often experiments will use either a second laser (such as a long pulse beam or a second short pulse beam) or a probe beam taken by sampling a small part of the main beam. In either case, the timing of these additional laser pulses to the primary pulse is another important task carried out during the setting up of the experiment.

Following the setting up period, the experiment moves tentatively into a mode of firing laser shots and collecting data. Typically, some initial shots, using simple targets, are taken to check that the diagnostics are all working correctly. If not, realignment and sometimes rebuilding takes place. Once all is working the focus turns to achieving the most number of high quality shots in the time available and tailoring those shots based on the results in order to better understand the interaction, achieve the objective of the experiment and reveal new physics.

4.2 High Power Laser Technology

The technique which has undoubtedly revolutionised laser-plasma interactions is chirped pulse amplification (CPA). This approach enabled, for the first time, laser intensities beyond 10^{18} W/cm^2 to be reached and, as a result, experimental investigations of relativistic plasma physics to be made.

The original problem of reaching these intensities is one of energy fluence. Efficient amplification of a laser pulse requires that, prior to the amplifiers, the fluence be close to the amplifier saturation fluence - which can be defined as

$$\Gamma_s = \frac{\hbar\omega_L}{\beta\sigma_{21}} \tag{4.1}$$

where $\hbar$ is Planck's constant, ω_L is the laser angular frequency, β is a dimensionless quantity related to the decay rate of the lower laser energy level and σ_{21} is the optical gain cross-section. For a Ti:sapphire laser Γ_s is of the order of a few Joules per centimeter square. For pulses of 30 fs duration, intensities of 10^{13} W/cm^2 are reached which is easily high enough to induce damage to the amplifier and optical components further down the beam line. Moreover, due to non-linear optical effects such as self-phase modulation and self-focusing caused by the optical Kerr effect, laser intensities beyond the damage threshold can be reached with lower fluences.

The potential for damage caused by non-linear optical effects is often characterised by the "B-integral" which is best defined with reference to the intensity dependent refractive index

$$n = n_0 + n_2 I \tag{4.2}$$

where $n_2 I$ is the intensity dependent part of the refractive index. Likewise the accumulated phase after a propagation distance L can be defined as

$$\phi = \frac{2\pi}{\lambda}\int_0^L n(z)\,\mathrm{d}z \tag{4.3}$$

$$= \frac{2\pi}{\lambda}\int_0^L n_0 I(z)\,\mathrm{d}z + \frac{2\pi}{\lambda}\int_0^L n_2 I(z)\,\mathrm{d}z \tag{4.4}$$

The second term of the phase, the intensity dependent part, is known as the "B-integral"

$$B = \frac{2\pi}{\lambda}\int_0^L n_2 I(z)\,\mathrm{d}z \tag{4.5}$$

Typically the laser intensity varies transversely across the beam front (whether with a Gaussian profile or otherwise), with the highest intensity part being in the middle of the beam, decreasing out to the wings. Such a profile, with sufficiently high intensities, leads to the wings of the beam accumulating more phase than the central bright spot. In other words, the lower intensity regions travel faster in the medium than the higher intensity regions resulting in a focusing effect. The potential for damage to optics therefore is greatly increased, even for laser pulses which are initially below the damage threshold.

As we have seen in previous chapters however, intensities several orders higher than this are required to enter the relativistic regime of laser-plasma interactions. The chirped pulse amplification technique enables such high intensities to be achieved.

Initially a short input pulse is generated and passed into a pair of diffraction gratings which act to disperse the spectrum and therefore stretch the pulse, often stretch factors of 10^3 to 10^5 are used. Pulse stretching is used to reduce the fluence below the damage threshold of the amplifying medium such that the pulse can be safely amplified without encountering the non-linear effects discussed previously. The, now significantly longer, laser pulse is amplified - often in multiple stages. In CPA laser chains this process can be quite complicated, with stages of pre-amplification before the pulse is amplified with larger amplifiers (for the same reasons as given earlier and described by Eq.4.1). Two amplification techniques are commonly employed. First a so-called regenerative amplifier is used. A schematic of this technique is shown in Fig.4.1.

Initially the stretched laser pulse is injected through a polariser, a half-wave plate and a Faraday rotator. Assuming the incoming beam is s-polarised initially passing through the half-wave plate (which is at 45° to the plane) rotates the polarisation to p-polarised. Passing through the Faraday rotator rotates the polarisation again by an amount depending on the length, the external magnetic field and the Verdet constant of the material. The pulse now passes through a second polariser which is set to reflect s-polarised light and transmit p-polarised light. Upon reflection the input pulse enters the Pockels cell (in this case with

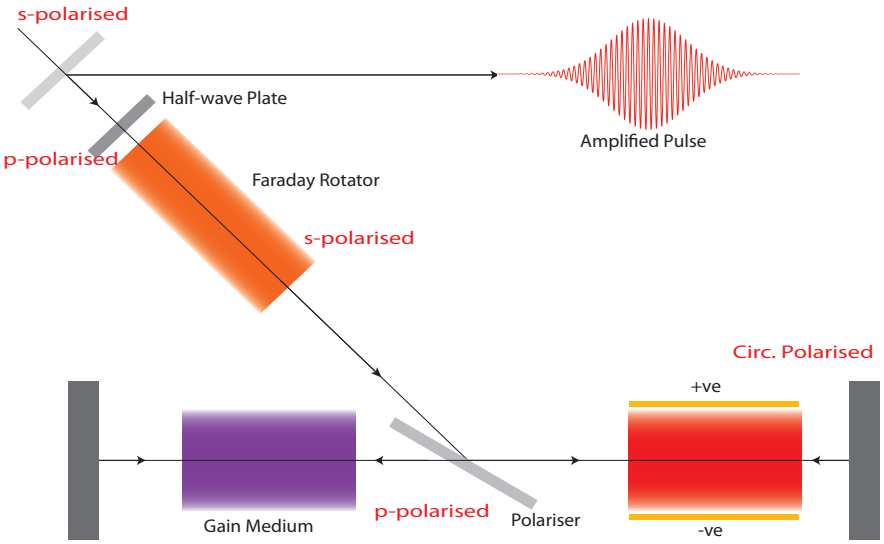

Figure 4.1: Schematic of typical regenerative amplifier used in early stages of CPA beam lines

s-polarisation). The Pockels cell voltage is set to the so-called "quarter-wave" voltage - causing it to behave like a quarter-wave plate. The pulse leaves the Pockels cell with circular polarisation, upon reflection from the cavity mirror the rotation direction is reversed. A second pass through the cell has the cumulative effect of single pass through a half-wave plate, resulting in a p-polarised pulse leaving the Pockels cell. Since the polariser transmits p-polarised light the pulse can pass into the part of the cavity with the gain medium. After passing through the gain medium the amplified pulse reflects from the second cavity mirror and makes a second pass. This process is repeated a number of times (perhaps as many as 20 round trips). In order to switch the pulse out of the cavity, the voltage across the Pockels cell is reduced so there is no rotation of the polarisation, resulting in the pulse being immediately reflected back out of the system by the polariser. An important note to make for this type of amplifier is that the gain medium should not be over driven as self-lasing can be induced. This effect is often a major component of the amplified spontaneous emission (ASE) in the system, a phenomenon which will be discussed in more detail in the following sections.

A second type of commonly used amplifier in CPA laser chains is the so-called multi-pass amplifier, where the input laser pulse is reflected off of a series of mirrors, with each reflection resulting in another pass through the gain medium. A schematic of this is shown in Fig.4.2. While this technique has a lower gain effi-

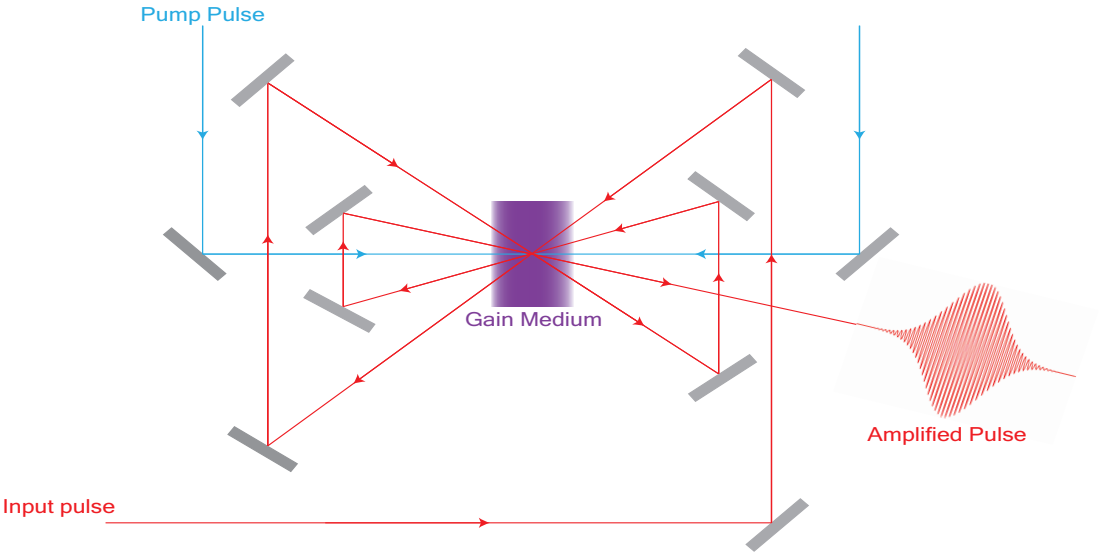

Figure 4.2: Schematic of typical multi-pass amplifier used in early stages of CPA beam lines

ciency than the regenerative amplifier technique (the medium has to be pumped harder), the single pass gain can be set much higher as the beam does not have to pass through any optics where B-integral could be an issue. For this reason, multi-pass amplifiers are typically set to be the final amplification stage in the CPA laser chain, often called the 'power amplifier'.

The next stage of the CPA technique is to take the now amplified, stretched pulse and compress it back to a pulse length of the order of the original input pulse. This is done by using a set of gratings which have the opposite dispersion as the stretcher gratings. The result now is a short, high energy laser pulse which can be reliably reproduced without much fear of damaging the laser optics with each pulse created. The final step, although not unique to CPA, is to focus the pulse onto target with a focusing optic. Again for reasons related to self-focusing and B-integral a parabolic mirror instead of a lens is often used. The whole CPA process is drawn schematically in Fig. 4.3.

4.2.1 Amplified Spontaneous Emission

An important side effect of these amplification techniques is the production of "amplified spontaneous emission" (ASE), previously introduced in **chapter 2**. Consider the gain media drawn in either Fig.4.1 or Fig.4.2 without the cavity

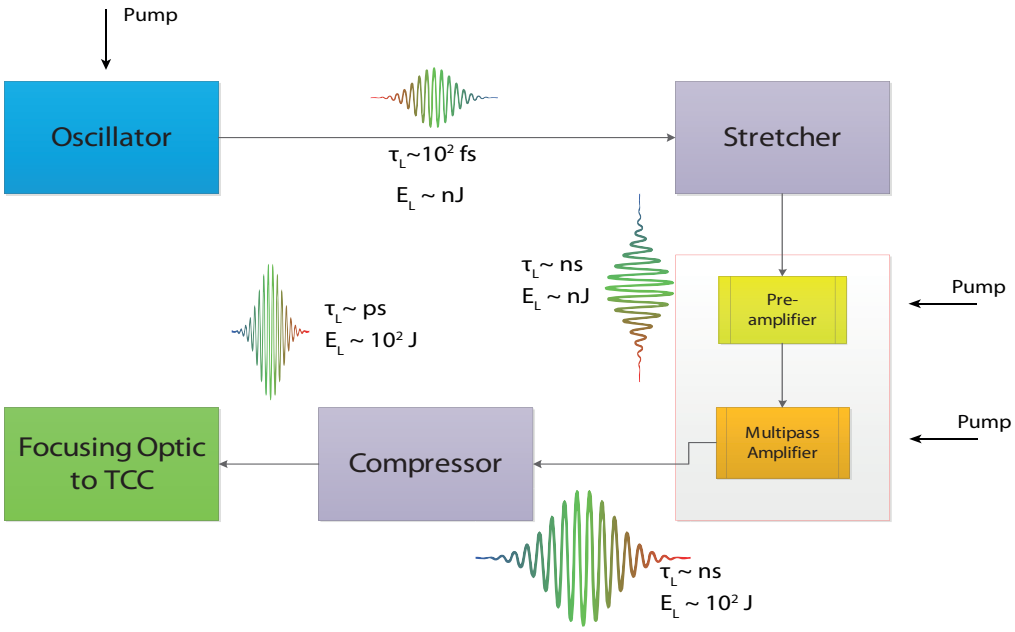

Figure 4.3: Simplified flow diagram of the laser pulse propagation through CPA laser chain.

mirrors. The pump beam will cause a population inversion in the material. After a certain lifetime these electrons will decay with a spectrum related to the line width of the decay transition, emitting radiation in all directions. A portion of that radiation is emitted at a large angle to the central axis. This light will quickly escape the gain medium without much amplification. Alternatively, consider the portion of the radiation which is emitted at small angle to the central axis, at one end of the gain medium. These photons will travel along the length of the gain medium, being amplified along the way and escape at the ends of the amplifier. This effect is shown in Fig.4.4. This is true for both directions along the amplifying rod, as such there will be forward and backward directed components of the ASE.

While ASE is present in most laser amplifier designs, the fact that the intensity of the current generation of large-scale CPA lasers used for intense laser-plasma interactions is often beyond 10^{20} W/cm^2 means that the level of ASE becomes important. For instance, even if the level of ASE production is 8 orders of magnitude lower than the level of stimulated emission (the main laser pulse), once focused onto target the intensity would still be 10^{12} W/cm^2 - enough to cause significant ionisation and plasma expansion at the front surface of the target prior

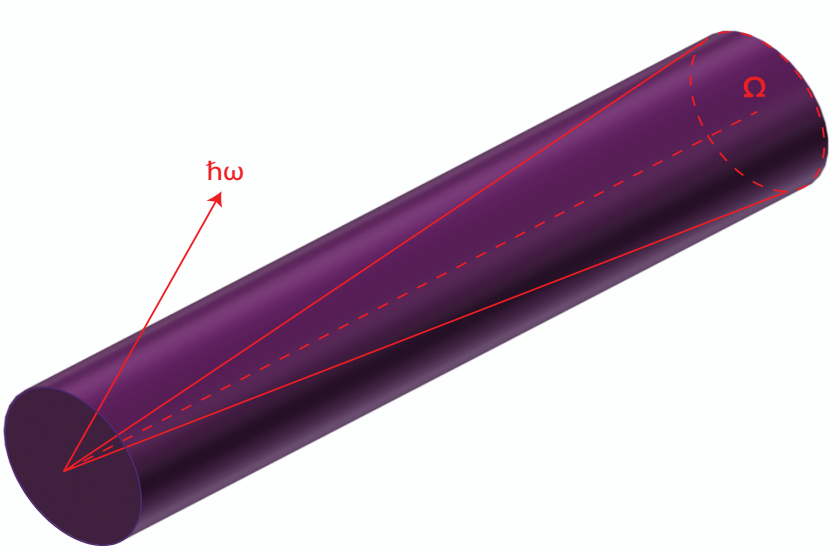

Figure 4.4: Schematic of ASE emission direction in a rod amplifier. Where photons either escape into 4π and see little amplification or into Ω and experience amplification along the whole length of the rod.

to the arrival of the main laser pulse. This parameter, the ratio of the main pulse intensity to the ASE intensity, is called the "laser contrast" and plays a critical role in determining the behaviour of the laser-plasma interaction (this will be discussed further in following chapters).

The temporal intensity profile of the laser pulse therefore determines, to a large extent, the initial conditions of the laser-plasma interaction. If the ASE level is too high there will be a very large amount of plasma on the front surface and if the ASE is early enough the resulting shock wave could potentially destroy the target before the main pulse even arrives. The leading edge of the ASE arrives on target nanoseconds before the main pulse. The majority of the ASE can be gated out with the help of a Pockels cell although this is limited to a minimum gating time of approximately a few hundred picoseconds, and so there is always some level of ASE transmitted through the system and onto target.

If the laser contrast inherent in the system cannot be improved easily then additional *in situ* measures are often employed before the main interaction point to suppress the ASE, often by using some kind of intensity filtering technique. One such technique is the use of a frequency doubling crystal. Since the crystals doubling efficiency is intensity dependent the majority of the main pulse is dou-

bled efficiently while the majority of the ASE is not. By using a dielectric mirror with a high reflectivity in the second harmonic and low in the first harmonic the unconverted laser energy can be dumped. The same technique can be employed for higher harmonics if required and may improve the contrast further still since higher order crystals require a still higher electric field for frequency conversion.

The second technique appears, initially, slightly incongruous with the whole concept of CPA. The aim there is to prevent damage to optical components by high intensity laser pulses. So-called "plasma mirrors" however take the opposite approach. Here the low intensity component proceeds the main pulse in time. The plasma mirror technique uses a high quality glass slab which will allow intensities on the order of the ASE to pass through. Some nanoseconds later, when the rising edge of the main pulse arrives the intensity is sufficient to ionise the surface and form a plasma. The peak of the pulse is then reflected from this plasma surface. In this way the plasma mirror acts as an intensity filter. Allowing the low intensity component to pass and reflecting the high intensity components. Plasma mirrors are not 100% efficient however instead values of 50-60% of the main pulse reflected are often given [72]. Nevertheless the improvement in laser contrast can be as much as two orders of magnitude. Improving the contrast even by this relatively small amount can change the interaction completely. This is especially true for applications such as high harmonic generation but, as shall be shown in following chapters, also for fast electron generation and ion acceleration.

4.3 High Power Laser Facilities

The problems of producing, stretching, amplifying, compressing and focusing laser pulses are, as has been described in the previous section, numerous and difficult. Despite this there are a large number of laser facilities around the world capable of generating short, high intensity laser pulses with intensities above 10^{18} W/cm^2.

Different facilities have found different solutions to apparently similar technical problems. In this section we will focus on three laser systems in particular

which are very relevant for **Chapters 5-7**. First, the petawatt arm of the VULCAN laser at the Rutherford Appleton laboratory (RAL) in Oxfordshire. Second the PHELIX laser based at the GSI laboratory in Germany and finally the Astra-Gemini laser also based at RAL.

4.3.1 VULCAN-PW

The petawatt arm of the VULCAN laser is one of the first of a generation of lasers nominally capable of generating petawatt (10^{15} W) pulsed power. As previously described the laser pulse starts in a mode locked oscillator which is used to generate ultra-short (fs) pulses. In VULCAN-PW this is a Ti:Sapphire laser medium which is pumped by a Nd:YAG laser. A train of 120 fs long, 1053 nm (with a 15 nm bandwidth), 5 nJ pulses with repetition rate of 80 MHz is produced from the oscillator. A single pulse is then gated out for stretching and amplification. Once the pulse has been selected out it is passed through the VULCAN-PW stretcher which consists of two reflective diffraction gratings and three lenses in a so-called "Offner triplet" configuration. This configuration is used to reduce, as much as possible, spectral aberrations in the pulse which will affect recompression further down the chain. After a first pass through the stretcher the pulse is dispersed from the initial 120 fs to 2.7 ns At this point it is sufficiently dispersed to be passed to the pre-amplifier, optical parametric amplifier system.

This technique (OPCPA) is different to those described previously and has some serious advantages over the conventional laser amplifier. In this scheme a so-called signal pulse (the pulse from the compressor) is passed through a non-linear crystal in the presence of a higher frequency, higher energy pump pulse. The interaction of the pump and signal pulse and the non-linear crystal results in the generation of a third frequency pulse called the idler. Also in this interaction there is net energy transfer from the pump to both the signal and idler pulse. In this way this technique is used to amplify the signal from the compressor in VULCAN-PW. The major advantage for this technique over more conventional laser amplifiers is three fold. First, the energy transfer between the pump and the signal is very efficient with very little heating produced in the crystal. This means

(a) (b)

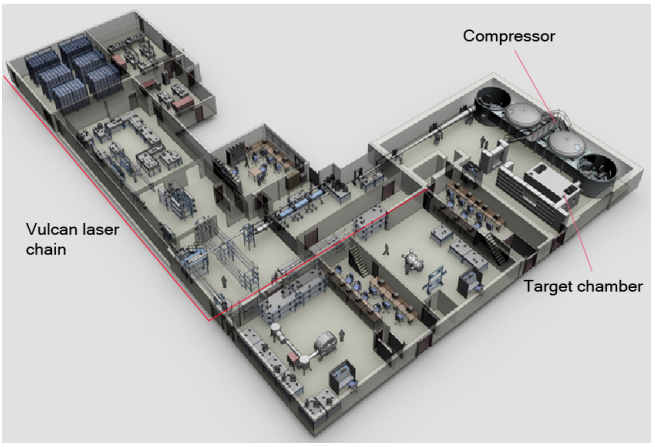

(c)

Figure 4.5: (a) Showing the target area petawatt (TAP) chamber before addition of radiation shielding. The compressor chamber is also visible on the left hand side of the image. (b) TAP chamber with radiation shielding (c) Overview of VULCAN laser system.

that the common effect of thermal lensing in amplifiers, where there is a refractive index profile across the crystal which causes focusing and possibly damage, is no longer an issue. Second, since parametric amplification can amplify pulses with very large bandwidth [73] the effect of gain narrowing is much reduced i.e the effect of amplifying the central frequency of the dispersed pulse much more than the wings. The result is a pulse which is much more effectively recompressed after amplification. Finally, and critically for laser-solid interactions, using the non-linear crystal as an amplifying medium does *not* lead to the generation of ASE resulting in a very clean pulse with which to do laser-solid experiments. After pre-amplification the pulse is passed back into the stretcher and spectrally dispersed further to a pulse length of 4.8 ns. At this point the pulse is passed to the main amplifiers for VULCAN-PW. These consist of a set of rod and disk amplifiers.

Initially the pulse enters a set of Nd:glass, rod amplifiers which are pumped by white light flash lamps. The diameter of the beam is gradually increased as it is amplified so that the intensity is kept below the damage threshold of the gain medium. The final set of amplifiers in VULCAN-PW are large diameter disk amplifiers, also pumped by flash lamps, bringing the pulse energy up to $\approx$ 650 J. The final step before focusing onto target is to recompress the pulse from 4.8 ns to $\approx$ 500 fs. The VULCAN-PW compressor consists of two 940 mm diameter gratings. The output pulse from the amplifiers is expanded up to reduce the energy fluence per unit area on the optics. The beam is initially turned with a large turning mirror onto two diffraction gratings with the exact opposite dispersion as the gratings used in the stretcher described earlier. The pulse is now recompressed, with a diameter of 600 mm and turned into the interaction chamber with a second large turning mirror. Finally a third turning mirror directs the beam onto a large, f/3.1, off axis parabola (OAP) which focuses the beam into a best focal spot of $\approx$ 4 μm resulting in a peak intensity on target of up to 10^{21} W/cm^2.

4.3.2 PHELIX

The PHELIX laser based at the GSI laboratory near Darmstadt, Germany is also an Nd:Glass laser operating at 1053 nm. Uniquely this laser offers the ability to direct the high energy protons generated from the target foil into a conventional particle accelerator, forming part of the so called LIGHT (laser-ion generation, handling and transport) project, with the aim of exploring a future interface between laser-plasma and conventional accelerators in, for example, the medical treatment of tumours with ion beams.

PHELIX initially generates a 100 fs, 4 nJ pulse which is stretched and amplified using a pair of regenerative amplifiers as described previously, increasing the pulse energy up to 30 mJ. Next the pulse is passed to a series of three pre-amplifiers which increase the pulse energy to $\approx$5 J. The beam is then expanded up to 70 mm to maintain the energy fluence below the damage threshold. The pulse is then passed onto the main amplifiers in the chain. These consist of five

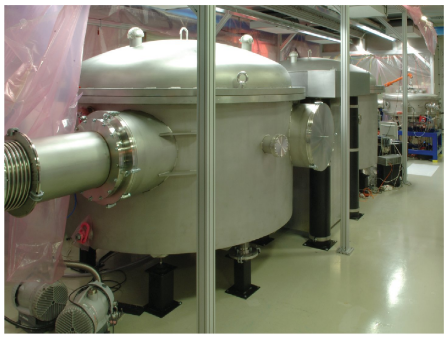

(a)

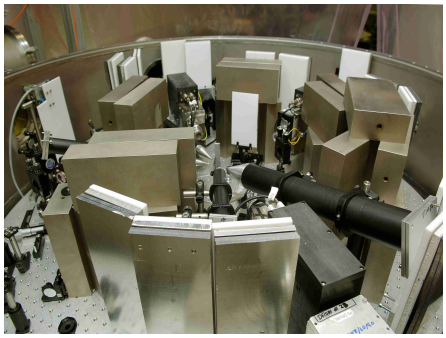

(b)

Figure 4.6: (a) Compressor chamber for the PHELIX laser. (b) Target chamber of PHELIX, including diagnostics and radiation shielding.

Nd:glass cassettes which potentially enable amplification up to 250 J. However, radiation safety levels limit this energy to $\approx$ 120 J.

Once the pulse is amplified it is passed on to the compressor which compresses it down to $\approx$ 600 fs. The final optic in the system is a f/6.7 copper coated 90-degree off-axis parabolic mirror of diameter 300 mm and focal length 2 m. Due to the large f-number a focal spot of only 15 μm in diameter is achievable, combined with a throughput from the compressor of 79% the peak intensity on target is typically of the order 10^{19} W/cm^2. Critically due to the use of regenerative pre-amplifiers, in addition to the main multi-pass amplifiers as opposed to the OPCPA technique fielded on VULCAN-PW the laser contrast on PHELIX is of the order 10^5-10^6 compared to the 10^8-10^{10} contrast level available on VULCAN-PW.

4.3.3 Astra-Gemini

The Astra-Gemini laser based at the Rutherford Appleton Laboratory, UK is different in a number of respects as compared to the previous two laser systems

discussed. Instead of Nd:Glass, the gain medium in this case is Ti:Sapphire. Unlike Nd:Glass, Ti:Sapphire has a very large gain bandwidth as a result a larger number of frequencies can be amplified and compressed resulting in the production of significantly shorter pulse length on the order of tens of femtoseconds. The gain bandwidth in this medium is optimised for 800 nm. Astra-Gemini consists of four amplification stages. The first three stages constitute the "Astra" laser, producing an 800 nm, 45-50 fs pulse containing ≈1.5 J. The Gemini laser is in reality the fourth stage of amplification for the Astra pulse. Gemini is designed for dual beam capability, as such the input pulse from Astra is split equally in two. The amplification is then simply a multi-pass amplifier as described previously, except that a Ti:Sapphire crystal is used instead of Nd:Glass. After amplification the pulse contains 15-20 J. Once amplified, the 1.06 ns pulse is passed to the compressor which is of a similar double-pass design to the VULCAN-PW compressor. The output from the compressor is typically a pulse of 40 fs in duration and containing 12 J.

The intensity contrast at the nanosecond level is of the order 10^{10}-10^{11} and 10^{4} at 1 ps from the main pulse. However through the use of a retractable double plasma mirror system the picosecond contrast level is improved to 10^{6} enabling experiments using ultra-thin nanometer scale targets.

Finally, the pulse is focused using an f/2 off-axis parabola to TCC in a focal spot of diameter ≈1.5 μm. The design specification for Gemini was for a dual beam laser system with 0.5 PW in each arm capable of 10^{22} W/cm^2 on target. Reaching these intensities is however an ongoing project and currently typical experiments with the f/2 parabola will achieve intensities of 0.5-1x10^{21} W/cm^2.

4.4 Laser-Plasma Diagnostic Techniques

With a description of how the intense laser pulse is generated and focused onto the target, our understanding of the implementation of a laser-solid experiment has reached as far as the beginning of the interaction itself. In order, now, to gain insight into how the rest of the interaction is measured experimentally some

of the multitude of diagnostic techniques employed during laser-solid interactions will be described.

In general these techniques break down into five main subcategories. One, ion imaging and spectroscopy, those techniques where the spectral and spatial information of protons and heavier ions are resolved. Two, x-ray imaging and spectroscopy, techniques where x-ray spatial and spectral information are resolved. Three, electron imaging and spectroscopy, techniques where the spatial and spectral details of emitted electrons are resolved. Four, absorption diagnostics, where the scattered or specularly reflected laser light is resolved, both spatially and spectrally, in order to infer the overall laser absorption into the target. Finally, five, nuclear techniques where the by-products of nuclear reactions, induced by the production of radiation during the main interaction, are measured in order to indirectly reveal some aspect of the overall interaction. In the following sections specific techniques inside these various subgroups will be described in more detail.

4.4.1 Fast Ion diagnostics

One of the key diagnostic techniques in recent years has been the measurement of the spatial and spectral information contained in the ion beam accelerated from the target during the interaction. Two techniques are particularly widely used. Firstly, dosimetry film stacks and, secondly, Thomson parabola spectrometers.

RCF

In the first case a proton sensitive (also x-ray and electron, for higher fluxes) film known as Radiochromic film (RCF) is layered one on top of the other. It is also very common to intersperse this "stack" of film with a filter of higher proton stopping power such as iron.

When a proton stops in matter it deposits the majority of its energy in a highly localised region called the Bragg peak, as shown in Fig.4.7(b). Unlike photons or electrons, protons (as well as heavier ions) deposit only a small amount of energy as they travel through the material. As the proton loses energy, the interaction cross section increases resulting in the proton losing more energy and increasing

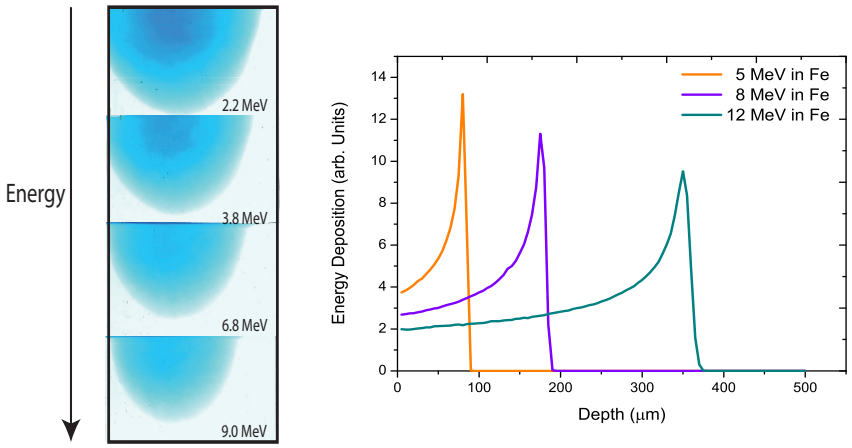

(a) (b)

Figure 4.7: (a) Typical result of RCF exposure to proton beam (b) Bragg peak of 12, 8 and 5 MeV protons stopping in iron.

the probability of an interaction. This avalanche-type effect results in the proton stopping very suddenly at a given penetration depth.

The RCF stack technique takes advantage of this effect by using discrete layers of film of known thickness, in addition to filters of known thickness. A proton corresponding only to a certain narrow energy band will stop in a particular layer of the stack and so the energy spectrum of the protons in the proton beam can be measured.

In addition to measuring the proton energy, if the RCF stack dimensions are large enough, the beam profile and total dose can also be measured. A typical image of an RCF stack after exposure to the proton beam is shown in Fig.4.7(a). In these images the proton beam has changed the optical density of a dye which makes up the film producing a blue colour. The deposited proton dose in a given piece of RCF can be characterised using an optical scanner, in transmission, by the optical density which can be expressed as

$$OD = -log_{10}(I/I_{BD}) \tag{4.6}$$

where I is the signal for a given pixel and I_{BD} is the maximum value possible for a given bit depth e.g 65535 for a 16-bit scanner. Using this technique on a piece of RCF exposed to a known proton dose by a well characterised conven-

tional RF proton accelerator provides a calibration that enables the calculation of the dose found on pieces of RCF exposed in laser-solid experiments. Usually this calibration film is cross calibrated with a standardised colour film such as the Kodak Q60 film [74], as long term light exposure of RCF can change the background optical density. While RCF is an extremely good beam profiler the energy resolution is limited. The highest possible energy resolution provided by a stack of pure RCF is ≈ 1 MeV due to the inherent thickness of a single piece of the film. Other techniques, such as the Thomson parabola spectrometer, offer much higher energy resolution by sacrificing this spatial information.

Thomson Parabola Spectrometer

The beam of charged particles accelerated from solid density targets consists of protons, heavy ions, electrons and neutral atoms (which have been accelerated as ions and then undergone recombination). The Thomson parabola spectrometer (TP-Spec) is a technique which is often used to separate, the charge-to-mass ratio of the ion beam and measure the energy spectrum.

The most basic design consists of a pair of high field strength permanent magnets and a pair of, usually, copper plates. The copper plates are attached to a high voltage power supply to generate a strong parallel electric field. Typically voltages of upward of 5 kV with a plate separation of ≈ 2 mm are used, giving an electric field on the order of 2.5×10^6 V/m. High magnetic field strengths of 0.6-1 T are achieved by using two NdFeB poles 5 mm apart. A small solid angle of the ion beam is selected using a pinhole. This limits the angular acceptance into the spectrometer, improving the energy resolution and also reducing the overall particle flux which would otherwise be too high for the detector. The selected ion beam moving perpendicular to both the magnetic and electric field is deflected. According to the Lorentz force equation the ions are bent vertically in the horizontal magnetic field. This acts to separate the ion beam by energy. The ion beam now enters the electric plates, here the deflection is in the horizontal plane. Even though the deflection is proportional to q/m, the charge-to-mass ratio, in both the electric and magnetic fields, since the deflection directions

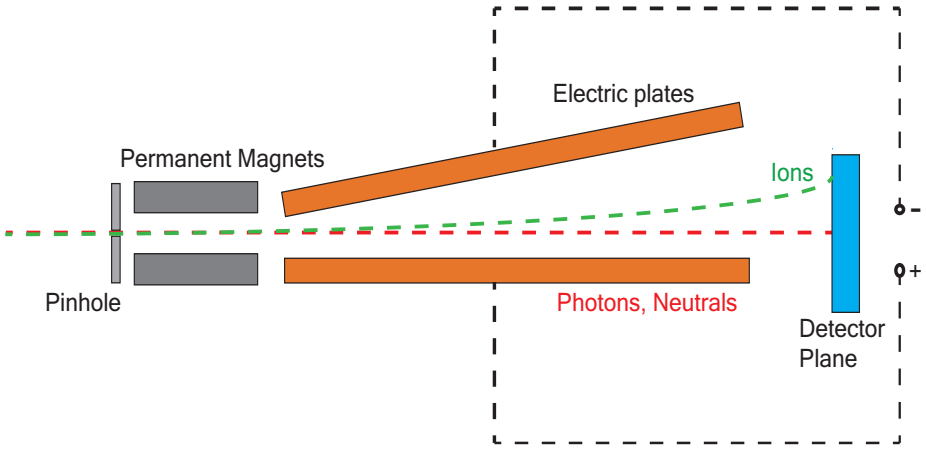

Figure 4.8: (a) Typical Thomson parabola spectrometer layout.

are different in the two fields, multiple ion charge states can be separated and resolved based on their q/m and their resulting energy spectra resolved with the combined deflection in both the magnetic and electric field. The major limiting factor on this technique is when trying to measure ion beams that contain ion states, although of different species, with the same q/m value; such as O^{8+} and C^{6+} . Another limiting factor is, when electrons enter the plates they are deflected much more strongly than the heavier ions and will often crash into the plates, causing variations in voltage and changing the deflection of other species. In order to avoid this a novel technique was developed in which one of the plates are angled [75]. A schematic of the TP-Spec layout is shown in Fig.4.8.

The detection media used in the TP-Spec is often one of three possibilities: Image Plate (IP), California-Resin 39 (CR-39) or a Multi-Channel Plate (MCP). The use of multichannel plates for ion detection is not described here because MCPs were not used in the experiments reported in this thesis but is covered in detail by Prasad *et al.* [76].

CR-39 is a polymer based material in which an incoming ion will induce damage. The ion will penetrate to a certain depth dependent on its energy, for same reason as described when discussing RCF. By etching with a sodium hydroxide (NaOH) solution to remove the top layer of the CR-39, the locations where damage was induced by the ion forms into visible pits. The response is single ion sensitive, one ion will create one pit. These pits are then often counted

using a microscope and automatic recognition software. By counting the number of pits, and making a fit to each of the tracks on the CR-39, the spectrum for each ion species and charge state can be extracted. An example of this process is shown in Fig.4.9(a). There are a number of major limiting factors of this detector type. First, the maximum cut-off energy is limited by the material thickness, while for heavy ions this is relatively high, typically hundreds of MeV, for protons this maximum cut-off is 11 MeV for a 1 mm piece of CR-39. Second, for very high ion densities pits can become overlapped, or so close they cannot be individually resolved. The result is that the total number of ions can easily be miscounted for high flux ion beams. Finally, the process of etching and scanning can be very time consuming and is not practical to implement on laser systems with repetition rates higher than the VULCAN laser system. Its mainly for this reason that other detection media have recently been implemented in the use of Thomson-Parabola spectrometers.

Image Plate is a proprietary particle detection media produced by FujiFilm. It is sensitive to all ionising radiation, including protons, electrons, x-rays and some circumstances ions. IP consists of a 10 μm protection layer, a 150 μm phosphor layer of composition $\mathrm{BaF}(\mathrm{Br}_{0.85}I_{0.15}) : Eu^{2+}$ and a steel support layer of 250 μm (all shown in Fig.4.9). An incoming particle of ionising radiation entering the image plate ionises the Eu^{2+} to Eu^{3+}, ejecting a photoelectron. The photoelectron is excited into the conduction band of the phosphor, where it is trapped in a lattice defect. This condition is metastable, with a lifetime of many hours. The exposed IP is taken to a scanner, where a tightly focused laser at 632 nm excites the metastable electron, which then decays from the metastable state to recombine with the Eu^{3+} ion, emitting a 400 nm photon in the process. The photon is detected with the use of a photomultiplier tube and the signal is amplified and converted to a digital image using an analogue to digital converter (ADC). The major advantage of this technique is that once all of the metastable electrons are depopulated (which, after scanning, is easy to do with a white light source) the same piece of film can be reused. The spatial resolution is typically, 25 μm and the dynamic range is over 5-orders of magnitude. However this may

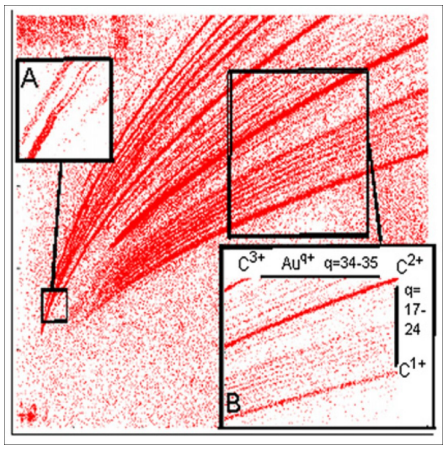

(a)

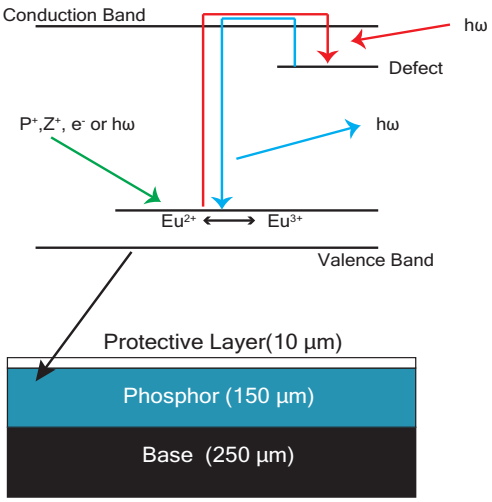

(b)

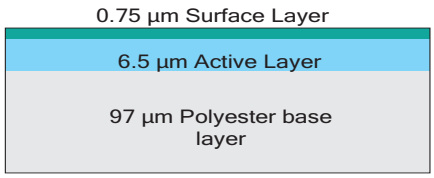

(c)

Figure 4.9: (a) Typical result when using CR-39 with TP-Spec, inset A shows saturation of the CR-39 and inset B shows individual tracks of Au and C ions resolved. (b) Composition of IP. Also shown is the level transitions which occur during exposure and scanning. (c) Composition of the HD-810 format of RCF used in the experiments presented in this thesis.

be extended by multiple scans of the same piece of IP (see Chapter 5).

In the context of using this type of film with the TP-Spec, a particular kind is used where there is no 10 μm plastic protection layer otherwise the lower energy ions would be stopped by this layer. Cross calibration of IP with CR-39 has been carried out by Doria *et al.* [77].

4.4.2 Kα X-ray Diagnostics

The measurement of x-ray emission from the target enables the fast electron beam temperature, divergence [13], conversion efficiency (see Chapter 6) and the level of refluxing within the target [78] to be inferred. This measurement of x-ray emission from laser solid interactions is typically done in two ways. Either imaging of the x-ray source at a particular wavelength for spatial resolution or dispersing spectrally the emission from the target. Two techniques are particularly relevant for the data presented in the following chapters namely: Kα imaging and spectroscopy.

As fast electrons generated by the interaction move through the target they collide and interact with K-shell electrons. These electrons are freed and L-shell electrons transition to the K-shell, emitting an x-ray photon in the process. The wavelength of this photon is dependent on the electronic structure of the particular material. The interaction of the free, fast electrons with the bound K-shell electrons has a cross-section which scales with electron energy. This cross-section peaks for electron energies in the tens of keV region. As such, this technique is dominated by the lower energy part of the electron spectrum.

Experimentally, copper and aluminium are typically used, emitting Kα photons at 8.047 keV and 1.486 keV respectively. In a target, for example plastic, a thin layer of Cu or Al is included to act as a fluorescent layer which enables a measurement of the fast electron population in that particular region of the target. The x-ray emission generated from this layer is then imaged by a spherically bent Bragg crystal which reflects and focuses the x-rays. An image is then formed on a detector which is usually IP or, occasionally, an x-ray sensitive CCD. By analysing this image, information about the fast electron beam divergence and spectrum can be experimentally derived. Alternatively, more detailed informa-

tion about the fast electron spectrum can be extracted, not solely by imaging but by spectrally dispersing the x-ray emission and looking at the emission and intensity of other spectral lines.

4.4.3 Plasma Diagnostics

The techniques mentioned in previous sections attempt to measure aspects of plasma emission, whether protons, electrons or high energy photons. In this section the use of techniques which, by external probing, measure the plasma electron density and the laser energy fraction not absorbed by the plasma will be discussed.

Optical Probe Interferometry

The critical importance of the electron density profile in intense laser-solid interactions has already been alluded to and will be detailed in later chapters. In order to characterise this density gradient the interferometry technique suggested by Benattar *et al.* [79] is often used. The common approach when this technique is used in laser-solid experiments is the following.

Initially a small "pick-off" of the main laser is taken and frequency doubled. Frequency doubling has two effects, first it enables probing of higher electron densities (see Chapter 2) and, second, it enables the scattered light from the interaction, with the central laser wavelength, to be blocked. This doubled light is then made linearly polarised with a polariser and transported into a so-called "timing slide" or delay stage. Where two mirrors are set at 90° to each other on a movable stage, allowing extra delay to be added to the optical path and changing the probe time relative to the arrival of the main pulse on target. After the delay stage, the probe is directed transversely past the target. In the overdense and solid regions the probe is reflected. In the vacuum regions the probe passes through unaffected. However, in the transparent, underdense region the probe passes through and is refracted. The refractive index decrease (as plasmas have a refractive index less than one) means that, in the plasma density gradient some parts of the beam accumulate less phase than others. The probe beam

is then imaged with a high resolution positive lens. As shown in Fig.4.10 the probe is directed into a Wollaston prism which acts to spatially separate the S- and P- components of the polarisation. Passing the beam through a second polariser which is set at a middle position (perhaps 45°) to the two orthogonally polarised components which leave the Wollaston means that two images of equal intensity and polarisation are produced. In the region where the two beams overlap, interference fringes are produced. Since, by using the Wollaston, the path length between the two images is identical, this is an inherently stable and easy to set up arrangement. The separation between fringes in the image plane of this interferometric arrangement is given by Benattar *et al.* as

$$i = (\lambda/\epsilon)(d_1/d_2) \tag{4.7}$$

where λ is the laser wavelength, ϵ is the divergence angle of the Wollaston, d_1 is the distance from the focus of the first lens to the Wollaston and d_2 is the distance from the Wollaston to the image plane. As explained previously, since the plasma density gradient can also be regarded as a refractive index gradient and, hence, an optical path length gradient, there is an observable fringe shift in the interference pattern in those regions of the probe beam which pass through the plasma. The electron density of the plasma can be calculated by using the Abel inversion technique to form a phase map and subsequently convert that phase map into a map of the electron density.

While this is a very successful technique, it does have a significant drawback when applied to laser-solid interactions. Since the densities involved are often very high, some parts of the probe beam are very highly refracted and are not imaged down the diagnostic line in those regions. Moreover, the main interaction typically takes place at the relativistically corrected critical density, many times greater than the critical density for the frequency doubled probe, and this would be the region of most interest to probe. As a result only regions of lower density can be probed. However, it is known [28] that the density profile at higher densities can be much different than in regions further out from the target. Techniques which resolve this issue are still the subject of research.

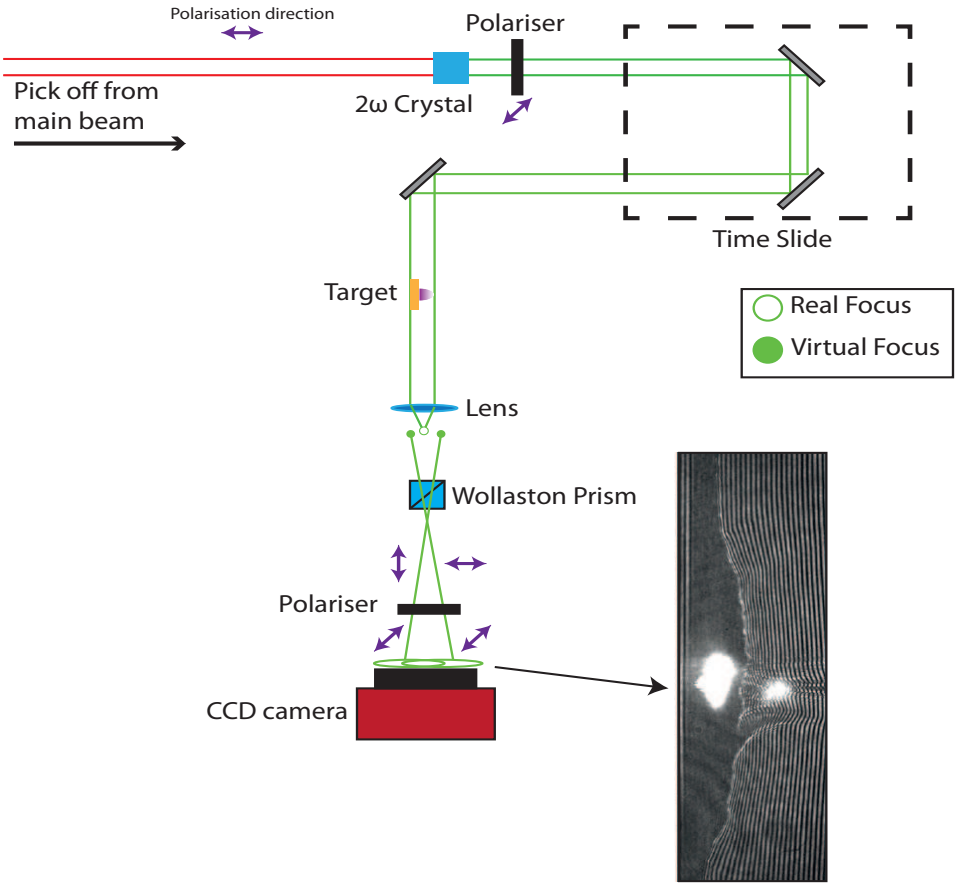

Figure 4.10: Layout of optical probe interferometer. Example image, with expanding plasma, shown in inset.

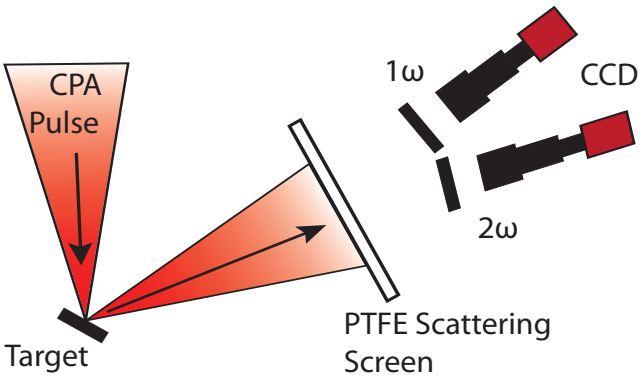

Figure 4.11: (a) Layout of plasma reflectivity diagnostic.

Plasma Reflectivity

Measurements of laser absorption in laser-solid interactions is critical in understanding the conversion efficiency of laser light to fast particles and the development of future applications for these interactions. Measurement of this is often done by imaging the specularly reflected light from the solid target. This is typically done using a scattering screen and a CCD camera with a telephoto lens filtered for the central laser wavelength, as shown in Fig.4.11. Additional filters and cameras can be used to look at higher, optical, harmonics of the laser wavelength. With proper calibration, the CCD camera is used to measure the energy reflected by the target. Alternatively an appropriately calibrated calorimeter can be used.

4.5 Simulation and modelling

Despite the range of diagnostic techniques which are implemented in order to gain useful experimental results, it is often the case that the number of variables are simply too large to gain a deep enough understanding of the fundamental physics without resorting to some type of supportive modelling. Analytical models, in their simplicity, can often be a great resource to provide such support. However, again it is often the case that the number of variables is simple too large to be accounted for by a simple mathematical model. Instead a broader understanding

can be gained by using numerical models which include a much larger number of physical effects and parameters. Obviously, it is not possible to perform such calculations in a pen-and-paper fashion.

Numerical simulations require an algorithm which includes both the relevant physics and a numerical scheme which is used to approximate solutions to the equations describing the system. The scale of the computing resources to carry out such an operation varies greatly depending on the task. For laser solid interactions certain models run in seconds on a desktop computer and others can take weeks on massively parallel high power computing clusters. This large range of scale and resource which can be implemented to solve a particular problem means that it is important to understand what physical phenomena are relevant and therefore what type of code to execute.

For laser-solid interactions there are three main types of code. In Gibbon's chapter [35] on the subject he helpfully sub-divides these in the way shown in Fig.4.12. For the type of laser-solid interactions that form the basis of this thesis the most useful codes are the kinetic and macroscopic (fluid) codes. The remaining code type, the so-called microscopic type, is particularly useful for simulations of particle stopping in matter (Monte-Carlo) or analysis of solid state or quantum effects (molecular dynamics).

Returning to the two most relevant code types (kinetic and macroscopic) the two subdivisions of these which are implemented in results section of this thesis, and are therefore the most relevant, are hydrodynamic (hydro) codes and particle-in-cell (PIC) codes. Other than being codes which model laser interactions with plasma the similarity essentially stops there. The next section will address some of the attributes of hydro codes, the circumstances in which they are often used and the hydro codes used in this thesis. Similarly, the section following on from that will discuss the same areas for PIC codes.

4.5.1 Hydrodynamic simulation codes

In general terms hydrodynamic codes treat the plasma as a fluid and calculate bulk quantities like density and velocity to describe the plasma dynamics. Micro-

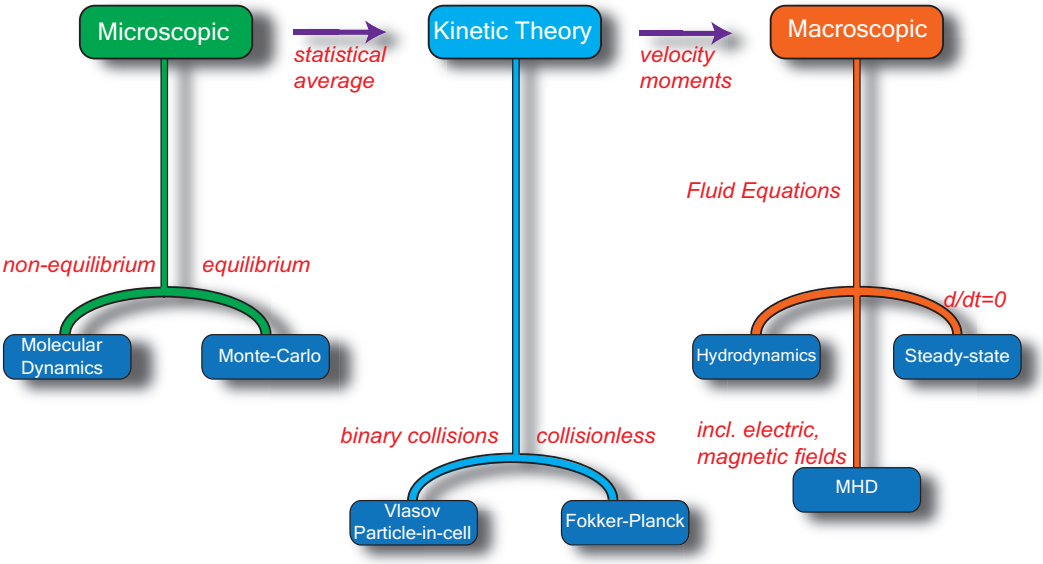

Figure 4.12: (a) Breakdown of various simulation code types for laser-solid interactions by the physics included in the model. From Gibbon [35].

scopic effects, like particle distributions are ignored. This fluid description is only valid if the system is very close to local thermodynamic equilibrium and typically holds when the time scale of the hydro motion is much longer than the electron-ion collision time. As such, in reality hydro codes are often used in circumstances where the effects of interest occur on time scales of hundreds of picoseconds or nanoseconds.

The method of solving the fluid equations in both space and time often works in following way. The mass density, velocity and internal energy of the system is mapped onto a spatial mesh or grid. The fluid equations are solved, which then enables the mesh to be evolved and the resulting energy transport to be calculated. Hydro codes often take one of two different forms based on how this mesh evolves. Either a Eulerian coordinate or a Lagrangian coordinate system is used. In the Eulerian form the grid positions are fixed and the fluid moves from one cell to another as it evolves. In the other, Lagrangian, type code the grid moves with the fluid and each point on the grid forms a so-called fluid element.

Other considerations for hydro codes include the absorption of the laser into the fluid and the material specific response of the fluid. For the absorption of the laser hydro codes typically do not include solvers for Maxwell's equations,

instead the laser is simply treated as energy input to the system, often assuming total absorption at the critical surface. The material specific response of the fluid is often included in hydro codes by using equation of state data tables, such as the SESAME [80] library, or by assuming an ideal gas equation of state.

For the work in this thesis two different hydro codes have been implemented, POLLUX [81] and HELIOS [82]. POLLUX is a 1D Eulerian type hydro code which assumes an ideal gas equation of state. The code also does not include any radiation effects such as the production of thermal x-rays. POLLUX was initially used in this thesis to model the expansion of plasma at the front of the target when it is irradiated by the laser ASE. Similarly HELIOS is also used to model these effects as well as a secondary nanosecond heating laser, in **chapter 6**. However, HELIOS - which is a Lagrangian type code - does include equation of state data and radiation effects.

4.5.2 Particle-in-cell Codes

PIC codes are a change of scale entirely from hydro codes. Besides the algorithm and physics included there is also a significant change in scale. Typical hydro simulations, and specifically those highlighted above, are able to easily complete on modern desktop computers within seconds. PIC simulations on the other hand often push the boundaries of what is possible in terms of high power computing. Most PIC codes are designed to implement the message passing interface (MPI) protocol, enabling the calculations required by the simulation to be divided among a large number of CPUs and computed in parallel, massively reducing the time required to complete a given simulation. The memory requirements for such simulations are also very large, reaching hundreds of gigabytes of RAM for a running simulation. In addition the storage requirements can be large, where each output is on the scale of gigabytes or tens of gigabytes. Such large amounts of output data also leads to the problem of effectively visualising it. To that end, it is often the case that custom visualisation software is written to run either on the normal cluster, a special multi-GPU node of the cluster or on a high performance desktop machine. Each of these technical points is a consequence of

the particle scale approach taken by PIC codes (i.e no longer using bulk quantities as in hydro codes).

Recall the reasoning behind the hydrodynamic representation of laser-plasma interactions, that it could be assumed that the system was in local thermodynamic equilibrium. In cases of short-pulse laser solid interactions however that assumption is no longer valid and therefore a so called kinetic treatment of the system is required. Ideally such a description of the plasma begins with a particle velocity distribution function of the form

$$\frac{\partial f}{\partial t} + \mathbf{v}.\frac{\partial f}{\partial x} + q\left(\mathbf{E} + \frac{\mathbf{v}}{c} \times \mathbf{B}\right).\frac{\partial f}{\partial \mathbf{p}} = 0 \tag{4.8}$$

The distribution function $f(r, v)$ is 6-dimensional - three spatial, three momentum - and is therefore complex to solve and memory intensive given that the computation requirements scale with the number of particles to the power of six. Reducing the number of dimensions is one possibility but another forms the basis of the PIC method. Instead of the distribution function consisting of real particle numbers it can instead be represented by discrete, statistically weighted *macroparticles*.

To calculate the position, current and density of the macroparticles they are mapped onto a grid. Once the current and density are known for a given position on the grid, Maxwell's equations can be solved to calculate the resulting electric and magnetic field. Using these fields the resulting motion due to the Lorentz force can be calculated. This results in a new current and density value which returns us the beginning of the loop. This loop is iterated for the duration of the simulation. A schematic of this algorithm is shown in Fig.4.13.

PIC simulations can give an important insight into the underlying physics of laser-plasma interactions. However there are a number of potential issue which can arise. For example the number of macroparticles per cell determines both how smooth the distribution function is in phase space and how much statistical noise is present in the simulation outputs. Depending on the particular problem being investigated this can be a determining factor in the result of the simulation, if for example the desired effect is hidden below the noise. In order to counteract

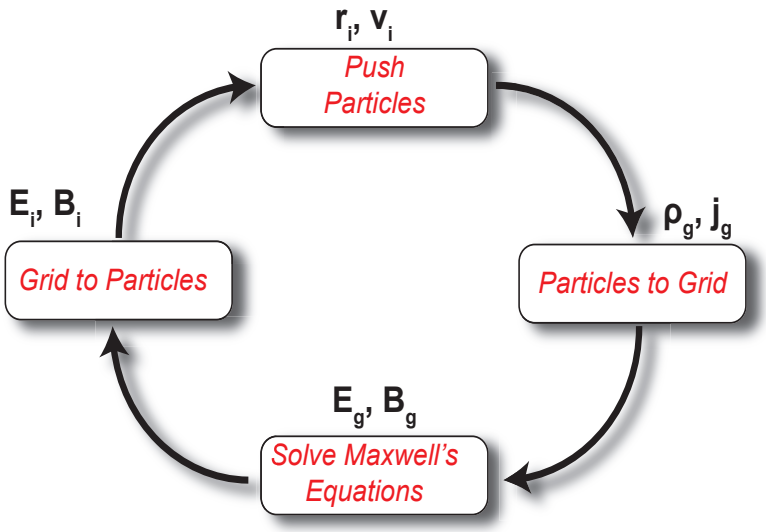

Figure 4.13: (a) The PIC algorithm where the subscripted "i" is the macroparticle index and the subscripted "g" is the grid cell index. The algorithm calculates the macroparticle density and current on the grid and then uses that to solve Maxwell's equations. The calculated electric and magnetic fields are then applied to the particles to determine their motion at which point the loop repeats

this one must often find a convergent condition where the measured effect does not change as more macroparticles per cell are added. Additional effects include spatio-temporal requirements to resolve the highest frequency in the system (the plasma frequency in the case of laser-solid interactions) and the length scales on the order of the Debye length. In both cases numerical instabilities can occur if these conditions are not met. In the latter, if the Debye length is not well resolved, the system will non-linearly self-heat until the condition is met, resulting in non-physical behaviour. Other drawbacks to PIC are the physical phenomena which are typically left out of the algorithm such as ionisation and collisions. This can lead to non-physical effects such as, in the case of collisions, unrealistic magnetic field growth since collisional dissipation of the field is not included.

For the work contained in this thesis, the PIC code implemented is called EPOCH. This code as suggested above uses the MPI protocol to perform parallel calculations. It distinguishes itself as being an intentionally open source code which, in principle, enables users to edit the code to make it better suited for specific tasks. In addition the code is developed with the end user in mind

and to that end it uses a simple input deck system where the parameters of the simulations can be easily modified. Besides these points EPOCH very much follows the PIC archetype.

4.6 Summary

In summary, conducting an experiment which investigates laser-solid interactions at the intensity scales relevant to the subject of this thesis requires the coming together of a number of key technologies from the laser, to target manufacture, to the implementation and design of various diagnostic techniques. Such is the complexity of each of these areas in themselves that significant effort must be expended in coordinating and planning before the experiment can even begin.

The interaction itself is also sufficiently complex that multiple diagnostic techniques must be deployed in order to build an understanding of the key effects occurring and in the process, hopefully, providing a glimpse of new and interesting physics. Additionally this is often not sufficient to gain a full understanding, significant effort also has to be put into modelling and simulations. A process which can often involve the use of a large amount of computing power and a significant amount of time. As we shall see in the following chapters, despite the large scale and complex systems which are implemented in such experiments, real and fundamental insights can be gained into the nature of high energy density processes.

Chapter 5

Surface transport of energetic electrons in intense picosecond laser-foil interactions

The controlled generation and transport of relativistic beams of electrons in solid density targets is critical for a number of applications in this field including the development of laser driven ion sources (e.g for cancer therapy) and the fast ignition approach to inertial confinement fusion. Both applications rely on efficient laser coupling into fast electrons and on controlling the spectral and spatial distribution of these electrons. Developing techniques which exert control over these properties of fast electron beams will therefore greatly enhance the prospects of future applications in this field.

Focusing on inertial confinement fusion for the moment. As discussed in previous chapters, a fuel pellet containing a mix of deuterium and tritium is uniformly, irradiated by nanosecond pulsed laser beams. In this approach the compression beams do the work of both increasing the fuel density and providing sufficient heating to initiate thermonuclear burn. This is often called the "central hotspot" approach. Since the conversion of laser energy into heating is very low a very large input energy (MJ) is required to achieve gain. Increasing the energy of the laser driver decreases the overall gain, and the effectiveness of this scheme.

Tabak *et al.* [5] proposed an alternative scheme called fast ignition in which

the compression and heating phases are separated, with "ignition" temperatures being reached through the use of the second beam. The benefit being that the compression driver energy can be reduced and by using an efficient heating source, the energy gain increased. This heating has to be done on the order of tens of picoseconds before the fuel disassembles. As a consequence a low input energy, high power source is required - naturally a high intensity short pulse laser is suited for this task. This approach proposes that the fuel should be compressed, avoiding as much as possible to form a central hot spot and then to fire a short pulse, high intensity ($\approx 10^{20}$ W/cm^2) laser into the expanding coronal plasma. The laser, being sufficiently intense will relativistically channel through the plasma and be absorbed at the relativistic critical density surface, generating fast electrons, which propagate into the compressed fuel, causing sufficient heating to initiate thermonuclear burn. If the short pulse beam heating can be achieved with a much lower energy than the reduction in the compression drive energy, the achievable gain in this scheme is predicted to be approximately an order of magnitude higher than the direct drive approach.

The critical issue with the fast ignition scheme however is the propagation of the laser in the tenuous coronal plasma and the fast electrons in the high density fuel pellet. The laser will filament and refract in the underdense region of the plasma, reducing the laser intensity and focal spot quality. The fast electron beam, generated by the laser, is not collimated (due to scattering in the laser field and the curved critical surface with which it interacts) and since there is a stand off distance between the electron source and the deposition region, the current density and, as a result the heating, will be much reduced. Finally, the electron beam does not travel through the high density plasma unperturbed. The electron beam is susceptible to plasma instabilities such as the Weibel and two-stream instability due to the formation of a cold return current, as described previously. All of these factors act to reduce the heating efficiency therefore increasing the required input energy of the heating beam and reducing the overall gain.

In an attempt to counteract this, Norreys *et al.* [14] introduced the concept of using a re-entrant cone inserted (see figure 1.3) into the D-T shell to move the

electron source closer to the deposition region therefore increasing the effective current density and reducing the impact of beam instabilities and issues with the laser propagation in the tenuous plasma. An increase in the fusion neutron yield of three orders of magnitude was measured compared to the case without a short pulse heating beam. Given that the effect of introducing a cone, although not without issues, is drastic - ideally attempts should be made to optimise this geometry.

In an attempt to do exactly this, 3-D PIC simulations by Sentoku *et al.* [83] demonstrated two effects. One, that the high intensity laser pulse is optically guided inside the conical target, focusing and consequently increasing the laser intensity at the cone tip by several orders of magnitude. Such an intensity increase is critical for improving the heating efficiency [15]. Second, in the laser interaction with the cone walls fast electrons are generated which in-turn self-generate a "quasi-static" magnetic and electric field at the target surface. This field acts to guide electrons along the cone walls and toward the cone tip resulting in an order of magnitude increase in the local electron density, as compared to a planar foil geometry.

This now returns us to the ideas of inducing changes in the fast electron generation introduced in **Chapter 3**. Recall, Nakamura *et al.* [62] explored this surface guiding effect further using numerical and analytical simulations. They predict that high energy electrons (MeV) accelerated into a planar target (in this case a target is taken as equivalent to the wall of the cone) can be decoupled from the bulk of the plasma and transported along the target surface due to the aforementioned formation of a strong surface field. Furthermore, Nakamura *et al.* show in simulations that this field has a strong dependence on the incidence angle of the laser, growing for angles increasingly close to the target surface. Finally, it was predicted that there exists a critical laser incidence angle above which the transmittance of electrons through the target falls to zero and all electrons are transported along the surface of the target.

In this chapter, results are presented from an experiment using the PHELIX laser at GSI, in Darmstadt, in which the surface guiding mechanism proposed by

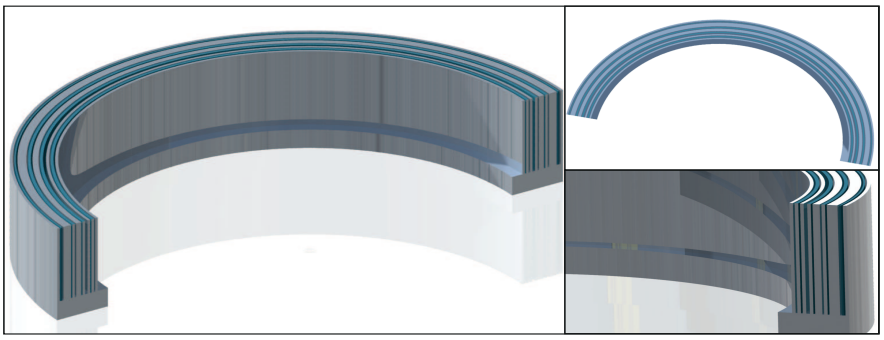

Figure 5.1: 3-D CAD drawing of "wrap around" stack diagnostic. Layers of IP are interspaced by increasing thicknesses of steel filtering to look at both the spatial and spectral angular distribution.

Nakamura *et al.* and others [60, 84] is explored. Specifically, the angular distribution of fast electrons escaping from the foil target is measured under conditions of varying laser incidence angle, polarisation and intensity, and compared to the predictions of Nakamura *et al.* and previous experimental results carried out at lower laser intensities [60, 84]. This study has been published in *Applied Physics Letters* [85].

5.1 Experimental Method

The PHELIX laser at GSI, as described in the previous chapter, is an Nd:Glass system operating at 1053 nm, capable of generating a 600 fs, 120 J laser pulse with $\approx$ 95 J on target in a 30 μm by 13 μm focal spot giving a peak on target laser intensity of 4x10^{19} W/cm^2. The energy within the focal spot (FWHM) was measured to be 50%. The intensity contrast, measured at the beginning of the experiment, was 10^6 up to 50 ps prior to the peak of the pulse. The targets used were 20 μm thick, 2x2 mm Cu foils.

In order to measure the angular distribution of escaping fast electrons a novel diagnostic technique was developed, henceforth known as the"wrap around stack" for reasons that will become apparent. Shown in Fig. 5.1, the wrap around stack consists of a curved back plate and base plate constructed from aluminium with a radius of 80 mm and covering an angle of $\approx 230^o$. Layers of image plate (IP), cut such that they match the arc length of the back plate, are inserted into this

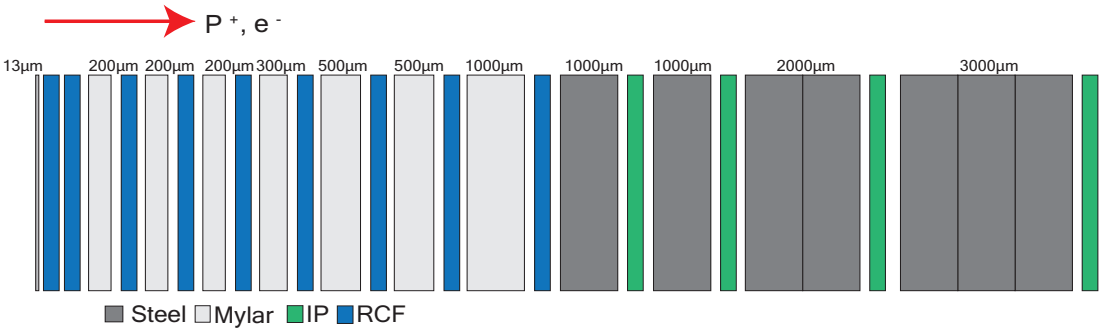

(a) Wrap around stack layers

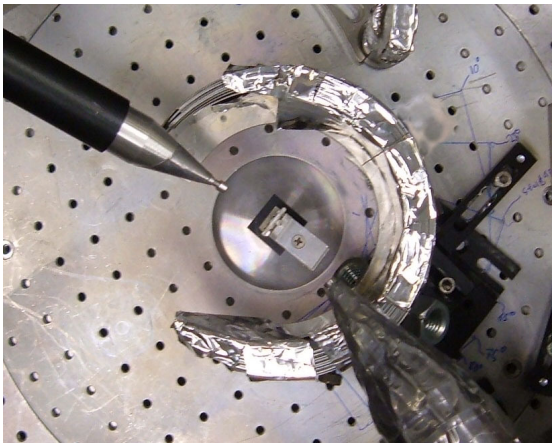

(b) Top view of wrap around stack diagnostic

Figure 5.2: (a) Stack design used to measure spectrum of protons and electrons. (b) Top view of experimental chamber, showing "wrap around stack" diagnostic covering 230^o degree angular range.

mount. In order to achieve some degree of spectral resolution four layers of IP are used interspaced, from the front to the back, with 1 mm, 1 mm, 2 mm and 3 mm thick steel filters respectively. These filters are mechanically cut and bent such that they also match the curve described by the back plate.

In addition to measuring the angular distribution of escaping electrons, the angular distribution of accelerated protons is also measured using a modification to the "RCF stack" diagnostic described in the previous chapter. Strips of RCF, cut to the same length as the IP, are placed at the front of the wrap around stack. Each layer is filtered with increasing thicknesses of Mylar to provide spectral resolution. Finally a thin layer of aluminium foil is placed at the very front of the stack in order to filter out heavy ions. The details of each layer are shown diagrammatically in Fig.5.2.

Whereas protons stop with a characteristic Bragg peak in the RCF stack,

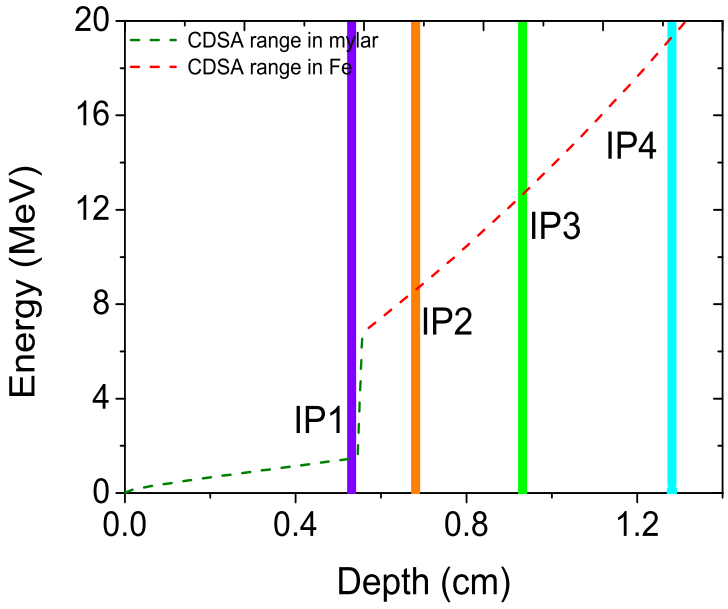

Figure 5.3: (a) Plot of the total path length of electrons in, initially, Mylar and then iron calculated using the continuous slowing down approximation (CDSA) range table from the ESTAR database. The positions of the layer of IP are also indicated, corresponding to minimum energy thresholds of (7 ± 1) MeV, (9 ± 1) MeV, (13± 3) MeV and (19 ± 3) MeV, respectively.

electrons stop in the IP stack by depositing energy across multiple layers. For this reason the achievable energy resolution is more limited than for the protons. However, it is possible to define each layer as an electron energy threshold whose signal is dominated by electron energies above a certain cut-off energy. In order to calculate the energy threshold that each layer corresponds to, the electron stopping database ESTAR[86] was used to compute the stopping of electrons in both the RCF front layer (assumed to be mostly Mylar) and the IP stack back layers (assumed to be mostly iron). Given the energy deposition characteristics of electron stopping in matter a minimum energy threshold is defined, corresponding to each layer, where an electron must be of a particular energy or greater to have deposited dose in that layer. This minimum energy threshold for each layer, from front to back, is found to be (7 ± 1) MeV, (9 ± 1) MeV, (13± 3) MeV and (19± 3) MeV, respectively.

In addition to the limited capability of this diagnostic to spectrally resolve the escaping electrons, the main focus is to enable a high resolution measurement of

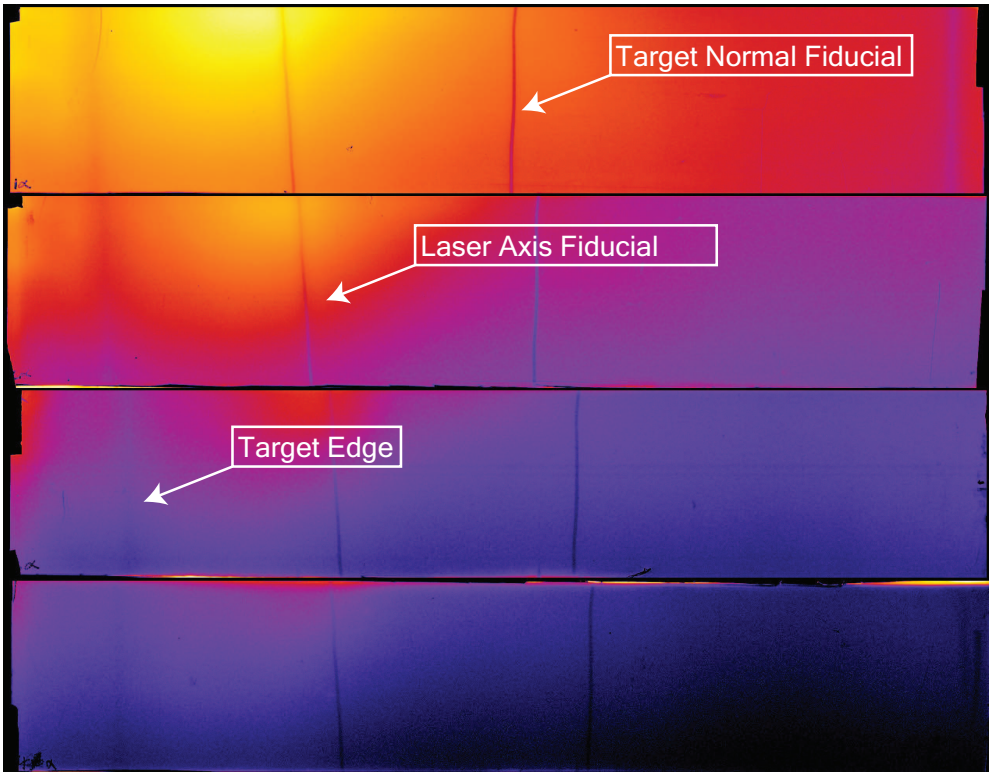

Figure 5.4: (a) Example image of unprocessed output from wrap around stack, wire fiducials are indicated by arrows in white. The stack shows the bottom half of the electron beam.

the angular distribution of these electrons. Once the wrap around stack has been exposed to the electron and proton beam, the image plate must first be scanned in order for the resulting data to be recorded.

The IP scanner is a flatbed scanner so the IP must be removed from the mount and laid flat. This produces a flat 2D image of the electron signal. An example of the raw form data is shown in Fig.5.4. Note the four layers are scanned simultaneously, avoiding issues with inadvertent signal loss between pieces of IP due to temperature variations or exposure to ambient light. Also note the obvious dips in signal, indicated by the arrows. These are intentional fiducials created by placing a wire consisting of Sn/Pb solder against the front of the stack, acting as an additional filter and causing a dip in the signal. These wires are positioned to mark the target normal and the laser axis directions. Alignment of the wires was aided by using reference laser lines set up and pointed along the laser axis and target normal directions.

In order that the distribution recorded on the IP can be extracted as a function

of angle a number of problems must first be resolved. Firstly, despite the level of filtering the signal recorded by the IP is often extremely high. So high, in fact, that the level of photostimulated luminescence released by the IP during scanning is enough to saturate the analogue-to-digital converter (ADC) in the scanner. By repeated scanning of the image plate the signal level can be decreased such that the ADC no longer saturates. However, in order to compare the signal level of one shot to the next the difference in scan time shot to shot must be corrected for. Second, an algorithm must be developed which removes the fiducials from the image, corrects for slightly different positions of the IP at increasing depths into the stack and makes an appropriate sampling of the data which is sufficiently insensitive to noise. Finally, using this line-out and the reference wires previously discussed, the angle for each point along the line out must be calculated.

Dealing with the issue of saturation first, multiple scans of the same IP are made. An identical region is sampled from an area of the image plate that is observed to be initially highly saturated. The mean signal of the sample region is then measured and plotted as a function of the number of times scanned. Finally an exponential fit of the form $y = Aexp(-x/B) + y_0$ is made to the data, where x is the number of scans, A and B are fitting parameters and y_0 is the value of y for the zeroth scan. In addition to exposure of the IP to the scanner light source, the IP is occasionally exposed to a white light source in order to decrease the time spent scanning. Whereas the exposure time of the scanner is very repeatable from shot to shot, the decay curve for manual exposure is subject to change as longer exposures are occasionally necessary. In the shots where this scanning procedure was applied the decay curve must be recalculated by measuring the decay of the unsaturated regions of the image.

Coming now to the second issue of dealing with the unprocessed IP data. The scanned image, such as that shown in Fig. 5.4, is manually split into four images each containing one layer of IP and read into a program written in the MATLAB technical computing language. MATLAB is used for this application, over python or C++ for example, due to a highly developed image processing toolbox and the relative speed at which new code can be debugged and implemented.

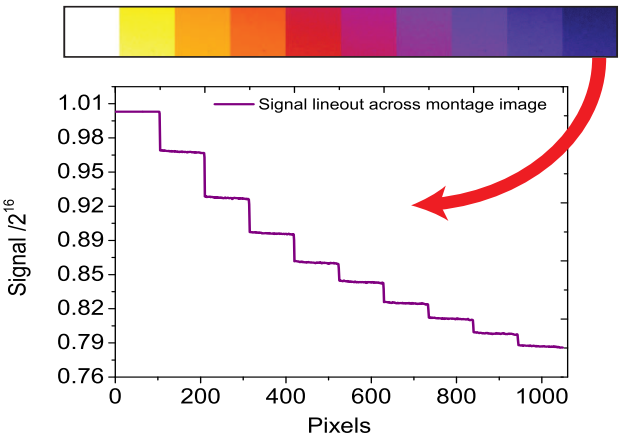

(a)

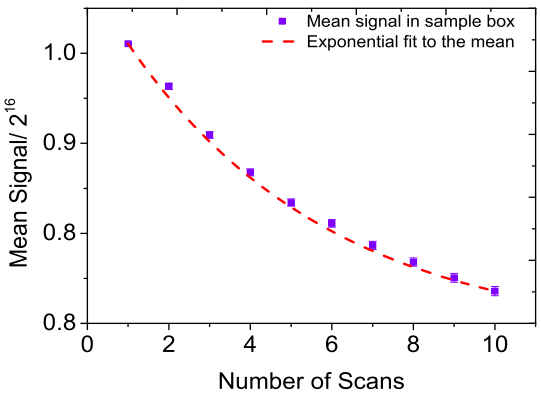

(b)

Figure 5.5: (a) Montage of the sample region used to measure the repeated scanning decay function. (b) Plot of the mean signal in sample area as a function of the number of scans. The red dashed line is an exponential fit of the form $y = Aexp(-x/B) + y_0$.

Due to the fact that each layer of the image plate is not orientated in exactly the same position, mostly as a result of the shifting caused by inserting the steel filters, each layer will cover slightly different angles. If the zero point for the angle calculation was taken to be the edge of the IP at one side then the relative position of features in each layer would be different, making it difficult to draw strong conclusions about the energy sensitivity of any features recorded. In order to correct for this a sub-function is included in the program that uses the fiducials as reference points and lines up the fiducials in each layer. Then using the layer with its fiducial closest to one edge as the standard, any excess angles are cropped from the other layers. The result is that some layers cover fewer angles but the angles which are covered can be compared from layer to layer.

Finally, a conversion from the current measurement of length into angle is required. First a line-out is taken across the IP and the signal averaged vertically down 500 pixels in order to mitigate hot spots and damage present on the IP. Using the pixel resolution of the IP to convert pixels into microns (25 μm/pixel) and the distance from TCC to each layer in the stack, the arc length and consequently the angle per pixel is calculated.

5.2 Experimental Results

Plotted in Fig. 5.6 (a-e) is the measured angular distribution of the escaped fast electrons for s-polarised laser incidence angles varying from 10^0 to 80^0. All laser incidence angles are measured relative to target normal. The direction of the laser, in red, and the target orientation in grey are also indicated on the plots.

Beginning with Fig. 5.6 (a), we note that the peak emission direction of the fast electrons is along the laser axis of propagation. This is unsurprising as we would expect the electron acceleration at the intensities present in this experiment to be dominated by the J×B force which is predominantly directed along the laser axis. As the incidence angle is increased however, an obvious change in the distribution is observed. The peak emission angle changes from being predominately aligned along the laser axis at 10^0 and 25^0 to a double peak

distribution at 45^0. With one obvious peak along the laser axis and another directed along the target surface. Moreover, as the incidence angle is increased further still to 65^0 and 80^0, this surface transported fraction of electrons now dominates the angular distribution of the escaping fast electrons.

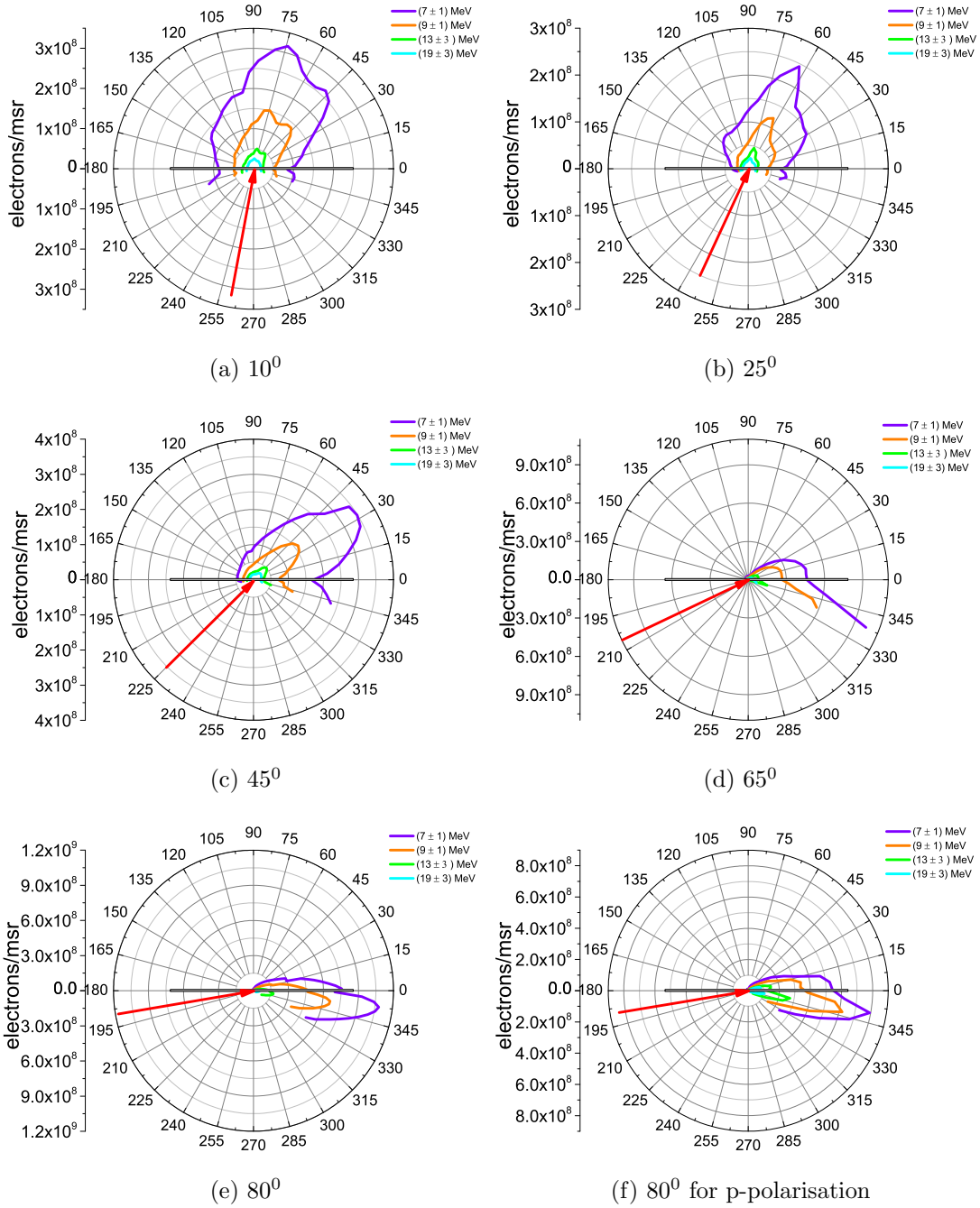

(a) 10^0 (b) 25^0

(c) 45^0 (d) 65^0

(e) 80^0 (f) 80^0 for p-polarisation

Figure 5.6: (a-e) Polar plots of the electron angular distribution as a function of laser incidence angle for s-polarisation. (f) Polar plot of electron angular distribution at 80° for p-polarisation.

This result agrees qualitatively rather well with the predictions of Nakamura *et al.* [62], who state that a critical angle exists at $\approx 65^0$, above which all of the fast electrons are pulled from the plasma by the formation of a strong surface-magnetic field which, although present for all incidence angles, is enhanced as more electrons are pulled onto the surface at increasing incidence angles. A "phase transition point" is reached above this critical angle where this surface magnetic field dominates and forces electrons into an "organised motion" along the target surface. Clearly, the results presented above, qualitatively agree with Nakamura *et al.* [62]. However note that, even at $\theta_l = 80^0$, there are still electrons transported through the target and detected at the rear surface.

Results from a previous experiment by Li *et al.* [60] supports this observation. Although using lower intensity ($\approx 10^{18}$ W/cm^2) and significantly lower energy pulses, similarly they observe a significant change in the angular distribution of the escaping fast electrons. Moreover, Li *et al.* [60] observe fast electrons escaping through the target rear surface, even above the critical angle suggested by Nakamura *et al.* [62].

In order to gain a quantitative measure of the growth of the surface current with respect of the rest of the signal and enable a comparison with the predictions of Nakamura *et al.* the ratio of the total number of electrons at angles on the front side of the target to the total number of electrons is made. This is shown in Fig.5.7(a). This plot shows, that although the number of electrons guided along the target surface grows significantly with laser incidence angle, it only ever makes up just over 50% of the total signal, in contradiction to the result of Nakamura *et al.*

An additional factor which must be considered is the change in laser intensity with incidence angle. As the laser incidence angle is increased, because the target surface is tilted relative to the laser propagation axis, the focal spot is effectively stretched along the horizontal axis thus decreasing the laser intensity at the interaction point. In order to investigate whether the observed change in the angular distribution of the escaping fast electrons is due to the change in intensity, shots at 25^0, 45^0 and 65^0 were taken with the laser energy reduced in each shot such

that the intensity was equal to shots taken at 80^0. An example of this data scan, at 45^0, is shown in Fig.5.7(b). While there is an obvious reduction in the total number of electrons as the laser energy is decreased, the electron angular distribution is still dominated by electrons transmitted through the bulk of the target, unlike in the 80^0 case, where the majority of escaping electrons are observed to be transported along the target surface.

The intensity dependence of the electron angular distribution has also been investigated by Habara *et al.* [61] at lower laser intensities (from 10^{17}-10^{19} W/cm^2). They find that as the intensity is increased the emission direction of the escaping electrons on both the front and rear surfaces moves closer to the target surface for a constant (60^0) angle. These changes are observed over two orders of magnitude in the laser intensity. The change in intensity during the experiment presented here is much smaller, less than an order of magnitude. As such it is the change in angle which dominates the growth in the surface magnetic field.

Another factor, highlighted by Habara *et al.*, is the extent to which the preplasma expansion at the target front surface (as controlled by the laser pulse intensity contrast) determines the magnitude of the surface magnetic field. Habara *et al.* observe, in PIC simulations, an increase in the surface directed current with the introduction of a small scale length preplasma on the target front surface. Increasing this scale length further causes the surface emission direction to move to the specular reflection direction. Increasing the intensity however (from 1x10^{18} W/cm^2 to 3x10^{18} W/cm^2), for this same scale length, to a level where the laser pulse power is greater than the critical power required for relativistic self-focusing causes self-focusing to occur to an estimated intensity of 10^{19} W/cm^2 and electrons are again guided along the target surface. The experimental results presented above are all at the same laser contrast and the laser intensity is always above 3x10^{18} W/cm^2. As such a sharp transition at lower intensities is not observed where the surface magnetic field is no longer strong enough to direct electrons along the target surface (such as the effect observed by Habara *et al* at 10^{17} W/cm^2). However, these previous results do highlight the importance of the laser intensity in the generation of the surface magnetic field.

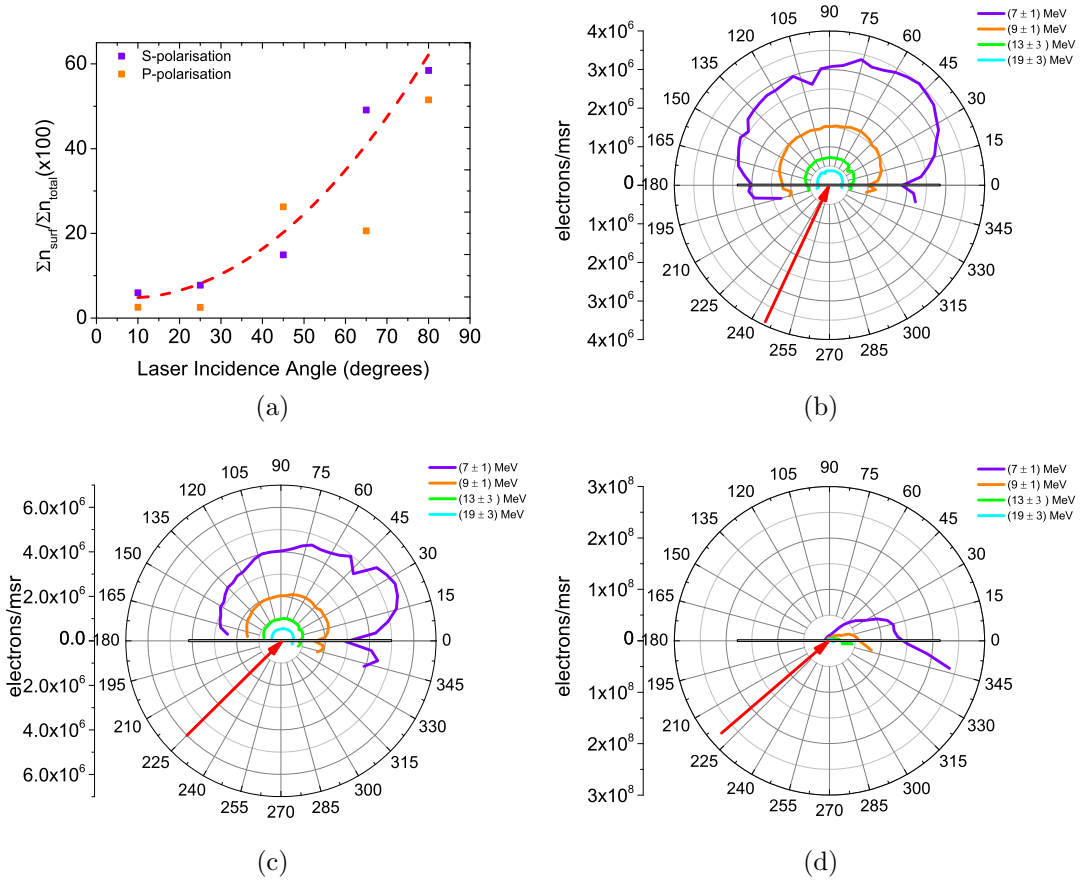

Figure 5.7: (a) Ratio of surface to transmitted current for s- and p-polarisation as a function of laser incidence angle. (b-d) Electron distribution at 25^0, 45^0 and 65^0 angle of incidence with a laser intensity equivalent to 80^0 angle of incidence.

The measured change in the angular distribution of the escaping electrons with incidence angle has been shown to be significant. In addition to measuring the escaping electrons, protons accelerated from the rear of the target via the TNSA mechanism were also measured. Whereas the peak electron signal clearly moves with incidence angle, no such movement is observed in the proton signal. As expected the measured proton signal is entirely dominated by protons accelerated in the target normal direction.

Considering, however, the decrease in the number of electrons leaving through the rear of the target, a significant decrease in the resulting electric field at the rear of the target would be expected. This would result in a significant decrease in the maximum energy of protons accelerated.

In order to explore this idea further the plasma expansion model of Mora

[21, 22] is used to model the expected proton cut-off energy. This 1D model assumes an isothermal expansion of a quasi-neutral sheath into vacuum. For this study, the decrease in intensity as a result of the increase in the size of the focal spot at larger angles is incorporated into the model.

Taking the experimentally measured pulse length, energy and focal spot (at 0^0) as inputs, the focal spot horizontal axis is scaled with incidence angle according to

$$r_x(\theta) = r_x(0)/cos(\theta) \tag{5.1}$$

where r_x is the radius of the major axis of the laser focal spot. The change in intensity can therefore be expressed as

$$I(\theta) = I(0)cos^2(\theta) \tag{5.2}$$

where $I(\theta)$ is the laser intensity for an angle θ and $I(0)$ is the laser intensity for $\theta = 0$. Using this calculated intensity for a given incidence angle the electron temperature is calculated according to the ponderomotive scaling with intensity [44].

$$k_B T_e = m_e c^2 \left(\sqrt{1 + \frac{a_0^2}{2}} - 1 \right) \tag{5.3}$$

where k_B is Boltzmann's constant, T_e is the fast electron temperature, a_0 is the dimensionless laser amplitude described in **Chapter 2**, m_e is the electron rest mass and c is the speed of light in vacuum.

The total number of electrons, N_e, accelerated by the laser is estimated by an energy balance with respect to the laser pulse energy

$$N_e = \frac{\eta E_L}{k_B T_e} \tag{5.4}$$

where η is the conversion efficiency of laser energy into fast electrons (assumed to be 20% in this model, based on measurements by Nilson *et al* with similar laser parameters [87]) and E_L is the laser energy on target.

The radius of this electron bunch at the rear surface can be written as

$$R_e = r_L + dtan(\theta_e) \tag{5.5}$$

where r_L is the radius of the laser focal spot, d is the target thickness and θ_e is the half-angle divergence of the electron beam. A half-angle of $\approx 25^0$ is assumed based on measurements made by Green *et al.* [13]. The resulting density of the electron bunch at the rear of the target is then assumed to be

$$n_{rear} = \frac{N_e}{c\tau_L \pi R_e^2} \tag{5.6}$$

where τ_L is the laser pulse duration. Using this calculated density the maximum energy of protons accelerated for a given rear surface electron density is related to the normalised acceleration time, t_p, of the protons which is given by

$$t_p = \frac{\omega_{pi} t_{acc}}{\sqrt{2e}} \tag{5.7}$$

where ω_{pi} is the ion plasma frequency, e is Euler's number and t_{acc} is the acceleration time of the protons. Fuchs *et al*[22], by experimentally measuring the proton maximum energy scaling with intensity and target thickness, find good agreement for a value of $t_{acc} = 1.3\tau_L$ for the proton acceleration time.

Finally, using the equations above, the maximum proton energy can be calculated using the formula of Mora [21].

$$E_{max}(\theta) = 2k_B T_e[ln(t_p + \sqrt{t_p^2 + 1})] \tag{5.8}$$

In Fig.5.8 the maximum proton energy is plotted as a function of laser incidence angle. The case where the laser intensity is changing with incidence angle is plotted for both the s-polarised and p-polarised scans. In addition, the case where the laser energy is adjusted such that the laser intensity remains constant as the incidence angle is changed is plotted. The above model is shown as the blue dashed line. A good agreement is found between the model and the experimental data.

This result suggests that despite the large observed changes in the escaped angular distribution of the fast electrons, the electrons which are electrostatically trapped inside the target, and to which the protons are sensitive, do not display such a change.

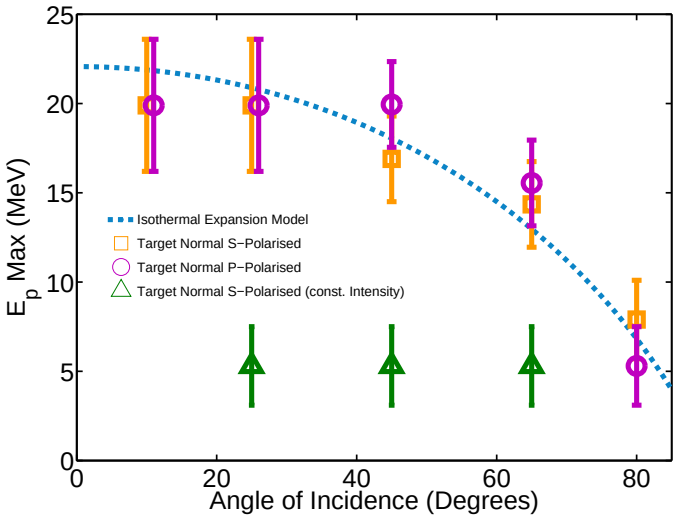

Figure 5.8: (a) Maximum proton energy as a function of laser incidence angle. The magenta and orange points show the measured maximum proton energy for p- and s-polarisation, respectively. The predictions of the model presented above are shown by the dashed blue curve. The points in green show the maximum proton energy for constant laser intensity.

5.3 Conclusions

In conclusion, it has been demonstrated that the angular distribution of escaping electrons is highly sensitive to the laser incidence angle. It has been shown that as the incidence angle is increased from a near normal 10^0 to a very steep 80^0 the escaping electron distribution changes from being peaked along the laser axis direction to being dominated by a population guided along the target surface. There is good qualitative agreement with previous work by other authors who, in PIC simulations, demonstrate that the growth of a self-generated quasi-static electric and magnetic field acts to confine and guide a population of electrons along the target surface and that this field grows with increasing laser incidence angle.

In contradiction to this previous work no "critical angle" is observed in which

the population of electrons escaping through the rear of the target falls to zero. Instead, even at 80^0 a fraction approaching 45% of the total measured escaping electron yield is observed to be transmitted. This lack of a critical angle could be a consequence of the assumptions made in the model of Nakamura *et al.* [62], such as an effectively infinite focal spot diameter, or in the PIC simulations where dissipative mechanisms for the magnetic field, such as collisions, are not included. As a consequence it is possible that the modelling overestimates the magnitude of the surface guiding fields.

An experimental consequence of increasing the laser incidence angle is to lengthen the laser focal spot along one axis, therefore decreasing the on-target intensity. It has been demonstrated that despite this change in intensity the factor which dominates the observed modifications to the angular distribution of escaping electrons is the increasing incidence angle. A simultaneous measurement of the maximum proton energy demonstrated, however, that despite the drastic changes in the electron angular distribution, the decrease in proton maximum energy can be explained simply by considering the corresponding decrease in laser intensity. In a further series of measurements, where the intensity is held constant, no such decrease is proton maximum energy is observed despite still observing modifications to the electron angular distribution.

With respect to the cone guided approach to the fast ignition and in particular those scenarios in which surface guided currents on the cone walls are used to enhance the electron density at the cone tip, these measurements demonstrate that while a fraction of electrons are surface guided a significant fraction is also transmitted through the target (or cone walls) regardless of laser incidence angle.

Chapter 6

Enhanced laser-to-electron energy coupling in solid density plasmas using a controlled plasma density gradient

One of the most complex aspects of laser-solid interactions is the coupling of laser energy into matter. There are a wide range of parameters which drive changes in absorption from laser intensity and electron density to laser polarisation and plasma temperature, which makes gaining a complete understanding difficult.

An understanding of absorption mechanisms, despite these difficulties, is however fundemental for both the understanding of laser-solid interactions in general and specifically for the previously discussed potential applications such as a laser-driven ion acceleration and laser-driven fusion schemes.

In this chapter, experimental results supported by both PIC and hydrodynamic simulations are discussed in which the effect of varying the front surface plasma density scale length on the absorption of laser energy into fast electrons is investigated.

6.1 Experimental Method

The experiment was performed using the VULCAN-PW laser which, during this experiment, generated a 0.7 ps, p-polarised, 1054 nm pulse with 130 J on-target energy - giving a peak intensity of $\approx 1.3 \text{x} 10^{20}$ W/cm^2 once optical throughput efficiencies are considered. The incident angle was 19^0 measured from target normal. At the beginning of the experiment the front end of the VULCAN-PW laser system was upgraded improving the intensity contrast to $< 10^{-10}$ at 1 ns and 10^{-8} at 100 picoseconds prior to the peak of the pulse [88], further details of the VULCAN-PW laser are given in **Chapter 4**. In addition to the improved inherent laser contrast, a plasma mirror system was installed during the experiment to improve the contrast still further. Up to two orders of magnitude improvement can be expected [72]. As such, it is reasonable to expect to be in a regime where only the rising edge of the main pulse preionises the target resulting in a very sharp initial plasma density profile.

In addition to the main short pulse laser a second 1054 nm laser of 5 ns in duration is used to preform a plasma on the front surface of the target prior to the arrival of the short pulse laser. The density profile of the plasma on the front surface is modified via changes in intensity of the long pulse beam (by changing the energy in the pulse) which causes a faster plasma expansion as the laser intensity is increased. In order to minimise the difficulties, particularly in simulations, of dealing with a spherical expansion a phase plate is used to produce a large focal spot, 270μm in diameter, with a flat top profile in order to approximate a one dimensional plasma expansion. A temporal delay between the pulses of 1.5 ns is used, measured with respect to the leading edge of the main pulse, with the long pulse arriving on target prior to the short pulse.

The target used for all of the measurements here consists of three layers of material. A 40 μm thick layer of aluminium, an 8 μm layer of Cu which acts as an x-ray fluorescent layer and 75 μm layer of plastic to act as a so-called "get-lost layer", mitigating the effects of the refulxing electron population. This target design, with a total thickness of 123 μm, is shown in Fig. 6.1.

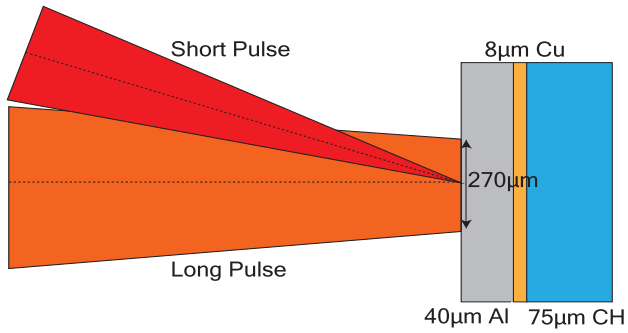

(a)

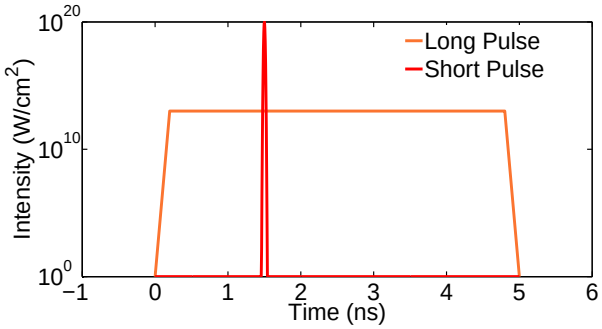

(b)

Figure 6.1: (a) Schematic showing the spatial overlap of the long and short pulse beams and the target composition (b) Temporal overlap of the long and short pulse.

In order to gain the fullest possible picture of the effect of changing the front surface plasma density gradient, a broad spectrum of diagnostic techniques are employed. Both a curved Bragg crystal, for 2-D imaging and a flat HOPG crystal spectrometer are used to measure x-ray emission from the burried copper fluorescent layer. Proton emission is measured using the RCF stack diagnostic discussed in previous chapters. In addition, the spatial-intensity profile of the specularly reflected laser light is measured using a CCD camera which is set to image a polytetrafluoroethylene (PTFE) scattering screen. The camera is filtered such that only a 20 nm window centered on the laser wavelength is observable. By comparing the signal recorded on each of these diagnostics, which are sensitive to different aspects of the laser to fast electron coupling, across various density profiles changes in the absorption are revealed. A schematic of the diagnostic arrangement is shown in Fig. 6.2.

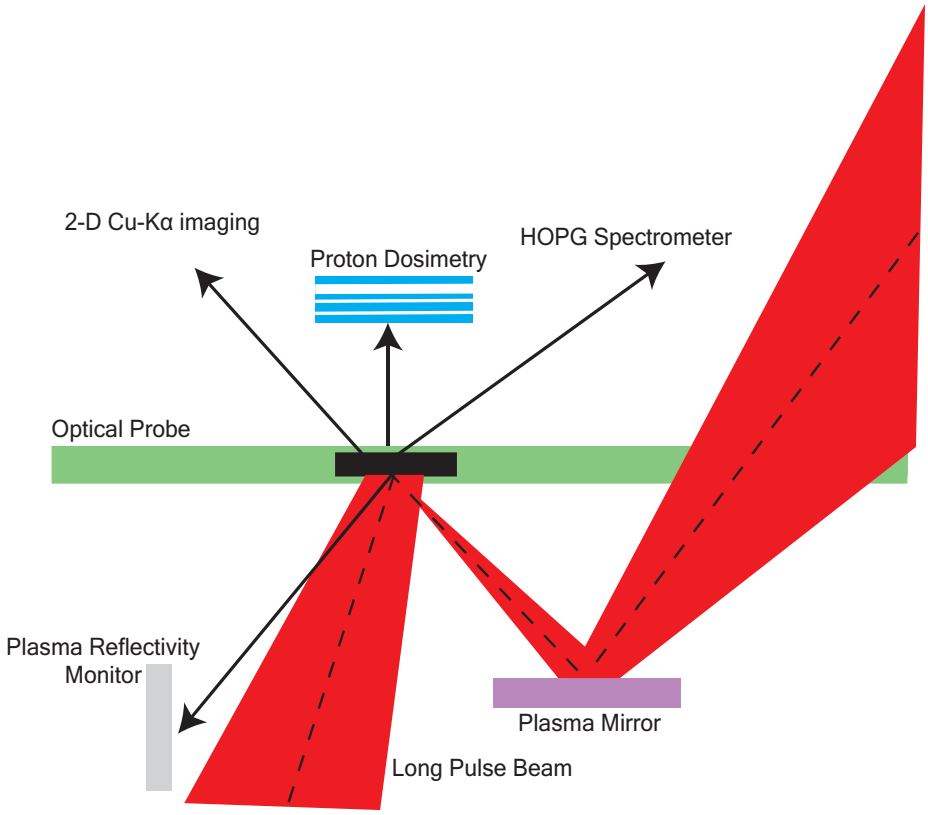

Figure 6.2: (a) Schematic showing suite of diagnostic techniques employed during the experiment.

6.2 Experimental Results

In order to understand the signal recorded by each of the diagnostics the interaction of the long pulse with the target must first be investigated. First, a calculation of long pulse intensity on target is required and second, using that calculated intensity, hydrodynamic simulations of the plasma expansion into vacuum are performed in order to evaluate the front surface density profile.

The intensity profile produced by the phase plate is shown in Fig.6.3. Of the bright central order and the second order on either side, only one of the larger spots interacts with the target. The other parts of the profile are allowed to miss

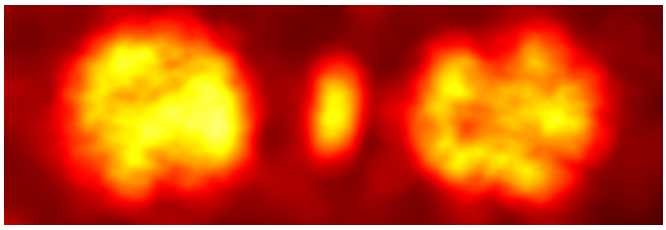

Figure 6.3: (a) Spatial profile of long pulse beam after passing through the phase plate. Only one of the large diameter spots interacts with the target.

the target altogether. Initially a phase plate was developed which produced a single circular distribution with the zero order in the middle. However, this lead to a very non-uniform expansion due to the intensity spike caused by the zero order. Using this three spot profile ensures that an approximately 1D expansion is driven by the large circular distribution.

The relative fraction of the total pulse energy contained in this circular distribution is measured using the image in Fig. 6.3. The total energy in the pulse is then measured by placing a large diameter calorimeter in the beam path. Using this energy value, the measured pulse length and focal spot diameter, the long pulse intensity is calculated. Shown in Table. 6.1 are the calculated long and short pulse intensities for each of the laser shots presented later in the chapter. Note that the long pulse intensity is varied over an order of magnitude where as the short pulse intensity is always within $\approx 9\%$ shot-to-shot variation. It is reasonable therefore to expect the changes in the long pulse intensity to be the dominant factor in any observed changes in the signals recorded on the diagnostics.

Shot	I_{LP} (TW/cm^2)	I_{SP} (10^{20} W/cm^2)
A	0	1.2
B	2.1	1.2
C	3.5	1.4
D	5.5	1.3
E	18.7	1.4
F	23.2	1.2

Table 6.1: Table of the long pulse, I_{LP}, and short pulse, I_{SP}, intensities used in data presented later in this chapter. The short pulse intensity is maintained within 9% of the mean whereas the long pulse intensity is scaled over an order of magnitude up to 23.2 TW/cm^2.

The key experimental results will now be discussed. In Fig. 6.4(a) the max-

imum proton energy is plotted as a function of long pulse intensity. In (b) the proton conversion efficiency is plotted. The points in blue are the data measured during this experimental campaign and in red are the results of a previous campaign with a more limited range of diagnostics and long pulse intensities [28]. The key difference between the two experiments, however, is the use of 40 μm Cu targets in the McKenna *et al.* [28] results compared to the 123 μm Al-Cu-CH layered targets presented here for the first time. As a result, the overall proton maximum energies and conversion efficiency in the present experiment is much reduced (such a scaling has been previously described [22]).

Focusing now on the new results. Note the increase in proton maximum energy from the zero point, in the absence of the long pulse beam, to I_{LP}=2.11 TW/cm^2, an overall increase of $(35 \pm 5)\%$. By increasing I_{LP} further the proton maximum energy decreases to below the proton energy recorded for I_{LP}=0 TW/cm^2. If the long pulse is increased even further the proton maximum energy is again observed to increase. Note also the good agreement between these most recent results and the previous results of McKenna *et al* [28]. Clearly there is a complex relationship between the density profile at the front surface of the target and the proton maximum energy. A similar trend is observed in the proton conversion efficiency, with both the initial peak and the second increase at the highest long pulse intensities seen in the proton maximum energies, reproduced in this measurement.

To gain a fuller picture of this interplay, additional results are shown in Fig.6.5(a)-(b). In Fig.6.5(a) the integrated Cu-Kα yield recorded by the HOPG spectrometer is plotted as a function I_{LP}, a near identical trend to both Fig6.4(a-b) is observed in this measurement. Finally in Fig.6.5(b), the integrated specular reflectivity is plotted. Here we see the opposite trend, where there are maxima in Fig.6.4(a-b) and Fig.6.5(a) there are minima in Fig.6.5(b), and visa versa.

By taking these four plots together a clearer picture emerges. Since the reflected energy measurement in Fig.6.5(b) provides a measure of the difference between the total laser energy and the absorbed energy then the minima in this plot corresponds to maxima in the laser coupling into the target. Comparing this to Fig.6.4(a-b) and Fig.6.5(a) then it can be concluded that the peaks here cor-

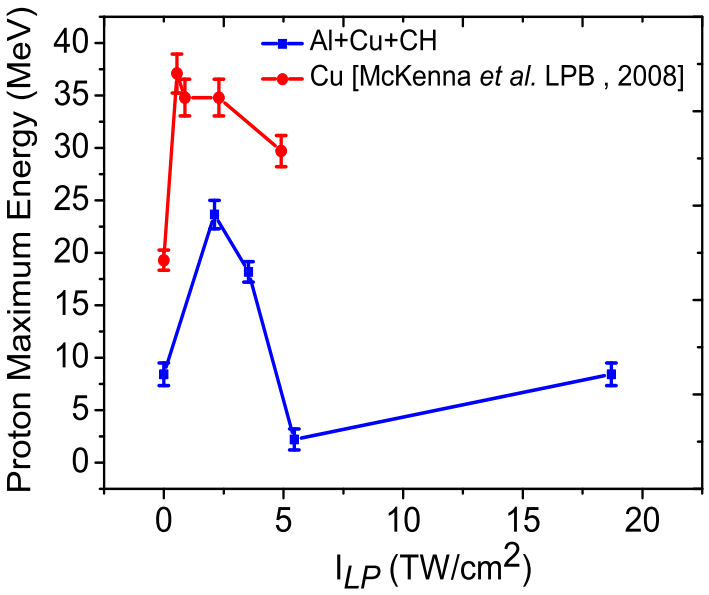

(a)

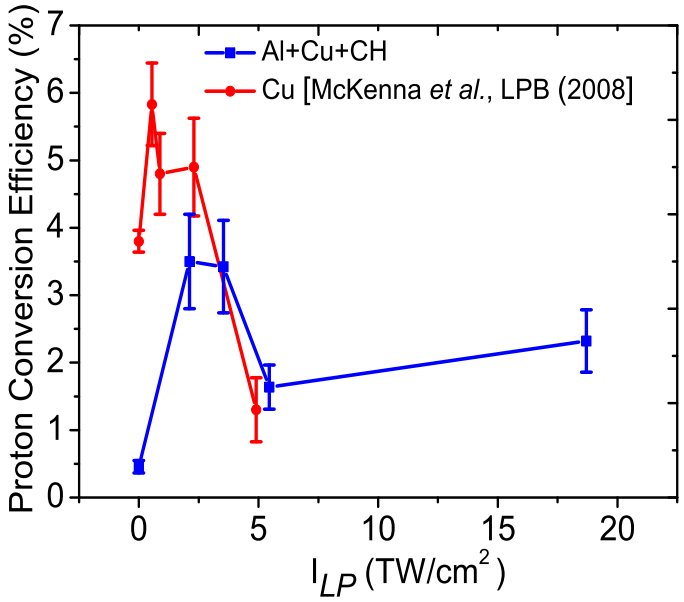

(b)

Figure 6.4: Experimental results of (a) proton maximum energy and (b) conversion efficiency

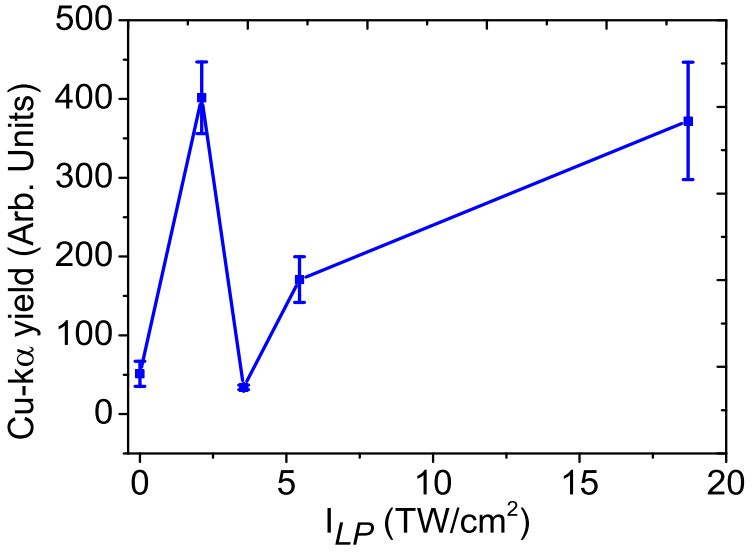

(a)

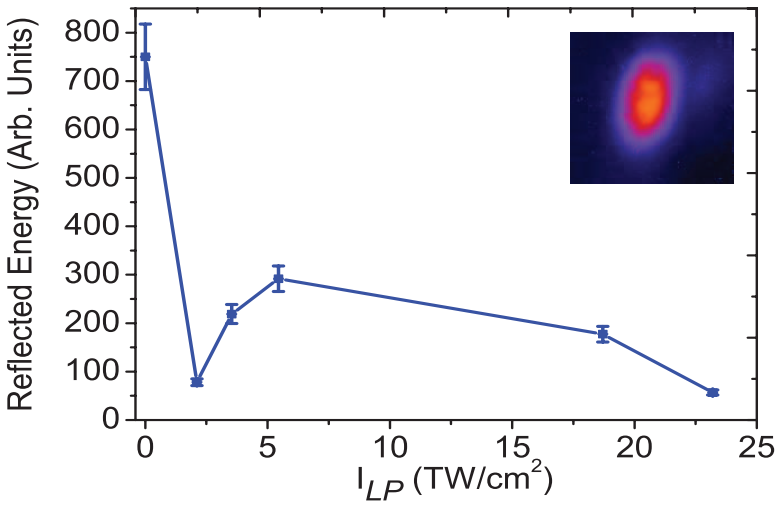

(b)

Figure 6.5: Experimental results of (a) x-ray yield and (b) plasma reflectivity plotted as a function of long pulse intensity.

respond to regions where the short pulse laser coupling into fast electrons, since these diagnostics are primarily sensitive to fast electrons, is optimised compared to I_{LP}=0 TW/cm^2. Moreover, there are clear signatures of two regimes, the first for low I_{LP} where the laser coupling to fast electrons is enhanced compared to the case where I_{LP}=0 TW/cm^2. Beyond this a transition occurs where the coupling is decreased. Finally as I_{LP} is increased further the coupling again improves.

Speculating, momentarily, on the source of this transition. For each of the shots presented the laser power is in excess of the critical power required for relativistic self-focusing (see **Chapter 2**), as such it is reasonable to expect the the laser to self-focus if presented with a medium in which to do so. Without the long pulse beam the laser contrast is effectively so high that the short pulse beam interacts with a near-solid density slab resulting in a poor energy coupling into fast electrons, likely via a vacuum-type absorption mechanism [35]. However, once the long pulse is present a region of preplasma exists in which the pulse self-focuses, resulting in an enhancement in the coupling efficiency [89]. As the I_{LP} is increased further and the pulse propagates through a larger region of underdense plasma it begins to filament resulting in a reduction in intensity and a laser-electron coupling as a result. Some evidence for this is presented in previous results of McKenna *et al.* in the same intensity range where reductions in coupling are observed here. Finally, as I_{LP} is increased further a new regime is entered in which the laser-electron coupling is dominated not by absorption at the critical surface but by absorption in the underdense part of the density profile, perhaps via the mechanism described by Lefebvre *et al.* [90]. To explore these ideas further we now model the density profile induced by the long pulse laser using hydrodynamic simulations and the laser coupling into fast electrons using PIC simulations.

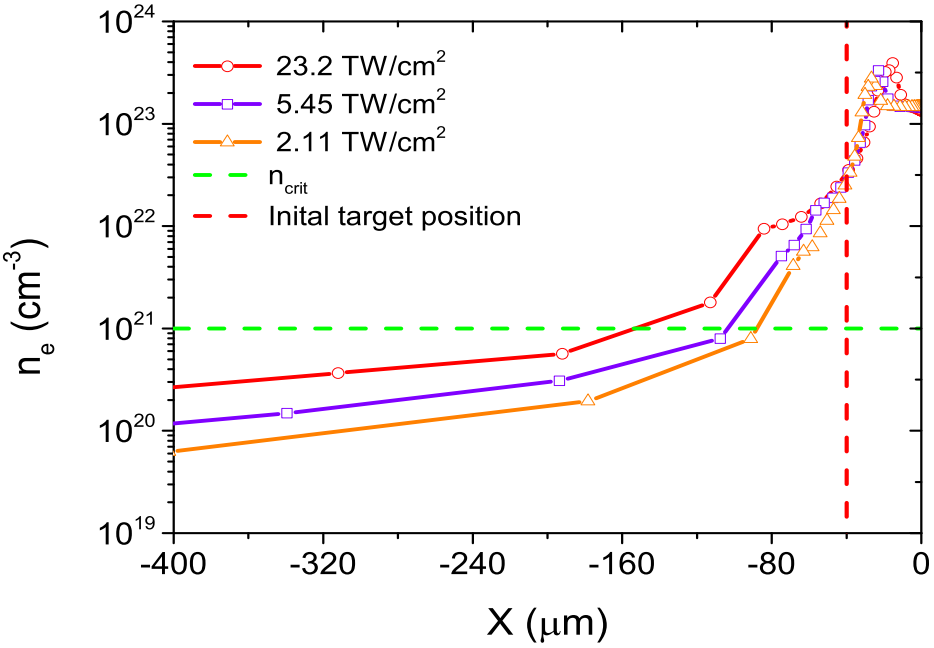

Figure 6.6: (a) Electron density profile extracted from HELIOS radiation-hydrodynamic simulations for three of the experimentally measured long pulse intensities in Table.6.1. The critical density is shown by the green dashed line.

6.3 Hydrodynamic and PIC simulations & discussion

In order to determine the plasma density profile which corresponds to these long pulse intensities, the plasma expansion at the front of the target is modelled using the 1D Lagrangian radiation-hydrodynamic simulation code HELIOS. Laser deposition is modelled using inverse bremsstrahlung when the electron density is less than the critical density and using a calculated absorption coefficient at the critical density surface. The material equation of state (EOS), in this case aluminium, is included from the PROPACEOS EOS and x-ray opacity data.

In Fig. 6.6(a) the density profile for three of the long pulse intensities listed above is plotted. The initial temperature of the target is assumed to be room temperature. The simulation is run for 5 ns but the profile is extracted at 1.5 ns, the time corresponding to the arrival of the short pulse laser on target. As

covered in **Chapter 2** by making a fit to the equation

$$n_e(x) = n_o exp(-x/L) \tag{6.1}$$

the density scale length is calculated by taking the negative inverse of the gradient of the fit. Note that there are two distinct scale lengths. The first, very close to solid densities and the second, at much lower densities. The reason for the formation of regions of different density scale lengths has been demonstrated by Kruer [91], among others, who describes the formation of these regions as a result of laser pressure at the critical surface. This light pressure pushes on the critical density surface (where the light is reflected) and slows the plasma expansion into vacuum. It has been shown, even for moderate intensities that this radiation pressure can significantly steepen the density profile in the higher density regions of the expanding plasma. The fitted equation, which unlike many previous studies in this area includes both density scale lengths, as the initial density profile input to the particle-in-cell code (EPOCH). The input density is cut-off for the EPOCH simulation at $5n_{crit}$. This cut-off which is ≈100 times less than solid density is imposed due to the large computational demand of the PIC simulation. However, given that the focus of this study is on changes in fast electron generation in the overdense plasma region caused by changes to the laser propagation in the underdense plasma, such a peak density is sufficient.

The simulation box contains 15000×3000 cells and is 147μm × 30μm in real space. A p-polarised laser of intensity 1.29×10^{20} W/cm^2 is used, corresponding to the average of the short pulse intensities shown in Table.6.1, and the pulse length is set as ≈700 fs.

By simply plotting, initially, some of the 2D outputs from the PIC simulations clear changes in the interaction for the various density scale lengths can already been seen. In Fig.6.8(a-d) the electron density is plotted for the three long density scale length cases and for a comparison sharp density scale length case. Plots of the laser electric field for the same cases are shown in Fig.6.7. Note also the difference in box size between case A and cases B,C,F. In the case of A where there is no large preplasma extending out into vacuum, the box size is cut down

in order to reduce the computational requirements.

Comparing initially the electric field, E_y, plots of cases A and B, the introduction of a large density scale length clearly makes a large difference to laser pulse propagation. In the first instance, with a very sharp density profile, the laser propagates through vacuum and interacts directly with the critical density surface. This interaction results in a deformation, by ponderomotive pressure, of the critical surface and a strong mirror like reflection of the incoming pulse. This can be seen in Fig.6.7(a), where the incoming pulse is modulated by the reflected pulse. At later times when the critical density surface is deformed further, the laser light is reflected over much larger angles due to an effect which is very similar to that highlighted by Schumacher *et al.* [92]. The deformed critical surface acts as a very short focal length parabolic mirror, resulting in a large increase in the divergence angle of the reflected light. However, in case B when the laser pulse has to propagate through a very large region of relatively high density preplasma a number of other effects can be observed. Initially after $\approx$50 μm of propagation there is a high degree of self focusing. After further propagation the pulse defocuses and then self focuses again. This self focusing continues up to the region approaching the critical density surface. At this point the laser begins to both diffract and refract in the density gradient. Some of these effects are also observed by looking at the two dimensional plots of the electron density, n_e. Specifically the self-focusing effect can be seen in Fig.6.8(b) but in addition there is an obvious ponderomotive channelling effect, where electrons are ejected from the laser axis by the transverse ponderomotive force enabling the pulse to propagate further into the plasma.

Moving on to cases C and F, the effect of the large region of preplasma now at even higher densities, following the HELIOS modelling, begins to have a detrimental impact on the laser pulse propagation. In case C looking at both n_e and E_y, similar to B the pulse self-focuses but after a certain a propagation length this strong filamentation of the laser pulse occurs and the various filaments begin to refract in the plasma density gradient. This spreads the laser energy over a significantly larger region than the initial laser focal spot. Analysis of E_y over

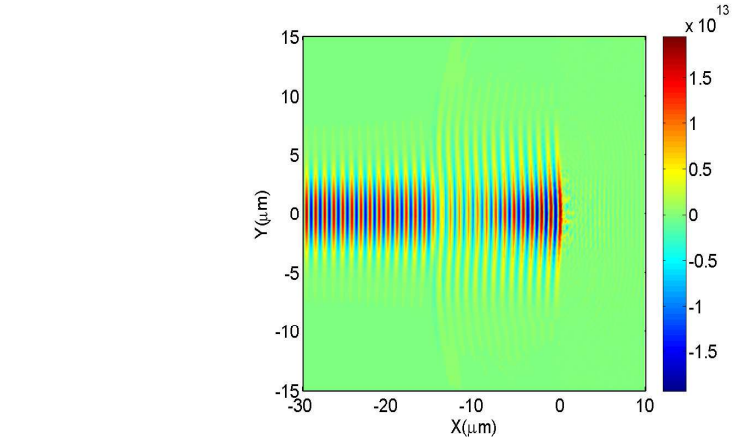

(a) Case A - sharp profile

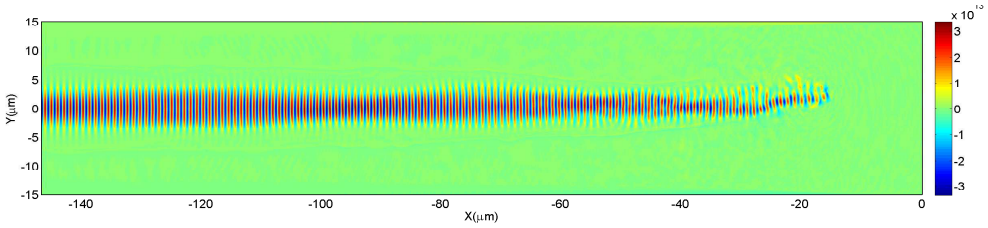

(b) Case B - profile for $I_{LP} = 2.11$ TW/cm^2

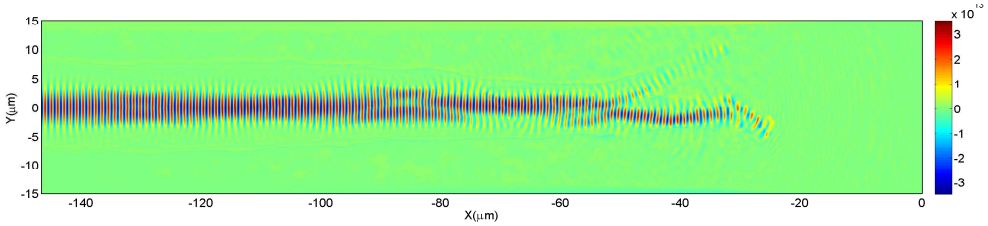

(c) Case C - profile for $I_{LP} = 5.45$ TW/cm^2

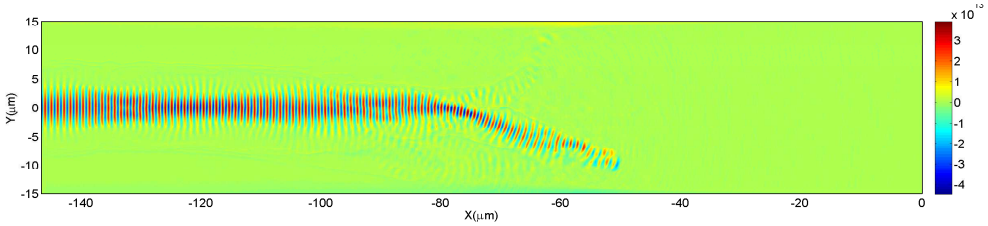

(d) Case F - profile for $I_{LP} = 23.2$ TW/cm^2

Figure 6.7: Electric field plots from EPOCH PIC simulations of density profiles for cases A, B, C and F from Table.6.1.

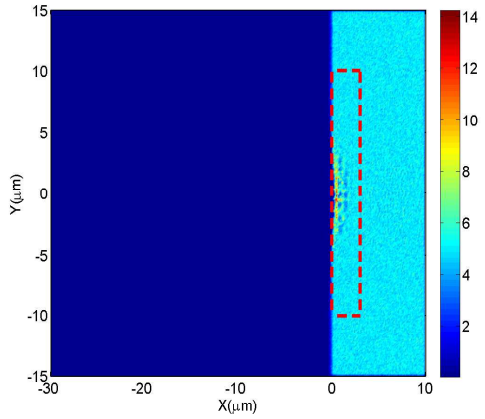

(a) Case A - sharp profile n_e/n_{crit}

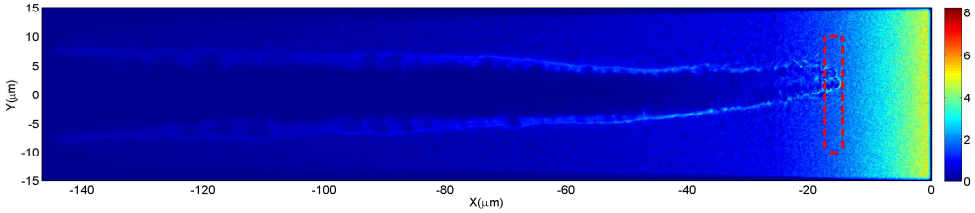

(b) Case B - n_e/n_{crit} profile for $I_{LP} = 2.11$ TW/cm^2

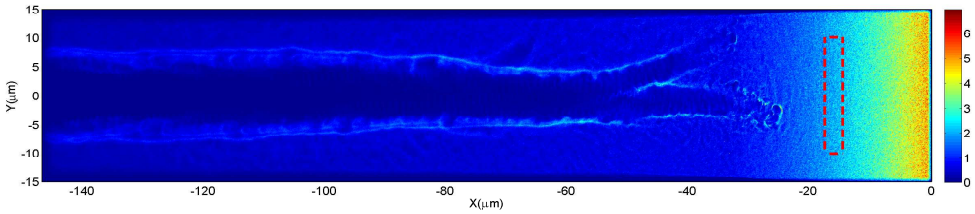

(c) Case C - n_e/n_{crit} profile for $I_{LP} = 5.45$ TW/cm^2

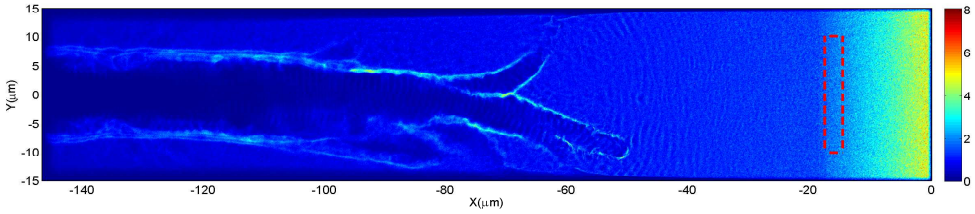

(d) Case F - n_e/n_{crit} profile for $I_{LP} = 23.2$ TW/cm^2

Figure 6.8: Electron density plots from EPOCH PIC simulations of density profiles for cases A, B, C and F from Table.6.1. The rapid onset of laser filamentation can clearly be seen for longer density scale lengths.

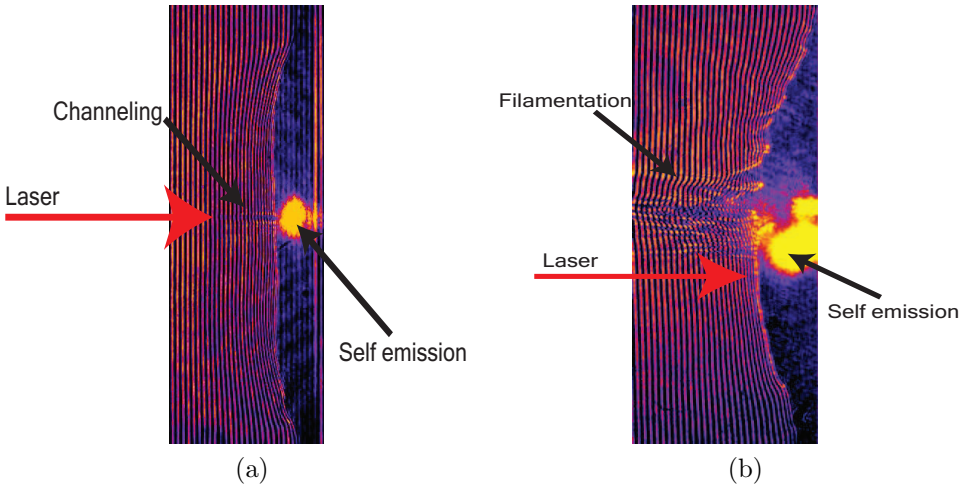

Figure 6.9: Transverse optical probe interferometry images under very similar conditions from the previous McKenna *et al.* [28] study (a) Showing channel formation (b) Showing the onset of beam filamentation.

several time steps shows that the onset of this filamentation is seeded by the onset of diffraction of the laser pulse following a region of strong self focusing. In case B self focusing is observed to occur shortly after the pulse enters the simulation and again close to the critical density surface. In C the self focusing is significantly stronger than in B, leading to a rapid diffraction of the pulse. These diffracted regions are however still intense enough to channel into the plasma resulting in a break up of the laser spatial profile. In F, at even longer plasma density scale lengths, the onset of filamentation appears even earlier in the simulation and is more severe, owing to the combined effects of self-focusing, diffraction and refraction. Some experimental support for this effect also exists. In the previous study by McKenna *et al.* [28], highlighted earlier in Fig.6.4, results from transverse optical interferometry show clearly filamentation of the incoming laser pulse for long pulse intensities very similar to those which are used here as an input to HELIOS and EPOCH, also showing filamentation. Below this intensity, when the density profile is steeper, filamentation in the optical probe is not observed. An example of this measurement is shown in Fig.6.9 for the cases where there is (a) channelling and (b) filamentation.

Taking this analysis of the simulation results a step further it is useful to examine the electron spectrum in the region of the critical density surface. The

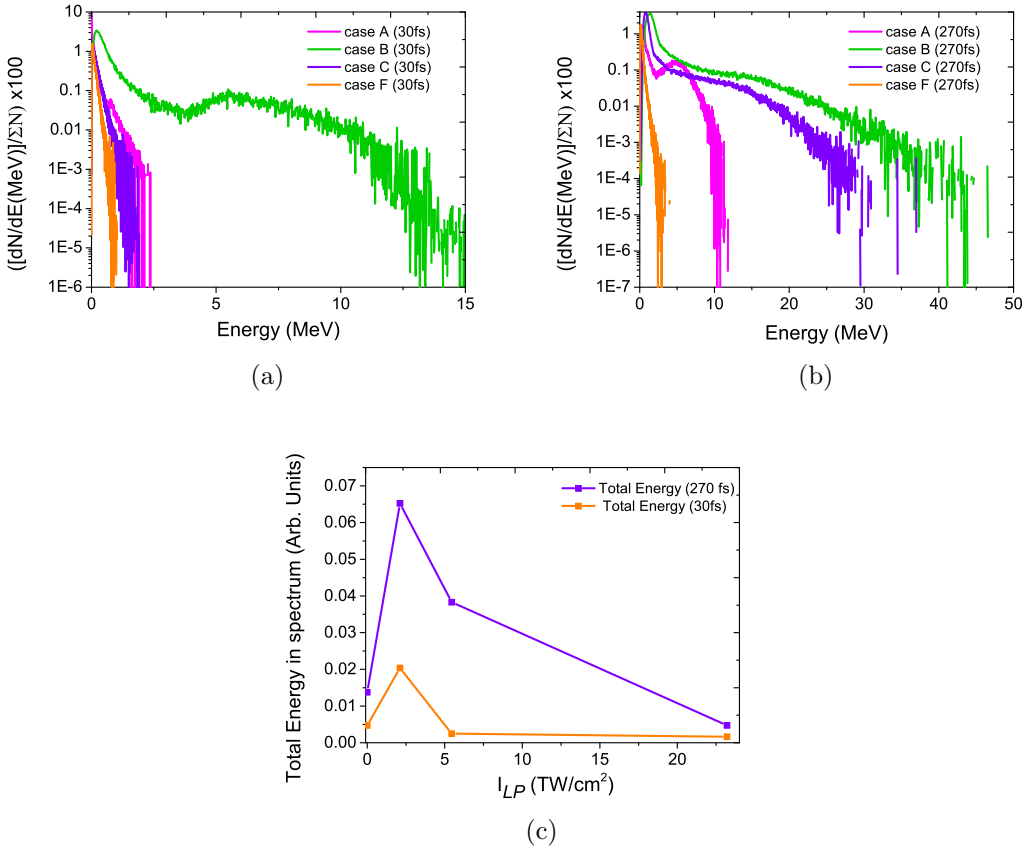

Figure 6.10: (a) Electron spectrum at 30 fs after laser pulse has crossed into overcritical region for (b) Electron spectrum at 270 fs after laser pulse has crossed into overcritical region (c) Total energy in spectra as a function of the experimental long pulse intensity.

sample region is highlighted by the red box with the dashed outline. The sample is centered on the laser propagation axis but intentionally limited to less than the entire vertical extent of the simulation in order to avoid the influence of any edge effects at the extremes of the simulation box.

In Fig.6.10(a) the electron spectrum in the sample region is shown for cases A, B, C and F after only 30 fs of heating. The spectrum for the sharp profile case clearly cuts off at a lower electron energy than case B. The other cases, C and F, also cut off a significantly lower electron energies than in B. Integrating under these spectra and accounting for differences in total numbers of electrons in the sample region an estimation of the laser-electron conversion efficiency can be made. This is plotted in Fig.6.10(b). Clearly for case B there is very rapid and significant generation of fast electrons at early times. The form of the curve

agrees well with that of the experimental data, an optimum in conversion efficiency is seen for the density profile corresponding to the long pulse intensity in case B. However, a second increase for very long density scale lengths, such as in the case of F, is not observed. Making the same measurement at 270 fs, while case B still has the largest cut-off energy and total energy contained in the spectrum, the other cases are becoming more comparable. This suggests that the optimised condition measured experimentally is in fact a dynamic effect which is most effective at the very beginning of the interaction at the critical surface.

So far good agreement between the trends measured experimentally and in simulations has been established. However an underlying reason for such increases have not yet been explored. In the first instance the differences between case A and B can be understood by considering the magnitude of the laser electric field interacting with the critical density surface. In the same sample region as before the laser electric field is measured for case A and B. This is plotted in Fig.6.11(a). It is clear from this measurement that the laser field in case B has increased significantly in magnitude compared to the case where the laser pulse does not propagate through plasma. This is due to the strong self focusing occurring near the critical surface region of the target. Following the measurements of Ping *et al.*[58] and the subsequent empirical model by Davies [89] this self-focusing induced intensity increase drives a hotter population of fast electrons and an overall higher absorption, resulting in the spectrum in Fig.6.10(a). This process is however dynamic. The same measurement is performed at 270 fs in Fig.6.11, while case B is still at a higher laser intensity than A, the difference is reduced. These changes appear to be a consequence of the laser pulse ponderomotively channelling into interaction region. As electrons are pushed transversely away from the laser axis, the self focusing effect is reduced which results in more comparable laser intensities between the sharp density scale length case and case B. This effect has also to be considered in the context of the Gaussian temporal profile of the incoming laser pulse, hence the overall higher electric field values at later time steps. It is likely that this process is responsible for the unexpectedly high energy electron spectra at early times for case B and then the more

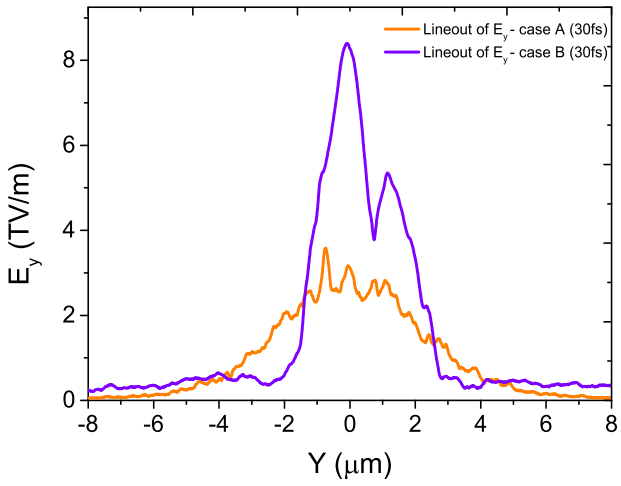

(a)

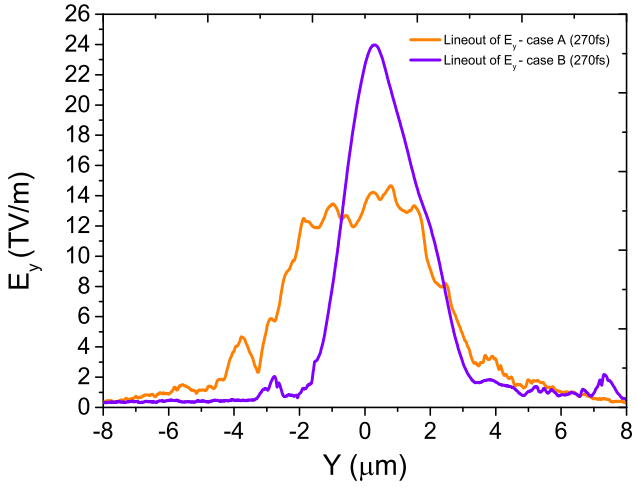

(b)

Figure 6.11: (a) Line-out of the laser electric field in the same region as the spectra is sampled. The line-out is taken at 30 fs for both case A and case B. (b) The same measurement made at 270 fs

closely matched spectra at later times. One can imagine that the efficacy of this dynamic effect could be enhanced if the period of self focusing coincided with the peak of the pulse. Two ways this could be achieved would be to use a plasma shutter like technique [69] to remove the rising edge of the pulse, or simply to use a femtosecond scale laser pulse. This would give the electrons less time to move transversely before the peak of the pulse arrived.

Good agreement has been demonstrated for the optimum condition measured experimentally and the subsequent decrease in proton energies, conversion efficiency and x-ray yield measured at longer density scale lengths. However, the gradual increase measured at the longest scale lengths is not observed in simulations. The good agreement between the four separate experimental measurements does strongly suggest that this increase at longer scale lengths is a real effect. Indeed, modelling and simulations by Lefebvre *et al.* [90] and later by Andreev [63] also suggest a global increase in laser-electron conversion efficiency with density scale length. There are a number of possibilities why such an effect is not observed in simulations. One is that the increase is attributable to a volume type heating mechanism mediated by a standing wave which forms between the incoming and reflected laser pulse, as suggested by Lefebvre *et al.*. The simulations above are already extremely computationally expensive (typically 1.3×10^4 core hours per simulation). Allowing these simulations to run for the length of time required to form a standing wave in the underdense region and then providing enough time for the resulting accelerated electrons to be injected into the overcritical region would require significantly longer runs. Such simulations are not impossible, but would require a dedicated program of work beyond the scope and the scale of this study. Another possibility is that of the transverse scale of the simulation box. At 30 μm it is significantly smaller than the 270 μm long pulse driver which forms the plasma in the first place. As a consequence at the longest density scale lengths the diffraction and refraction of the pulse in the plasma is so large that, at late times, the pulse is essentially directed out beyond the transverse limits of the simulation. Ideally this effect could be corrected by running simulations with larger lateral dimensions, however as already stated the simulations above

are already nearing the limit of what is possible computationally without scaling up to a very large high performance cluster.

6.4 Conclusion

In conclusion, the effect of preplasma density scale length has been investigated both experimentally and via simulations. A long pulse, nanosecond scale, laser is used to drive a quasi-1D plasma expansion into vacuum prior to the arrival of a high intensity (10^{20} W/cm^2) short pulse laser. Experimentally an optimised proton maximum energy, conversion efficiency and x-ray yield is measured with introduction of a density profile at the front surface of the target corresponding to a long pulse intensity of 2.11 TW/cm^2. Measurements of the plasma reflectivity are in good agreement, suggesting that this change is driven by an increase in the short pulse absorption. The density profile corresponding to a given long pulse intensity is modelled using the radiation-hydrodynamic simulation code HELIOS. These profiles are then used as an input to the PIC simulation code EPOCH. The simulation is scaled to the largest size and densities computationally possible, using the resources available to our research group, in order to investigate the changing physical processes arising in the transition from a large region of underdense plasma to a region of overdense plasma. Good agreement with the experimental results is found. An optimum density profile condition is obtained at the same point in the simulations as in the experiment. The driving mechanism behind this increase is proposed to be the strong self-focusing which occurs near the critical density surface when a density gradient is present. This self-focusing drives the laser to higher intensities, causing a hotter, higher energy electron spectrum than might otherwise be expected. This process is shown however to be dynamic and, at later times when the electrons which induce the self-focusing are swept away from the laser axis the laser intensity between profiles is increasingly comparable. At longer density scale lengths there is an experimentally measured decrease in absorption. In simulations, and in agreement with measurements from a previous study, this decrease corresponds to beam break up as a result of

diffraction in the plasma induced by self-focusing. There is potential to optimise this effect further by arranging the interaction conditions such that the switch on of the self focusing effect coincides with the peak of the pulse. Two possible routes to this would be to either specifically shape a the temporal profile of the rising edge of a pulse or by using femtosecond scale pulses.

Chapter 7

Laser absorption to fast electrons in the transition to the relativistic induced transparency regime

In the previous two chapters the interaction of intense laser pulses with micron-scale, solid density targets was discussed. In such interactions, the laser pulse propagates up to the relativistically corrected critical density surface and whatever energy is not absorbed is reflected. As has been shown, this incoming laser-field is depleted due to the generation of high energy electrons which oscillate in the laser field and carry away energy from the laser pulse. The generation and transport of these electrons, whether generated at the critical surface or in the preplasma or transported through the bulk of the target or along the surface, has until now been the focus of the discussion.

In this chapter the discussion shall move on somewhat to consider the effect of limiting the target thickness to nanometer scales and shortening the pulse duration from the hundreds of femtoseconds previously considered to tens of femtoseconds.

The interest in interactions with such "ultra-thin" targets has been motivated in large part by attempts to develop laser driven ion sources. Specifically, for the

TNSA mechanism of ion acceleration which relies on a high electron density at the rear surface of the target to generate a high accelerating field, a thin target means that the rear surface is closer to the interaction region. Given that the electron source developed at the critical density surface is highly divergent, this reduction in transport distance to the rear surface of the target therefore results in a higher electron density at that point as compared to thicker targets. Studies in recent years have demonstrated a clear increase in the cut-off energy of protons with decreasing target thickness as a consequence of enhanced electron density at the target rear, for purely geometrical reasons, and for reasons of decreased electron refluxing time [93, 94]. However, it is noted that once the target thickness is decreased to thicknesses of 100 nm or less, and these geometrical considerations become less important, the proton maximum energy is observed to decrease. Such target thicknesses are highly sensitive to the laser intensity contrast, even on the picosecond time scale. Given, that the background ASE pedestal drives a shock wave which breaks out at the rear surface of ultra thin targets before the main laser pulse arrives on target, disrupting the TNSA mechanism, this is likely the cause for such observed decreases. Improvements in laser contrast would however enable experiments to take place using much thinner targets, granting access to a possible new regime of laser-solid interactions.

In the micron-scale target thickness regime laser-solid interactions are dominated by the transport of fast electrons through the bulk of the initially opaque, cold target. Conversely for ultra-thin targets the combined effects of the target thickness being of a similar scale to the skin-depth and the onset of relativistic induced transparency results in the electrons which constitute the target bulk experiencing the laser field directly. This changes the dynamics of the interaction significantly [67].

In this chapter, the results of a recent experiment using the Astra-Gemini laser with a laser-intensity contrast sufficiently high to enable targets with thickness $\leq$100 nm to be shot are discussed. With the aid of a novel diagnostic technique designed specifically for this experiment a measurement is made of the angular distribution of the escaping fast electrons across a parameter space including laser

intensity, polarisation and target thickness to investigate laser-solid interactions in the "ultra-thin" target regime.

7.1 Experimental Methods

The Astra-Gemini laser based at the Rutherford-Appleton Laboratory (RAL), UK, as described in **chapter 4** is a dual beam Ti:Sapphire laser operating at 800 nm. Each arm is capable of delivering up to 12 J on target in a 40 fs pulse. In this experiment an f/2 off-axis parabola configuration was used, enabling a $\approx$1.5 μm spot at best focus. A double plasma mirror system is used in order to improve the laser intensity contrast. Measurements show the contrast to be $\leq 10^{-11}$ on the nanosecond time scale and $\leq 10^{-6}$ on the picosecond time scale.

In order to measure the angular distribution of the escaping fast electrons, a novel scintillator based diagnostic technique was developed. In Fig.7.1 a photograph is shown of the multichannel scintillating electron detector (henceforth abbreviated as the "MuSE" detector). This diagnostic consists of 30 individual channels placed in 20^o intervals at the front side (laser side) of the target, although 5^0 resolution is possible, and in 5^o intervals at the rear side of the target. The detector is set 15^o below the target plane to enable access for a magnetic spectrometer and a "kicker magnet" which acts to remove charged particles from the line of sight of the scintillators, enabling a measurement of the proportion of the detected signal which consists of x-rays.

A single channel of the MuSE detector consists of a 5x5x30 mm $CdWO_4$ scintillator. This scintillator is coupled to a light guide whose input face is 5x5 mm and tappers to a 1 mm diameter output face. In order to enhance light transfer between the exit of the scintillator and the entrance to the light guide a small amount of refractive index matching gel is inserted at the interface. This scintillator-light guide couplet is then wrapped with diffusely reflecting aluminium tape. This ensures that any light which could escape through any face other than the exit face is reflected back into the scintillator-light guide couplet. A schematic of this is shown in Fig.7.2. The exit face of the light guide is then coupled to an

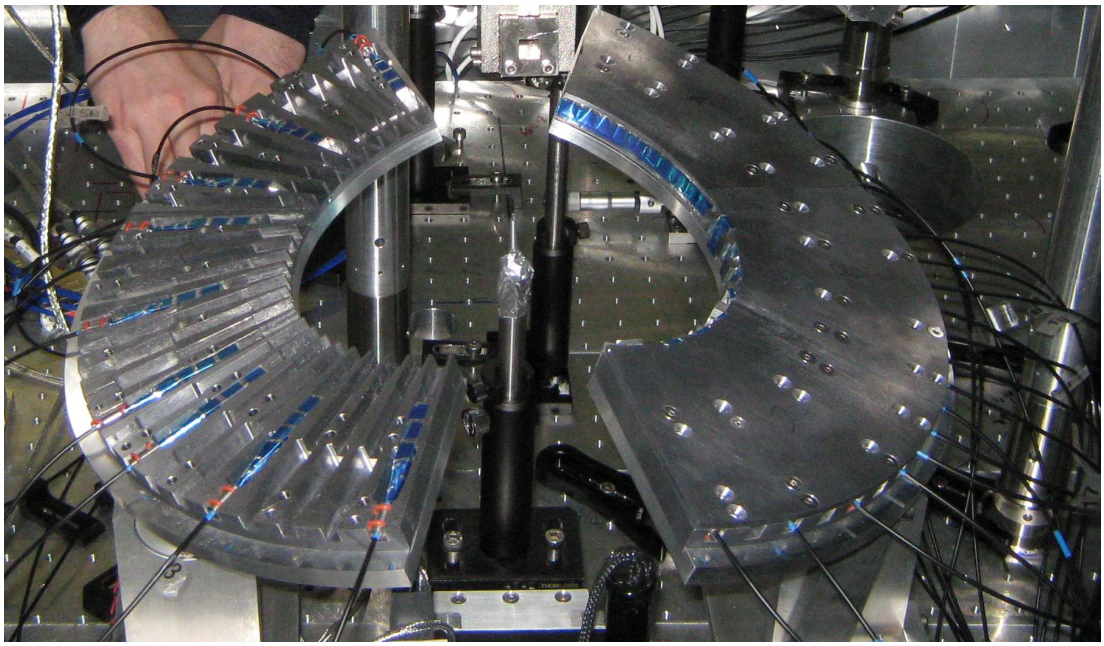

Figure 7.1: Image of MuSE detector in chamber. Notice both the front and rear sides of the target are covered by the diagnostic.

optical fiber. All of the output fibers are then coupled to a grid which is imaged by a 16-bit CCD camera (see Fig.7.3(a)) with an f/1 collection optic attached. A typical image captured with the CCD of the MuSE diagnostic is shown in Fig.7.3(b). Each of the bright circular sources is an end face of an optical fiber.

In order to measure the signal from each channel a simple image analysis algorithm was developed. Initially a diode laser is used to light up individual channels and an image is captured of the fiber output. For a given channel this image is first 'thresholded' by only selecting values above the image background and then 'binarized' by converting the below threshold values to zero and the above threshold values to a value of one. The result is an image whose pixel values consist of zeros everywhere except at the location of the output fiber whose values are all equal to one. By multiplying this image matrix by an image of the full grid (such as that in Fig.7.3(b)) an image is returned whose only non-zero values are those at the location of the fiber output. The total signal in this region is then measured. This process is repeated for each of the channels.

A check of this algorithm is to input an image with identical non-zero values. In Fig.7.4(a) a measurement is made of the total signal inside the area of the

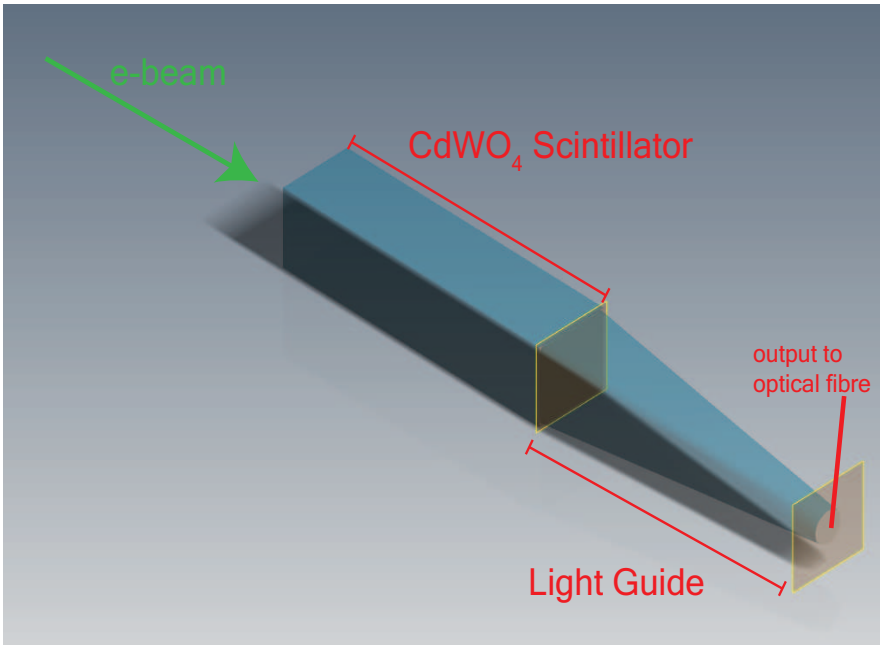

Figure 7.2: Schematic of a single channel of the multichannel scintillating electron detector (MuSE).

fiber output as provided by the binary image. Despite a uniform input image, the output values are nonuniform. This is a result of the fact that the channels have different optical throughputs. As such the binary mask for a given channel has a slightly different area due to the roll-off of the intensity profile at the fiber edges. By dividing the signal by number of pixels in this area however, the slight differences in sample size can be accounted for producing a flat signal as shown in Fig.7.4(b).

The algorithm accounts for the fact that there are different optical throughputs for each channel. A measurement is made using a uniform light source of the pixel count recorded on the CCD for each channel. An arbitrary value is chosen (in this case $2^{16}/2$) and the signal is then multiplied or divided such that the output of the channel equals this value, resulting in a flat field of points. Using this calibration process on real experimental shots results in a measurement of the mean signal for a given channel relative to this initial value.

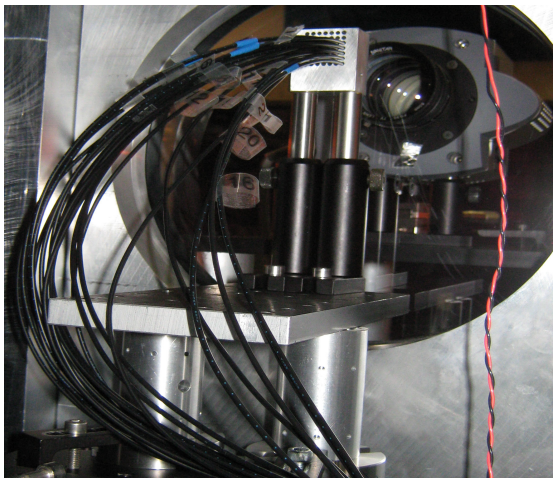

(a)

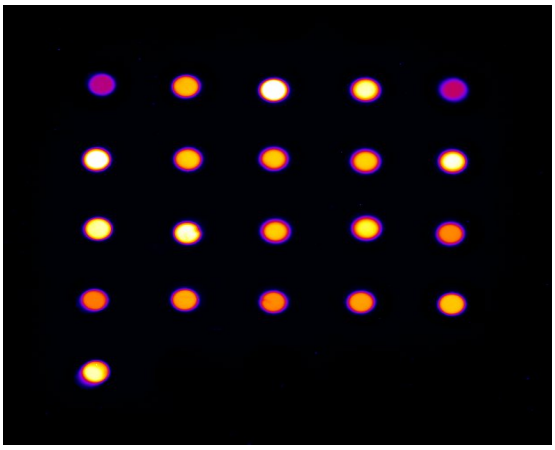

(b)

Figure 7.3: (a)Photograph of the fiber termination grid being imaged by Andor iXON 16-bit EMCCD. (b) Typical on-shot image recorded by CCD.

7.2 Experimental Results

In this section the experimental measurements made using the MuSE detector across a wide range of parameters including laser intensity, polarisation and target thickness are introduced. In Fig.7.5(a-d) the angular distribution of escaping electrons is plotted in polar coordinates for four different laser pulse intensities using a 40 nm aluminium target and linearly polarised pulses. The intensity in this case is changed by changing the energy in the pulse.

At the lowest intensities the angular distribution is broad, peaking slightly either side of the laser axis. However, as the laser intensity is increased a bright peak in the angular emission is observed, centered on the laser direction. Increas-

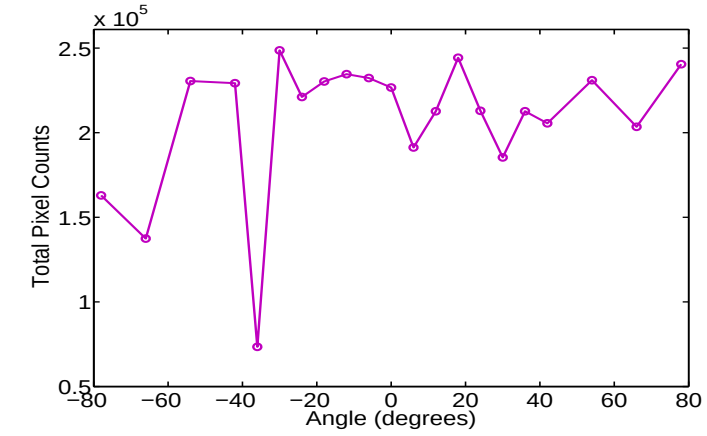

(a)

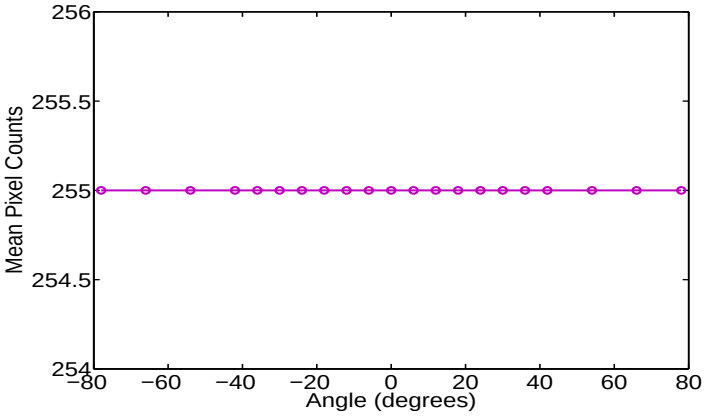

(b)

Figure 7.4: Output of image analysis algorithm, each data point represents a scintillator channel which is placed at a angle around the target, relative to the laser axis, specified by the x-axis. (a) Output for the algorithm when only measuring the total signal from a given channel. Despite using a uniform input image the output is non-uniform. (b) By modifying the algorithm to measure the mean signal of a given channel, instead of the total, the impact area and edge effects are mitigated. For the same uniform input image, a uniform output is produced.

ing the intensity further still reveals a rapid increase in the magnitude of this peak. For intensities beyond 5.5×10^{20} W/cm^2 an increase of $\geq$30 times in the on-axis signal is recorded with respect to shots at lower intensities.

In contrast, shots on the same targets, and at similar intensities, for circular polarisation show no such onset of a bright on-axis feature of a similar magnitude. Further shots on targets of 100 nm and 1μm thickness, using linear polarisation, appear much like the lowest intensity cases where the recorded distribution is low in signal and broad with no obvious central peak.

In order to compile these results together, the channels which constitute $\pm 18^o$

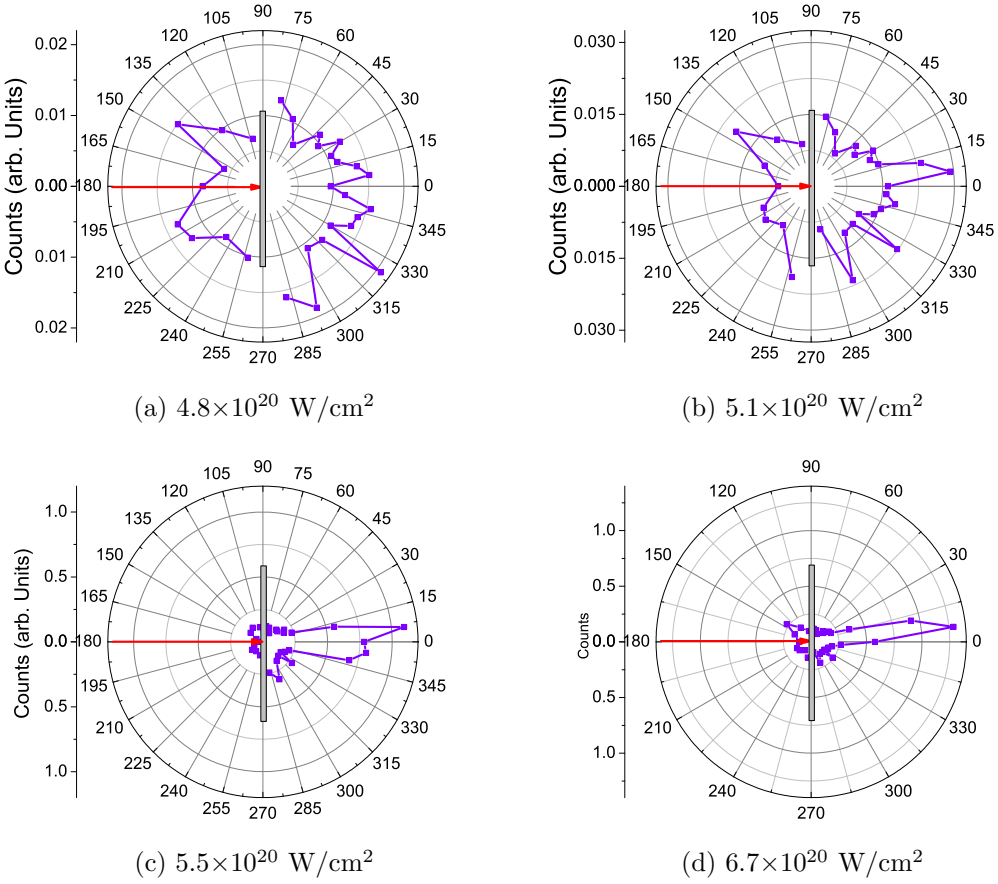

(a) 4.8×10^{20} W/cm^2

(b) 5.1×10^{20} W/cm^2

(c) 5.5×10^{20} W/cm^2

(d) 6.7×10^{20} W/cm^2

Figure 7.5: (a)-(d) The measured angular distribution of electrons for 40 nm targets and linearly polarised laser pulses. The clear formation of a bright on-axis electron peak is observed with increasing intensity. Also note the differences in scale.

around the central axis are extracted and integrated to get the total number of counts in the peak. The process is repeated for all of the intensities investigated for each polarisation and target type. The result is shown in Fig.7.7. The transition into a regime of a strongly peaked on-axis distribution is clear in this plot for the shots involving 40 nm Al at linear polarisation. For other parameters the lack of such a transition is obvious.

In all cases the electron signal is somewhat directionally biased, in the laser forward direction. However only in the 40 nm, p-polarised case when the laser intensity is above a certain threshold does the signal peak strongly along the laser axis. There are two obvious possibilities regarding the onset of this directional peak in electron emission. The first, a new mechanism whose onset occurs under these particular conditions. The second, the same mechanism as that driving

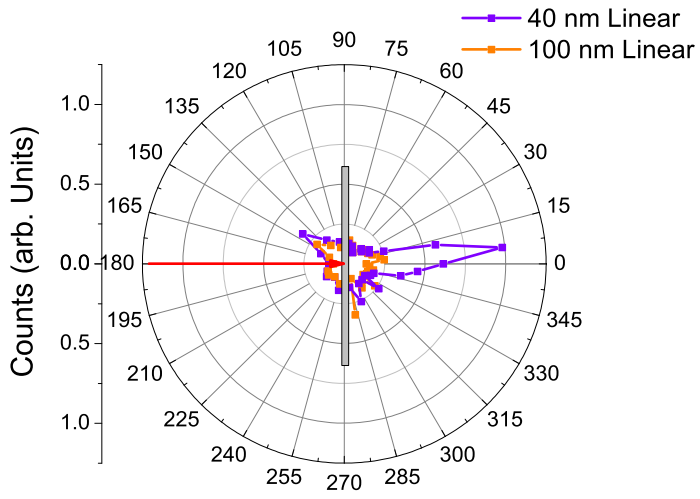

(a)

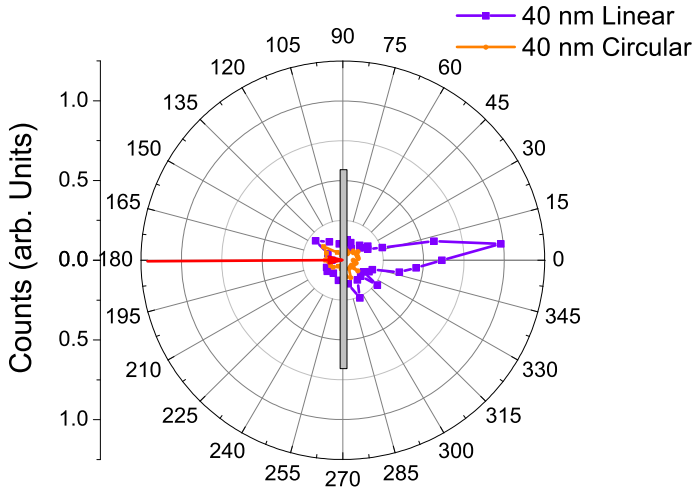

(b)

Figure 7.6: (a) Comparison of the angular distribution shown in Fig.7.5 for 40 nm Al, linear polarisation and 100 nm targets for the same intensity (5×10^{20} W/cm^2). (b) Comparison of the angular distribution for linear and circular polarisation for 40 nm targets and constant laser intensity equal to 5×10^{20} W/cm^2.

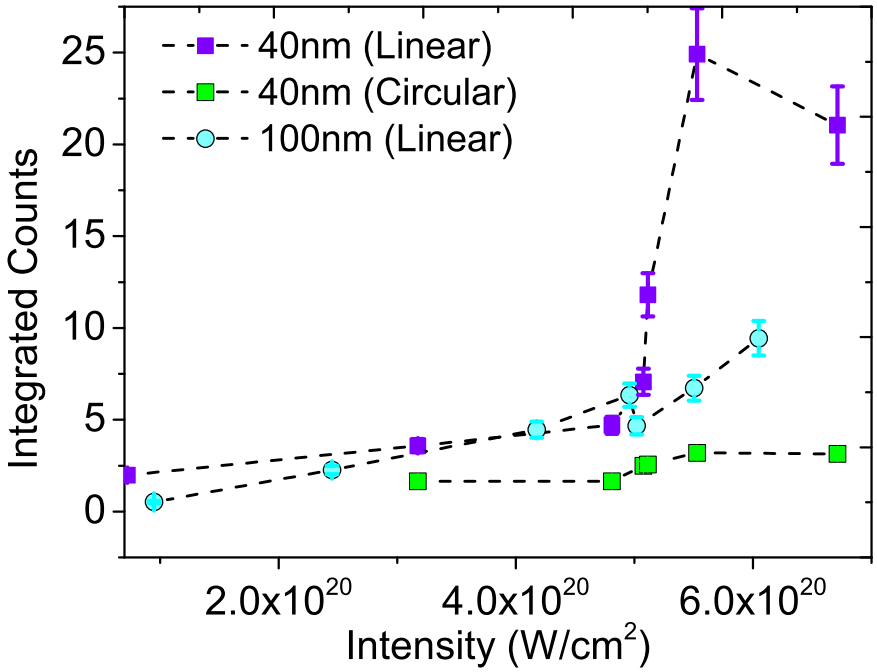

Figure 7.7: Integrated signal for channels between $\pm 18^0$ from the laser axis as a function of intensity for given laser and target parameters

electron acceleration at lower intensities, but one which becomes significantly more efficient under conditions at higher intensities, a specific target thickness and laser polarisation. In order to study this effect further 2D particle-in-cell (PIC) simulations were carried out and will be discussed in the following section.

7.3 PIC Simulations & Discussion

Using the 2D PIC simulation code EPOCH the laser-target interaction is simulated at an initial density of $100 n_{crit}$. Three species are used in the simulation: electrons, aluminium ions and a thin, 8 nm, layer of protons on the target rear surface in order to facilitate the TNSA acceleration of protons. Simulations for these conditions are then conducted for a range of intensities from $1 - 5 \times 10^{20}$ W/cm^2, polarisations (including circular and linear pulses) and target thickness, including 40 nm and 100 nm targets.

The experimental results suggest an effect which increases the number of

escaping electrons as the laser intensity is increased. Moreover, that this increase is spatially localised around angles close to the laser axis. As such, the electron density (n_e), the per-cell averaged electron kinetic energy ($\bar{T}$) and the electric field in the laser polarisation plane (E_y) are initially extracted. In addition, the electron spectra are extracted by splitting the parameter $\bar{T}$ into different energy bins. The indices for the cells in a given energy bin are found and used to extract the electron density at that cell position. Based on the grid size the total number electrons in a given cell is calculated and summed up, with cells in the same energy bin. This then provides a value for the number of particles for a given energy, from which to construct the energy spectra.

In Fig.7.8(a)-(f) the simulation parameters n_e/n_{crit}, $\bar{T}$ and E_y are shown for a 40 nm target and a linearly polarised laser pulse at 3×10^{20} W/cm^2 and 5×10^{20} W/cm^2, 42 fs into the simulation. Looking initially at the electron density pseudocolour plots, in the lower intensity case the target is seen to deform as the electrons are driven forward by the laser pulse. Some of the electrons at this point in the simulation ($\approx$20 fs after the peak of the laser pulse) have been ejected from the target, reducing the number of electrons in the focal spot. Nevertheless the target remains opaque to the laser, including later in time as the laser electric field decays to zero. In the higher intensity case however, it appears that the rate of attrition of electrons from the laser focal spot is sufficiently high that as the laser intensity peaks the combined effect of a reduced n_e and an increased γn_{crit} results in the target becoming transparent to the incoming laser pulse. The difference between the two cases is clear when looking at the electric field in the plane of the laser pulse. Here it can be seen that the laser pulse is reflected from the target surface at 3×10^{20} W/cm^2, but at 5×10^{20} W/cm^2 it is clearly transmitting through the target. Finally, looking at the pseudocolour plot for the average per-cell electron kinetic energy, the transmitted laser pulse now interacts directly with electrons previously accelerated from the target, leading to an enhancement of the electron energy in that region.

These initial observations of the 2-D data suggest that the electron emission peak coincides with the onset of relativistic induced transparency (RIT). However,

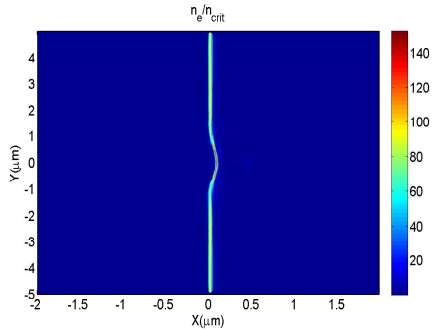

(a) n_e/n_{crit} - 3x10^{20} W/cm^2

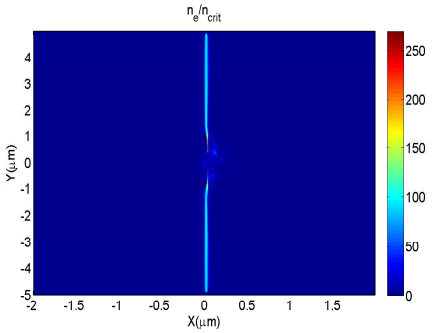

(b) n_e/n_{crit} - 5x10^{20} W/cm^2

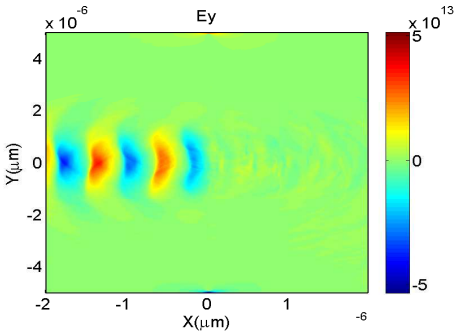

(c) E_y - 3x10^{20} W/cm^2

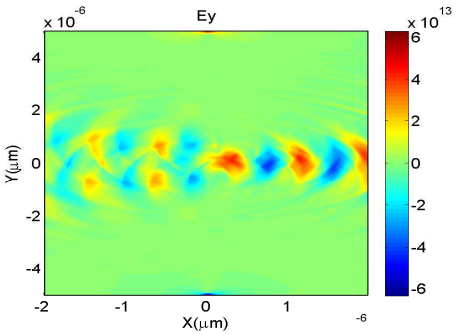

(d) E_y - 5x10^{20} W/cm^2

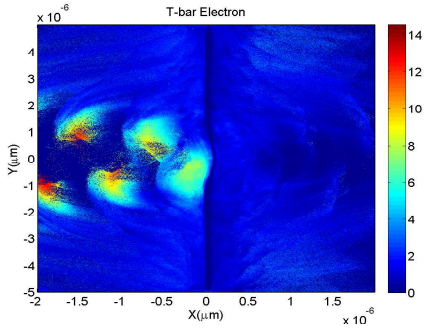

(e) T - 3x10^{20} W/cm^2

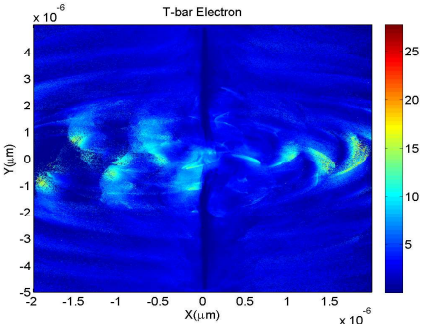

(f) T - 5x10^{20} W/cm^2

Figure 7.8: (a)-(f) 2D-pseudocolour plots of n_e/n_{crit}, T and E_y for 3x10^{20} W/cm^2 and 5x10^{20} W/cm^2. In the lower intensity case the laser pulse is observed to reflect at the critical surface. For higher intensities the laser pulse is observed to propagate through the target

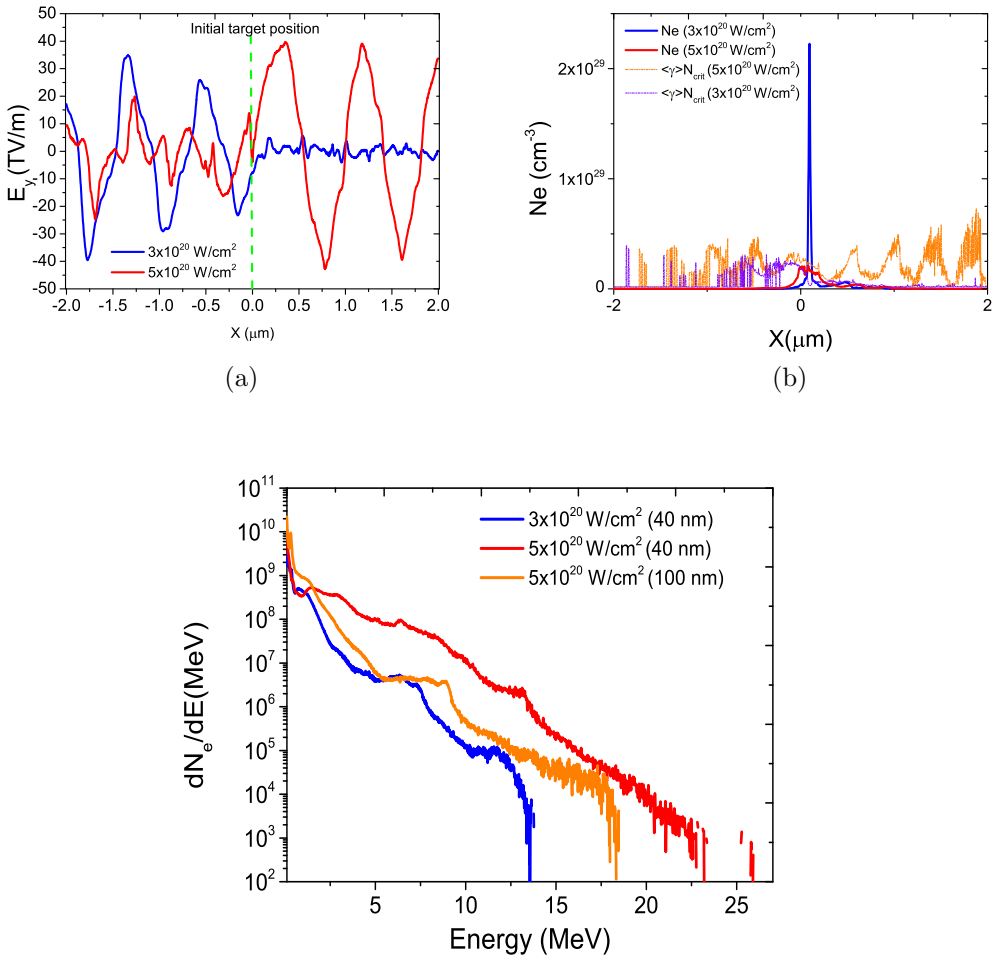

(a) (b)

(c)

Figure 7.9: (a) Plot of E_y for both 3x10^{20} W/cm^2 and 5x10^{20} W/cm^2 at 43 fs into the simulation. The laser pulse is clearly seen to be transmitted through the target in the higher intensity case. (b) Plot of n_e and γn_{crit} for both 3x10^{20} W/cm^2, 5x10^{20} W/cm^2. (c) Electron spectra at 43 fs into simulation for 3x10^{20} W/cm^2 and 5x10^{20} W/cm^2 for a 40 nm target and 5x10^{20} W/cm^2 for a 100 nm target.

this is observed at intensities significantly lower than are required for solid density aluminium to become transparent, as this would require intensities on the order of 10^{23} W/cm^2. Instead, it must be that the laser pulse is interacting with densities significantly lower than this due to the dynamic expulsion of electrons from the focal spot. In order to confirm this a line-out of n_e along the laser axis is extracted. Similarly a line-out in $\bar{T}$ is extracted. Using this energy, the per-cell average gamma factor is calculated for both the lower and higher energy cases. From here the value of the n_e line-out is first plotted in both cases. The values of the γn_{crit} line-out in both cases are then also plotted on top of this, shown in Fig.7.9(b). Clearly, in the instance that $n_e < \gamma n_{crit}$ the plasma has become transparent to the laser pulse. In Fig.7.9(b), in the lower intensity case the target density is significantly higher than γn_{crit} as a result the laser pulse is reflected. In the higher intensity case (i.e the intensity corresponding to the onset of the peak seen in the experimental data) it is found that $\gamma n_{crit} > n_e$ in the simulation. As a consequence the pulse is transmitted through the target. It can be stated then, and with some confidence, that the effect observed is in fact RIT since if the γ factor were not included the target would still be opaque to the laser pulse. Moreover, it is clear that this effect also requires the decompression of the target to take place as even for the largest gamma factor at these intensities, the solid density is still significantly larger. Note also, in the case where RIT does take place the oscillations in γn_{crit} as the laser pulse interacts with the escaping electrons. The periodicity of this oscillations is found to be $\approx 2\omega$. This is a clear signature of additional ponderomotive acceleration of the escaping electrons as the laser pulse is now able to interact directly with all of the electrons along the axis of propagation.

In order to link these results back to the experimental data it is necessary to investigate how this transition to an induced transparency regime effects the overall laser to fast electron energy conversion efficiency and the electron spectrum. In Fig.7.9(c) the electron spectrum for the lower and higher intensity cases is plotted. Here it can be clearly seen the electron spectrum is enhanced both in numbers, often by more than an order of magnitude, and in cut-off energy

for the higher intensity case. In both cases, however, the energy spread remains broad. Also included in this plot is the electron spectrum for a 100 nm target, at the same intensity as the case where RIT is observed. Experimentally, at this intensity and target thickness the onset of the bright on-axis peak is not observed. Similarly, in simulations, the onset of RIT is not observed for 100 nm targets. This scenario then is a good test of whether the enhancement seen in the electron energy spectrum is a result of the onset of RIT or purely just as a consequence of the increased intensity. In fact, the first of these points is observed to be the case. Whereas, the cut-off energy and numbers are seen to be enhanced when compared to the 40 nm, 3×10^{20} W/cm^2 case, the enhancement in both the number and cut-off energy is still significantly less than in the instance that RIT is observed. Also note the similarity in spectral shape for the two cases where RIT does not occur and, the marked change in the case where RIT does occur. This difference may be of interest, experimentally, as a signature of the onset of the RIT regime.

Moving now to consider the effect of changing polarisation on the onset of RIT. Recall, in the experimental section of this chapter the onset of the bright on-axis peak was observed to be sensitive to not only intensity but polarisation. Specifically, for the same intensity where RIT is observed for linear polarisation, when the polarisation is changed to circular, no such peak is observed. Plotting, in Fig.7.10, pseudocolour plots (as before) of the simulation parameters n_e/n_{crit}, $\bar{T}$ and E_y we note three key features. One, there is no RIT in this instance despite being at the same intensity as in the linear case. Two, instead of the rapid decompression of the electron population within the target we see a compression of the electrons at the laser front. Finally, the cut-off energy of the electrons in the simulation are significantly lower than seen in the linear case at the same intensity.

This result is of particular interest if considered in the context of the previously described radiation pressure regime (RPA) of ion acceleration, a mechanism which is predicted to become important for intensities above 10^{20} W/cm^2 and circular polarisation [30]. In this instance, the so-called "light sail mode", the

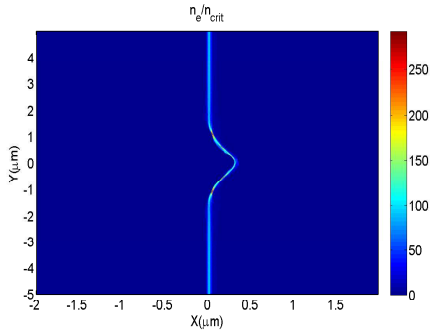

(a) n_e/n_{crit} - 5×10^{20} W/cm^2 (circular)

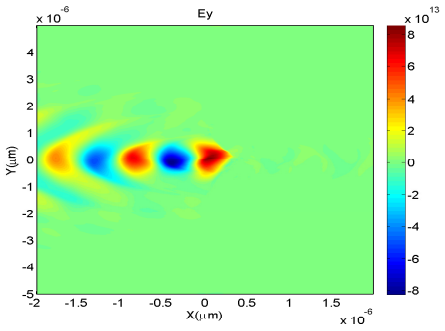

(b) E_y - 5×10^{20} W/cm^2 (circular)

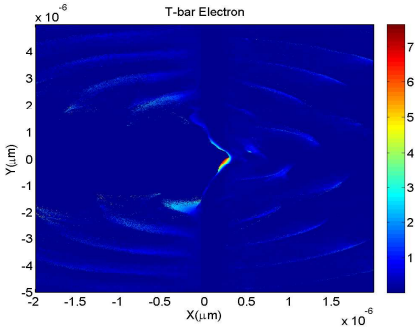

(c) T - 5×10^{20} W/cm^2 (circular)

Figure 7.10: Plots of n_e/n_{crit}, E_y and T for a 40 nm target and circular polarisation at 5×10^{20} W/cm^2. Despite the same intensity and target thickness as in the linear case, for which RIT is obtained, no RIT is observed for circular polarisation.

enhanced ion acceleration predicted for this mechanism, compared to TNSA, is contingent on having a highly reflecting plasma slab. In the linear polarisation case, electrons gain energy through the ponderomotive drive of the laser. This results, as seen earlier, in the ejection of MeV electrons from the target at twice the laser frequency, which in turn results in the rapid decompression of the target. As discussed earlier, under the right conditions this decompression will eventually lead to RIT. By using circular polarisation this oscillatory component of the fast electron generation is suppressed and instead electron acceleration is dominated by the slowly varying ponderomotive push, the magnitude of which follows the laser temporal-intensity profile. This stops the target from decompressing and enables electrons and ions to gain energy over the duration of the laser pulse length.

Applying the same technique as previously used to extract the electron energy spectrum, the energy spectrum of the proton and aluminium ions in the target are extracted. In the lower intensity linear case we see a sharp cut-off at around 3.5 MeV for the protons and 0.5 MeV for the Al ions. In comparison to the threshold intensity of 5×10^{20} W/cm^2 where RIT is observed, the proton spectrum is significantly lower in energy and numbers. The cut-off energy and spectral shape for the Al ions in this case is similar to that at lower intensities. For circular polarisation the proton cut-off energy and overall numbers is lower still than even the low intensity linear case. This suggests that we are still in a TNSA phase of ion acceleration given the sensitivity of the ion cut-off energy to the electron temperature. However, one feature of note is that the difference in energy between the Al ions and protons in the circular case is much smaller than any other case. This effect is characteristic of the onset of a radiation drive where there is a increased energy equilibration between ion species. However, no mono-energetic features are observed as would be expected if we had entered into a pure light sail mode of ion acceleration. In this parameter space of target thickness and laser intensity we appear to be in a transitory phase. In the linear case there is a transition to a relativistic induced transparency regime due to the significant electron heating induced by the $\mathbf{j}\times\mathbf{B}$ mechanism. In the circular case

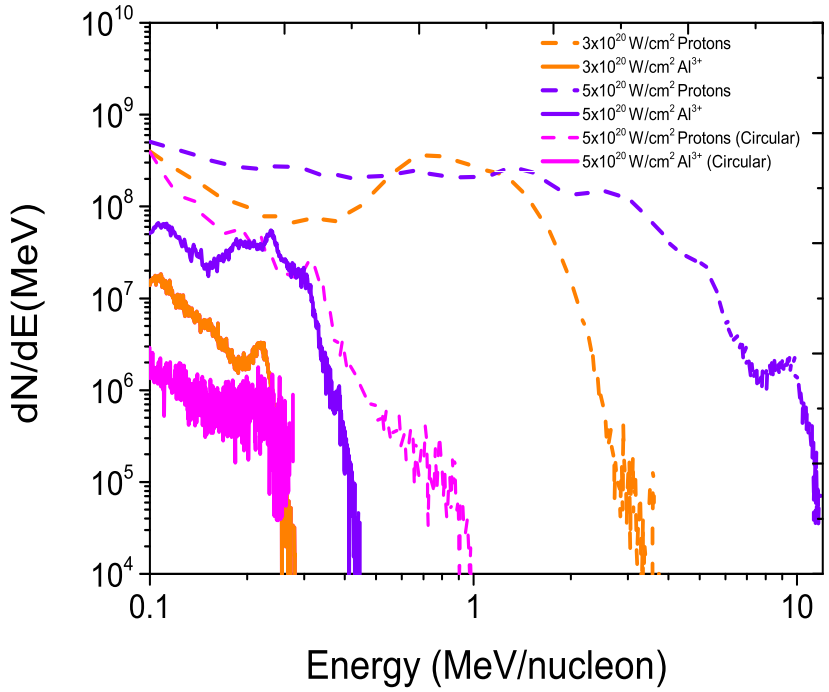

Figure 7.11: Plots of simulated spectra for protons and Al^{3+} ions. We compare the cases of intensities below and above this threshold for the linear and circular polarisation case.

the onset of a radiation drive regime is observed, evidenced by the compression of the electron layer and the increasing energy equilibration between ion species.

7.4 Conclusion

In conclusion, a regime of intense laser-solid interactions in which the onset of relativistic induced transparency occurs for initially solid targets has been demonstrated both experimentally and in simulations. This onset is found to be sensitive to laser intensity, polarisation and target thickness. The key experimental signature of this onset is the formation of a bright on axis peak in the electron angular distribution. In simulations good agreement with this change in the electron emission is found. Moreover, with the aid of simulations it is demonstrated that the enhancement in the on axis electron emission is directly as a result of the onset of RIT. This enhancement is identified as an overall increase in both numbers and cut-off energy in the electron spectrum.

This study began with the development of a new diagnostic, named the MuSE detector, consisting of a multi-channel array of scintillator-light guide couplets placed 360^o around the target. The detected signal is confirmed to be electrons by inserting a magnet in front of the detector and measuring the large decrease in signal.

Using this diagnostic the electron angular distribution is measured for a range of laser and target parameters. The dependence of the magnitude of the forward-directed electron signal is measured as a function of laser polarisation, and intensity, and target thickness. For 40 nm targets irradiated with linearly polarised laser pulses with peak intensities of $>5\times10^{20}$ Wcm^{-2}, the large on-axis peak in the electron signal is observed. By then varying the intensity for fixed polarisation and target thickness, a threshold intensity is clearly demonstrated (for 40 nm foils and linear polarisation). Above this threshold, and consistently for a number of intensities, the on-axis signal is measured to increase by more than an order of magnitude as compared to lower intensities. The effect of target thickness on RIT is also considered. It is shown in simulations that RIT does not occur for the previous threshold intensity with targets thicker than 40 nm. Likewise, there is no bright on-axis peak measured experimentally for such targets

By changing the polarisation to circular and keeping the intensity above the threshold intensity which induces RIT for 40 nm Al and linearly polarised pulses it is observed that RIT does not occur. Again, there is no on-axis peak measured experimentally. However, in simulations a distinct change in the dynamics of the interaction is found. The ejection of electrons from the focal spot is much reduced. As such the target density does not decrease and RIT is unable to occur for the laser intensities available. Instead, since the oscillatory $\mathbf{j} \times \mathbf{B}$ component is suppressed with circular polarisation, an increase in the density of the n_e layer below γn_e is observed as the laser pulse intensity increases over the pulse envelope. This results in the target remaining opaque to the laser pulse for its duration. Previous theory indicates the onset of a radiation drive mechanism for ions in this parameter space. Some supporting evidence is observed such as an increasing equilibration of energy between the various ion species. However no

mono-energetic or even quasi-mono-energetic spectral shape is observed, which suggests that the full light-sail mode of ion acceleration has not yet been entered.

Overall, a regime of laser-solid interactions was investigated in which the dynamics are highly sensitive to the laser intensity, polarisation and target thickness. It has been demonstrated both in experiments and in simulations that for linear polarised pulses above an intensity of 5×10^{20} W/cm^2 with a target thickness of 40 nm, relativistic induced transparency occurs and that this leads to a large increase in the numbers of escaping electrons. Future work in this area will explore this regime further and investigate opportunities to use this bright electron source to drive secondary processes such as gamma-ray and positron production.

Chapter 8

Summary & Conclusions

The work contained in this thesis has lead to a number of important insights into the nature of laser absorption and fast electron generation in ultraintense laser solid interactions. In this final chapter these results will be summarised.

8.1 Surface transport of fast electrons at large incidence angles

While it is true that there had been studies prior to this work investigating the surface guiding effect at large incidence angles [60, 61, 84], the intensities used were only just high enough to be in the relativistic regime. For an effect which is essentially formed by the self-generated magnetic field of relativistic electrons, this is a critical factor. In addition, in the previous studies at lower laser intensities it was not possible to simultaneously measure the proton emission, and diagnose the population of fast electrons reaching the rear of the target. The results presented in **chapter 5** demonstrate the onset of surface guiding, at oblique incidence angles, for laser intensities $> 10^{19}$ W/cm^2. In good agreement with previous experiments, and theoretical models [62] it is found that for laser incidence angles $> 65^0$, the emission direction of escaping fast electrons is shown to shift from predominantly laser axis directed to the target front surface. However, moving a step further by looking at proton emission from the rear target normal in

conjunction with the model of Mora [21], it is demonstrated that a significant population of fast electrons is also accelerated longitudinally into the target, regardless of incidence angle. Changes in proton cut-off energy, which are related to fast electron temperature and number density, can be accounted for by considering only changes in the laser intensity with incidence angle. When the intensity is held constant with incidence angle, such changes are not observed, while the same changes to the escaping electron distribution are. This result has important consequences for proposed applications of surface guided transport including cone guided fast ignition and, in addition, ion acceleration.

8.2 Enhanced laser-electron coupling using a controlled plasma density gradient

In short pulse laser-solid interactions the effect of a plasma density scale length on the conversion of laser energy into fast electrons has been a contentious issue. Some studies show that this in fact degrades the absorption [95], while many others say the opposite [28, 58, 96] . If the latter is true it is also worth establishing if it is possible to use this effect to optimise absorption. For many proposed applications of laser-solid interactions to be practicable the interaction must be as efficient as possible, making such measurements of critical importance. The results presented in **Chapter 6** demonstrate that using a controlled density gradient on the front surface of the target, the coupling of laser energy into fast electrons can be enhanced. Experimental results demonstrate that there is an optimum density profile for which this is the case, and this optimum is measured using a number of different experimental diagnostics. The density profile generated by the long pulse beam is modelled using the radiation-hydrodynamic code HELIOS and is then used as an input to the PIC code EPOCH. These simulations demonstrate that the optimum in absorption is in fact a consequence of the enhanced laser intensity at the critical density surface due to laser self-focusing in the underdense region of the plasma profile. This process is also shown to be dynamic, as electrons are swept from the laser axis, the self focusing effect

reduces and the absorption between various profiles becomes more comparable. For longer density scale lengths the reduction in absorption is observed to be a consequence of laser filamentation in the plasma, in agreement with previous experimental studies. These results are of fundamental importance for all applications of intense laser-solid interactions. Further work in this area would also be of great use. An expanded program of simulations would likely provide further insight especially at longer times scales. Future experimental work could also explore the dynamics of the self focusing effect by using shaped temporal profiles or shorter laser pulses.

8.3 Laser absorption to fast electrons in the transition to the relativistic induced transparency regime

For targets of micron-scale thickness, electrons are accelerated at the critical surface or in the preplasma and injected into the solid density target bulk. The electrons then experience a multitude of transport effects, including filamentation, magnetic pinching and collisions. For nanometer-scale targets however these transport effects become less important and instead electrons, even in the bulk of the target, begin to directly experience the laser field [67]. The extent to which this changes the dynamics of the interaction and, especially, the conversion of laser energy into fast electrons is important for many potential applications of laser-solid interactions. The results presented in **chapter 7** demonstrate that in this regime, for linear laser polarisation and above a certain intensity, the nanometer-scale target becomes relativistically transparent. PIC simulations show that as the laser pulse initially interacts with the plasma slab, electrons are ejected from the focal spot. Consequently the electron density is reduced in this region. For sufficiently intense laser pulses the electrons are driven to high enough relativistic velocities that the target becomes relativistically transparent. It is the combination of both effects that make this possible. Experimental results, using a novel

scintillator based electron detector, show that for the condition of transparency a bright on-axis jet of high energy electrons forms, indicating a significantly enhanced electron coupling mechanism. Both experimentally and numerically, when the laser polarisation is changed to circular, relativistic induced transparency is not observed. This is attributed to the suppression of the $\mathbf{j} \times \mathbf{B}$ force at this polarisation. Such control over the generation of fast electrons could have important consequences for laser driven ion acceleration. In addition, the intense beam of escaping fast electrons for the condition of transparency may have applications in driving secondary sources of intense x-rays and γ-rays.

8.4 Future Work

The advent of short pulse, high power lasers capable of generating relativistic electrons as well as beams of high energy protons and gamma-rays has, for the past decade and a half, offered great promise for a number of applications including laser driven ion therapy and the fast ignition approach to inertial confinement fusion. However, in order that these applications are realised it is of fundamental importance that a greater understanding is reached regarding fast electron generation and, in particular, the active manipulation of plasma and laser conditions in order to enhance the fast electron generation processes. There are a number of routes to achieving this but from the experimental point of view there are some clear areas for development in the future.

The nature of ultraintense laser-solid experiments, principally due to the expense, typically precludes petawatt-class laser systems operated by single research groups. It is far more common for the laser systems of this scale to be based at national labs or equivalent (LLNL or RAL for example). This naturally leads to short duration, scheduled experiments. In order to therefore extract the most from a given experiment in my opinion three areas require development. First of all, better diagnostics should be developed, with better calibrated response in the harsh laser-plasma environment. Additionally there should be a focus on transitioning from passive film based diagnostics to active diagnostics enabling a

significantly higher repetition rate. This leads to the second area, better handling of data, which means better analysis software which is correctly benchmarked with input calibration data. Finally, an overall transition both in experimental methods and, in thinking, to handle ever higher laser repetition rates. Technologically, it should be possible to transition into a regime of working in which, in the future, more ultra-high intensity laser shots on solid targets can be taken in a single day than have been taken to date in the entire history of the field. Such high data rates would increase the statistical significance, and therefore confidence in recorded data. Ultimately this leads to a more detailed understanding of laser-solid interactions and, therefore, much greater control over them. Developing this experimental ecosystem; better diagnostics, better analysis and higher data rates would be a major step forward in understanding ultraintense laser-solid interactions.

Perhaps the area, in all of these regards, which is leading the way is that of interactions in the ultra-thin target regime highlighted in **chapter 8**. These are inherently easier to probe as transport effects, which are notoriously difficult to measure experimentally, are avoided. Moreover, given that it is possible to access this regime with lasers already capable of relatively high repetition rates, the only obstacles that remain in the way of highly detailed studies in this regime are diagnostic techniques and data handling. Some progress toward the first of these was demonstrated in **chapter 8** but continued development is still required. The second of these is also an ongoing effort.

The great potential for such interactions is obvious and has been highlighted by a number of authors. In particular, the proposed mechanisms of ion acceleration such as the light sail mode of radiation pressure acceleration [30, 97] and the breakout afterburner mechanism [68] predict ion energies much in excess of what has been possible to date. Both approaches rely on interactions in this ultra-thin nanometer scale regime. In order for such processes to be realised and for laser-plasma interactions to move towards a universally recognised platform for applied physics and as a basis for advanced technologies a step change toward this stronger experimental ecosystem must occur.

Bibliography

[1] TH Maiman. Stimulated optical radiation in ruby. *Nature*, 187(4736):493–494, 1960.

[2] J Nuckolls, L Wood, and A Thiessen. Laser Compression of Matter to Super-High Densities: Thermonuclear (CTR) Applications. *Nature*, 239(5368):139–142, 1972.

[3] J.D. Lawson. Some criteria for a power producing thermonuclear reactor. *Proceedings of the Physical Society. Section B*, 70:6, 1957.

[4] D. Strickland and G. Mourou. Compression of amplified chirped optical pulses. *Optics Communications*, 56(3):219–221, 1985.

[5] M. Tabak, J. Hammer, ME Glinsky, and WL Kruer. Ignition and high gain with ultrapowerful lasers. *Physics of Plasmas*, 1(5):1626–1634, 1994.

[6] M. Borghesi, A. Mackinnon, A. Bell, G. Malka, C. Vickers, O. Willi, J. Davies, A. Pukhov, and J. Meyer-ter Vehn. Observations of Collimated Ionization Channels in Aluminum-Coated Glass Targets Irradiated by Ultraintense Laser Pulses. *Physical Review Letters*, 83(21):4309–4312, 1999.

[7] J R Davies, A R Bell, M G Haines, and S M Gue. Short-pulse high-intensity laser-generated fast electron transport into thick solid targets. *Physical Review E*, 56(6):7193–7203, 1997.

[8] A. Bell and R. Kingham. Resistive Collimation of Electron Beams in Laser-Produced Plasmas. *Physical Review Letters*, 91(3):1–4, 2003.

[9] J. Santos, F. Amiranoff, S. Baton, L. Gremillet, M. Koenig, E. Martinolli, M. Rabec Le Gloahec, C. Rousseaux, D. Batani, A. Bernardinello, G. Greison, and T. Hall. Fast Electron Transport in Ultraintense Laser Pulse Interaction with Solid Targets by Rear-Side Self-Radiation Diagnostics. *Physical Review Letters*, 89(2):8–11, 2002.

[10] K. Lancaster, J. Green, D. Hey, K. Akli, J. Davies, R. Clarke, R. Freeman, H. Habara, M. Key, R. Kodama, K. Krushelnick, C. Murphy, M. Nakatsutsumi, P. Simpson, R. Stephens, C. Stoeckl, T. Yabuuchi, M. Zepf, and P. Norreys. Measurements of Energy Transport Patterns in Solid Density Laser Plasma Interactions at Intensities of 51020Wcm-2. *Physical Review Letters*, 98(12):1–4, 2007.

[11] R. Stephens, R. Snavely, Y. Aglitskiy, F. Amiranoff, C. Andersen, D. Batani, S. Baton, T. Cowan, R. Freeman, T. Hall, S. Hatchett, J. Hill, M. Key, J. King, J. Koch, M. Koenig, A. MacKinnon, K. Lancaster, E. Martinolli, P. Norreys, E. Perelli-Cippo, M. Rabec Le Gloahec, C. Rousseaux, J. Santos, and F. Scianitti. Kα fluorescence measurement of relativistic electron transport in the context of fast ignition. *Physical Review E*, 69(6):3–9, 2004.

[12] X H Yuan, A P L Robinson, M N Quinn, D C Carroll, M Borghesi, R J Clarke, R G Evans, J Fuchs, P Gallegos, L Lancia, D Neely, K Quinn, L Romagnani, G Sarri, P a Wilson, and P McKenna. Effect of self-generated magnetic fields on fast-electron beam divergence in solid targets. *New Journal of Physics*, 12(6):063018, 2010.

[13] J. Green, V. Ovchinnikov, R. Evans, K. Akli, H. Azechi, F. Beg, C. Bellei, R. Freeman, H. Habara, R. Heathcote, M. Key, J. King, K. Lancaster, N. Lopes, T. Ma, a. MacKinnon, K. Markey, a. McPhee, Z. Najmudin, P. Nilson, R. Onofrei, R. Stephens, K. Takeda, K. Tanaka, W. Theobald, T. Tanimoto, J. Waugh, L. Van Woerkom, N. Woolsey, M. Zepf, J. Davies, and P. Norreys. Effect of Laser Intensity on Fast-Electron-Beam Divergence in Solid-Density Plasmas. *Physical Review Letters*, 100(1):1–4, 2008.

[14] P. A. Norreys, R. Allott, R. J. Clarke, J. Collier, D. Neely, S. J. Rose, M. Zepf, M. Santala, A. R. Bell, K. Krushelnick, A. E. Dangor, N. C. Woolsey, R. G. Evans, H. Habara, T. Norimatsu, and R. Kodama. Experimental studies of the advanced fast ignitor scheme. *Physics of Plasmas*, 7(9):3721–3726, 2000.

[15] R Kodama, H Shiraga, K Shigemori, Y Toyama, S Fujioka, H Azechi, H Fujita, H Habara, T Hall, Y Izawa, T Jitsuno, Y Kitagawa, K M Krushelnick, K L Lancaster, K Mima, K Nagai, M Nakai, H Nishimura, T Norimatsu, P A Norreys, S Sakabe, K A Tanaka, A Youssef, M Zepf, and T Yamanaka. Nuclear fusion: Fast heating scalable to laser fusion ignition. *Nature*, 418(6901):933–934, 2002.

[16] S Kar, D Adams, M Borghesi, K Markey, B Ramakrishna, M Zepf, K Lancaster, P Norreys, a P L Robinson, D C Carroll, P McKenna, M Quinn, X Yuan, C Bellei, and J Schreiber. Magnetic collimation of petawatt driven fast electron beam for prospective fast ignition studies. *Journal of Physics: Conference Series*, 244(2):022041, 2010.

[17] A. P. L Robinson, M. H. Key, and M. Tabak. Focusing of relativistic electrons in dense plasma using a resistivity-gradient-generated magnetic switchyard. *Phys. Rev. Lett.*, 108:125004, 2012.

[18] Stephen P. Hatchett, Curtis G. Brown, Thomas E. Cowan, Eugene a. Henry, Joy S. Johnson, Michael H. Key, Jeffrey a. Koch, a. Bruce Langdon, Barbara F. Lasinski, Richard W. Lee, Andrew J. Mackinnon, Deanna M. Pennington, Michael D. Perry, Thomas W. Phillips, Markus Roth, T. Craig Sangster, Mike S. Singh, Richard a. Snavely, Mark a. Stoyer, Scott C. Wilks, and Kazuhito Yasuike. Electron, photon, and ion beams from the relativistic interaction of Petawatt laser pulses with solid targets. *Physics of Plasmas*, 7(5):2076, 2000.

[19] E L Clark, K. Krushelnick, JR Davies, M. Zepf, M. Tatarakis, FN Beg, A. Machacek, PA Norreys, MIK Santala, and I. Watts. Measurements of

energetic proton transport through magnetized plasma from intense laser interactions with solids. *Physical Review Letters*, 84(4):670–673, 2000.

[20] R A Snavely, M H Key, S P Hatchett, T E Cowan, M Roth, T W Phillips, M A Stoyer, E A Henry, T C Sangster, M S Singh, S C Wilks, A MacKinnon, A Offenberger, D M Pennington, K Yasuike, a B Langdon, B F Lasinski, J Johnson, M D Perry, and E M Campbell. Intense high-energy proton beams from Petawatt-laser irradiation of solids. *Physical Review Letters*, 85(14):2945–8, 2000.

[21] P. Mora. Plasma Expansion into a Vacuum. *Physical Review Letters*, 90(18):5–8, 2003.

[22] J. Fuchs, P. Antici, E. DHumières, E. Lefebvre, M. Borghesi, E. Brambrink, C. a. Cecchetti, M. Kaluza, V. Malka, M. Manclossi, S. Meyroneinc, P. Mora, J. Schreiber, T. Toncian, H. Pépin, and P. Audebert. Laser-driven proton scaling laws and new paths towards energy increase. *Nature Physics*, 2(1):48–54, 2005.

[23] O Tresca, DC Carroll, and XH Yuan. Controlling the properties of ultraintense laser proton sources using transverse refluxing of hot electrons in shaped mass-limited targets. *Plasma Physics and Controlled Fusion*, 105008, 2011.

[24] S. Buffechoux, J. Psikal, M. Nakatsutsumi, L. Romagnani, a. Andreev, K. Zeil, M. Amin, P. Antici, T. Burris-Mog, a. Compant-La-Fontaine, E. DHumières, S. Fourmaux, S. Gaillard, F. Gobet, F. Hannachi, S. Kraft, a. Mancic, C. Plaisir, G. Sarri, M. Tarisien, T. Toncian, U. Schramm, M. Tampo, P. Audebert, O. Willi, T. Cowan, H. Pépin, V. Tikhonchuk, M. Borghesi, and J. Fuchs. Hot Electrons Transverse Refluxing in Ultraintense Laser-Solid Interactions. *Physical Review Letters*, 105(1):1–5, 2010.

[25] P. McKenna, A .P. L. Robinson, D. Neely, M. Desjarlais, D. Carroll, M. Quinn, X. Yuan, C. Brenner, M. Burza, M. Coury, P. Gallegos, R. Gray,

K. Lancaster, Y. Li, X. Lin, O. Tresca, and C.-G. Wahlström. Effect of Lattice Structure on Energetic Electron Transport in Solids Irradiated by Ultraintense Laser Pulses. *Physical Review Letters*, 106(18):1–4, 2011.

[26] Teresa Bartal, Mark E. Foord, Claudio Bellei, Michael H. Key, Kirk a. Flippo, Sandrine a. Gaillard, Dustin T. Offermann, Pravesh K. Patel, Leonard C. Jarrott, Drew P. Higginson, Markus Roth, Anke Otten, Dominik Kraus, Richard B. Stephens, Harry S. McLean, Emilio M. Giraldez, Mingsheng S. Wei, Donald C. Gautier, and Farhat N. Beg. Focusing of short-pulse high-intensity laser-accelerated proton beams. *Nature Physics*, 8(2):139–142, 2011.

[27] L Robson, PT Simpson, and RJ Clarke. Scaling of proton acceleration driven by petawatt laser plasma interactions. *Nature Physics*, 3(1):58–62, 2006.

[28] P. McKenna, D.C. Carroll, O. Lundh, F. Nürnberg, K. Markey, S. Bandyopadhyay, D. Batani, R.G. Evans, R. Jafer, S. Kar, D. Neely, D. Pepler, M.N. Quinn, R. Redaelli, M. Roth, C.-G. Wahlström, X.H. Yuan, and M. Zepf. Effects of front surface plasma expansion on proton acceleration in ultraintense laser irradiation of foil targets. *Laser and Particle Beams*, 26(04):591, 2008.

[29] D Batani, R Jafer, M Veltcheva, R Dezulian, O Lundh, F Lindau, a Persson, K Osvay, C-G Wahlström, D C Carroll, P McKenna, a Flacco, V Malka, Home Search, Collections Journals, About Contact, My Iopscience, New J Phys, and I P Address. Effects of laser prepulses on laser-induced proton generation. *New Journal of Physics*, 12(4):045018, 2010.

[30] A. P. L. Robinson, M Zepf, S Kar, R G Evans, C Bellei, Home Search, Collections Journals, About Contact, My Iopscience, New J Phys, and I P Address. Radiation pressure acceleration of thin foils with circularly polarized laser pulses. *New Journal of Physics*, 10(1):013021, 2008.

[31] S. Kar, K. Kakolee, B. Qiao, a. Macchi, M. Cerchez, D. Doria, M. Geissler, P. McKenna, D. Neely, J. Osterholz, R. Prasad, K. Quinn, B. Ramakrishna,

G. Sarri, O. Willi, X. Yuan, M. Zepf, and M. Borghesi. Ion Acceleration in Multispecies Targets Driven by Intense Laser Radiation Pressure. *Physical Review Letters*, 109(18):185006, 2012.

[32] L. V. Keldysh. Ionisation in the field of a strong electromagnetic wave. *Sov. Phys. JETP*, 20(1307), 1965.

[33] O. Lundh, F. Lindau, a. Persson, C.-G. Wahlström, P. McKenna, and D. Batani. Influence of shock waves on laser-driven proton acceleration. *Physical Review E*, 76(2):026404, 2007.

[34] A. R. Bell, F. N. Beg, Z. Chang, A. E. Dangor, C. N. Danson, C. B. Edwards, A. P. Fews, M. H. R. Hutchinson, S. Luan, P. Lee, P. A. Norreys, R. A. Smith, P. F. Taday, and F. Zhou. Observation of plasma confinement in picosecond laser-plasma interactions. *Phys. Rev. E*, 48:2087–2093, 1993.

[35] P Gibbon. *Short Pulse Laser Interactions With Matter: An Introduction*. Imperial College Press, 2005.

[36] F Brunel. Not-so-resonant, resonant absorption. *Physical Review Letters*, 59(1):6–9, 1987.

[37] H Alfvén. On the motion of cosmic rays in interstellar space. *Physical Review*, (5), 1939.

[38] J. Davies. Alfvén limit in fast ignition. *Physical Review E*, 69(6):065402, 2004.

[39] AR Bell and JR Davies. Fast-electron transport in high-intensity short-pulse laser-solid experiments. *Plasma Physics and Controlled Fusion*, 653:1–8, 1997.

[40] K. Akli, M. Storm, M. McMahon, S. Jiang, V. Ovchinnikov, D. Schumacher, R. Freeman, G. Dyer, and T. Ditmire. Time dependence of fast electron beam divergence in ultraintense laser-plasma interactions. *Physical Review E*, 86(2):026404, 2012.

[41] B Bezzerides, SJ Gitomer, and DW Forslund. Randomness, Maxwellian Distributions, and Resonance Absorption. *Physical Review Letters*, 44(10):651–654, 1980.

[42] CD Chen, PK Patel, and DS Hey. Bremsstrahlung and K-alpha fluorescence measurements for inferring conversion efficiencies into fast ignition relevant hot electrons. *Physics of Plasmas*, 16(8):082705, 2009.

[43] F. N. Beg, A. R. Bell, A. E. Dangor, C. N. Danson, A. P. Fews, M. E. Glinsky, B. A. Hammel, P. Lee, P. A. Norreys, and M. Tatarakis. A study of picosecond lasersolid interactions up to 1019 W cm2. *Physics of Plasmas*, 4(2):447, 1997.

[44] S.C. Wilks and W.L. Kruer. Absorption of ultrashort, ultra-intense laser light by solids and overdense plasmas. *IEEE Journal of Quantum Electronics*, 33(11):1954–1968, 1997.

[45] A. Link, R. R. Freeman, D. W. Schumacher, and L. D. Van Woerkom. Effects of target charging and ion emission on the energy spectrum of emitted electrons. *Physics of Plasmas*, 18(5):053107, 2011.

[46] Y. Sentoku, T. E. Cowan, a. Kemp, and H. Ruhl. High energy proton acceleration in interaction of short laser pulse with dense plasma target. *Physics of Plasmas*, 10(5):2009, 2003.

[47] P. McKenna, D. Carroll, R. Clarke, R. Evans, K. Ledingham, F. Lindau, O. Lundh, T. McCanny, D. Neely, a.P.L. Robinson, L. Robson, P. Simpson, C.-G. Wahlström, and M. Zepf. Lateral Electron Transport in High-Intensity Laser-Irradiated Foils Diagnosed by Ion Emission. *Physical Review Letters*, 98(14):145001, 2007.

[48] P McKenna, F Lindau, O Lundh, D C Carroll, R J Clarke, K W D Ledingham, T McCanny, D Neely, a P L Robinson, L Robson, P T Simpson, C-G Wahlström, and M Zepf. Low- and medium-mass ion acceleration driven by

petawatt laser plasma interactions. *Plasma Physics and Controlled Fusion*, 49(12B):B223–B231, 2007.

[49] M. Hegelich, S. Karsch, G. Pretzler, D. Habs, K. Witte, W. Guenther, M. Allen, a. Blazevic, J. Fuchs, J. Gauthier, M. Geissel, P. Audebert, T. Cowan, and M. Roth. MeV Ion Jets from Short-Pulse-Laser Interaction with Thin Foils. *Physical Review Letters*, 89(8):085002, 2002.

[50] JC Kieffer, P Audebert, M Chaker, and JP Matte. Short-pulse laser absorption in very steep plasma density gradients. *Physical Review Letters*, 62(7):760–763, 1989.

[51] D. D. Meyerhofer, H. Chen, J. A. Delettrez, B. Soom, S. Uchida, and B. Yaakobi. Resonance absorption in high-intensity contrast, picosecond laser-plasma interactions. *Physics of Fluids B: Plasma Physics*, 5(7):2584, 1993.

[52] U Teubner, I Uschmann, P Gibbon, D Altenbernd, E Förster, T Feurer, W Theobald, R Sauerbrey, G Hirst, Mh Key, J Lister, and D Neely. Absorption and hot electron production by high intensity femtosecond uv-laser pulses in solid targets. *Physical Review. E*, 54(4):4167–4177, 1996.

[53] SC Wilks, WL Kruer, and M Tabak. Absorption of ultra-intense laser pulses. *Physical Review Letters*, 69(9):1383–1386, 1992.

[54] G Malka and Jl Miquel. Experimental Confirmation of Ponderomotive-Force Electrons Produced by an Ultrarelativistic Laser Pulse on a Solid Target. *Physical Review Letters*, 77(1):75–78, 1996.

[55] K. Wharton, S. Hatchett, S. Wilks, M. Key, J. Moody, V. Yanovsky, A. Offenberger, B. Hammel, M. Perry, and C. Joshi. Experimental Measurements of Hot Electrons Generated by Ultraintense (1019 W/cm2) Laser-Plasma Interactions on Solid-Density Targets. *Physical Review Letters*, 81(4):822–825, 1998.

[56] M.I. Santala, M Zepf, I Watts, F.N. Beg, E Clark, M Tatarakis, K Krushelnick, A.E Dangor, T. McCanny, I Spencer, R.P. Singhal, K.W. Ledingham, S.C. Wilks, A.C. Machacek, J.S. Wark, R Allott, R.J. Clarke, and P.A. Norreys. Effect of the plasma density scale length on the direction of fast electrons in relativistic laser-solid interactions. *Physical Review Letters*, 84(7):1459–62, 2000.

[57] R. Kodama, K. Mima, K. a. Tanaka, Y. Kitagawa, H. Fujita, K. Takahashi, a. Sunahara, K. Fujita, H. Habara, T. Jitsuno, Y. Sentoku, T. Matsushita, T. Miyakoshi, N. Miyanaga, T. Norimatsu, H. Setoguchi, T. Sonomoto, M. Tanpo, Y. Toyama, and T. Yamanaka. Fast ignitor research at the Institute of Laser Engineering, Osaka University. *Physics of Plasmas*, 8(5):2268, 2001.

[58] Y. Ping, R. Shepherd, B. Lasinski, M. Tabak, H. Chen, H. Chung, K. Fournier, S. Hansen, a. Kemp, D. Liedahl, K. Widmann, S. Wilks, W. Rozmus, and M. Sherlock. Absorption of Short Laser Pulses on Solid Targets in the Ultrarelativistic Regime. *Physical Review Letters*, 100(8):085004, 2008.

[59] D. F. Cai, Y. Q. Gu, Z. J. Zheng, T. S. Wen, S. T. Chunyu, Z. B. Wang, and X. D. Yang. Experimental study for angular distribution of the hot electrons generated by femtosecond laser interaction with solid targets. *Physics of Plasmas*, 10(8):3265, 2003.

[60] Y. T. Li, X. H. Yuan, M. H. Xu, Z. Y. Zheng, Z. M. Sheng, M. Chen, Y. Y. Ma, W. X. Liang, Q. Z. Yu, Y. Zhang, F. Liu, Z. H. Wang, Z. Y. Wei, W. Zhao, Z. Jin, and J. Zhang. Observation of a Fast Electron Beam Emitted along the Surface of a Target Irradiated by Intense Femtosecond Laser Pulses. *Physical Review Letters*, 96(16):2–5, 2006.

[61] H. Habara, K. Adumi, T. Yabuuchi, T. Nakamura, Z. Chen, M. Kashihara, R. Kodama, K. Kondo, G. Kumar, L. Lei, T. Matsuoka, K. Mima, and

K. Tanaka. Surface Acceleration of Fast Electrons with Relativistic Self-Focusing in Preformed Plasma. *Physical Review Letters*, 97(9):1–4, 2006.

[62] T Nakamura, S Kato, H Nagatomo, and K Mima. Surface-Magnetic-Field and Fast-Electron Current-Layer Formation by Ultraintense Laser Irradiation. *Physical Review Letters*, 93(26):1–4, 2004.

[63] A. A. Andreev, K. Yu. Platonov, T. Okada, and S. Toraya. Nonlinear absorption of a short intense laser pulse in a nonuniform plasma. *Physics of Plasmas*, 10(1):220, 2003.

[64] T. Ma, H. Sawada, P. Patel, C. Chen, L. Divol, D. Higginson, a. Kemp, M. Key, D. Larson, S. Le Pape, a. Link, a. MacPhee, H. McLean, Y. Ping, R. Stephens, S. Wilks, and F. Beg. Hot Electron Temperature and Coupling Efficiency Scaling with Prepulse for Cone-Guided Fast Ignition. *Physical Review Letters*, 108(11):115004, 2012.

[65] Lihua Cao, Yuqiu Gu, Zongqing Zhao, Leifeng Cao, Wenzhong Huang, Weimin Zhou, X. T. He, Wei Yu, and M. Y. Yu. Enhanced absorption of intense short-pulse laser light by subwavelength nanolayered target. *Physics of Plasmas*, 17(4):043103, 2010.

[66] P Kumar Singh, G Chatterjee, Amit D. Lad, A Adak, S Ahmed, M. Khorasaninejad, M. M. Adachi, K. S. Karim, S. S. Saini, a. K. Sood, and G. Ravindra Kumar. Efficient generation and guiding of megaampere relativistic electron current by silicon nanowires. *Applied Physics Letters*, 100(24):244104, 2012.

[67] A. Henig, D. Kiefer, K. Markey, D. Gautier, K. Flippo, S. Letzring, R. Johnson, T. Shimada, L. Yin, B. Albright, K. Bowers, J. Fernández, S. Rykovanov, H.-C. Wu, M. Zepf, D. Jung, V. Liechtenstein, J. Schreiber, D. Habs, and B. Hegelich. Enhanced Laser-Driven Ion Acceleration in the Relativistic Transparency Regime. *Physical Review Letters*, 103(4):1–4, 2009.

[68] L. Yin, B. J. Albright, B. M. Hegelich, K. J. Bowers, K. a. Flippo, T. J. T. Kwan, and J. C. Fernandez. Monoenergetic and GeV ion acceleration from

the laser breakout afterburner using ultrathin targets. *Physics of Plasmas*, 14(5):056706, 2007.

[69] S Palaniyappan, B. M Hegelich, H. C Wu, D Jung, D C. Gautier, Lin Yin, B. J. Albright, R P. Johnson, T Shimada, S Letzring, D T. Offermann, J Ren, C Huang, R Hörlein, B Dromey, J C. Fernandez, and R C. Shah. Dynamics of relativistic transparency and optical shuttering in expanding overdense plasmas. *Nature Physics*, 8(10):763–769, 2012.

[70] M Roth, D Jung, K Falk, N Guler, O Deppert, M Devlin, A Favalli, J Fernandez, D Gautier, M Geissel, R Haight, C E Hamilton, B M Hegelich, R P Johnson, F Merrill, G Schaumann, K Schoenberg, M Schollmeier, T Shimada, T Taddeucci, J L Tybo, F Wagner, S A Wender, C H Wilde, and G A Wurden. Bright Laser-Driven Neutron Source Based on the Relativistic Transparency of Solids. *Physical Review Letters*, 044802(January):1–5, 2013.

[71] D. Kiefer, A. Henig, D. Jung, D. C. Gautier, K. a. Flippo, S. a. Gaillard, S. Letzring, R. P. Johnson, R. C. Shah, T. Shimada, J. C. Fernández, V. Kh. Liechtenstein, J. Schreiber, B. M. Hegelich, and D. Habs. First observation of quasi-monoenergetic electron bunches driven out of ultra-thin diamond-like carbon (DLC) foils. *The European Physical Journal D*, 55(2):427–432, 2009.

[72] B. Dromey, S. Kar, M. Zepf, and P. Foster. The plasma mirror A subpicosecond optical switch for ultrahigh power lasers. *Review of Scientific Instruments*, 75(3):645, 2004.

[73] A. Dubietis, R. Butkus, and A.P. Piskarskas. Trends in chirped pulse optical parametric amplification. *IEEE Journal of Selected Topics in Quantum Electronics*, 12(2):163–172, 2006.

[74] D. C. Carroll. *Laser Driven Ion Acceleration: Source Optimisation and Optical Control*. PhD thesis, University of Strathclyde, 2008.

[75] D.C. Carroll, P. Brummitt, D. Neely, F. Lindau, O. Lundh, C.-G. Wahlström, and P. McKenna. A modified Thomson parabola spectrometer for high resolution multi-MeV ion measurementsApplication to laser-driven ion acceleration. *Nuclear Instruments and Methods in Physics Research Section A: Accelerators, Spectrometers, Detectors and Associated Equipment*, 620(1):23–27, 2010.

[76] R. Prasad, D. Doria, S. Ter-Avetisyan, P.S. Foster, K.E. Quinn, L. Romagnani, C.M. Brenner, J.S. Green, P. Gallegos, M.J.V. Streeter, D.C. Carroll, O. Tresca, N. Dover, C.a.J. Palmer, J. Schreiber, D. Neely, Z. Najmudin, P. McKenna, M. Zepf, and M. Borghesi. Calibration of Thomson paraboLaMCP assembly for multi-MeV ion spectroscopy. *Nuclear Instruments and Methods*, 623(2):712–715, 2010.

[77] D. Doria, S. Kar, and K. Kakolee. Calibration of Image Plate response to energetic Carbon ions. *CLF Annual Report*, 2010.

[78] M N Quinn, X H Yuan, X X Lin, D C Carroll, O Tresca, R J Gray, M Coury, C Li, Y T Li, C M Brenner, a P L Robinson, D Neely, B Zielbauer, B Aurand, J Fils, T Kuehl, and P McKenna. Refluxing of fast electrons in solid targets irradiated by intense, picosecond laser pulses. *Plasma Physics and Controlled Fusion*, 53(2):025007, 2011.

[79] R Benattar, C Popovics, and R Sigel. Polarized light interferometer for laser fusion studies. *The Review of Scientific Instruments*, 50(12):1583, 1979.

[80] http://t1web.lanl.gov/doc/SESAME_3Ddatabase_1992.html.

[81] G J Pert. Algorithms for the Self-Consistent Generation Magnetic Fields in Plasmas. *Journal of Computational Physics*, 43:111–163, 1981.

[82] J.J. MacFarlane, I.E. Golovkin, and P.R. Woodruff. HELIOS-CR A 1-D radiation-magnetohydrodynamics code with inline atomic kinetics modeling. *Journal of Quantitative Spectroscopy and Radiative Transfer*, 99(1-3):381–397, 2006.

[83] Y. Sentoku, K. Mima, H. Ruhl, Y. Toyama, R. Kodama, and T. E. Cowan. Laser light and hot electron micro focusing using a conical target. *Physics of Plasmas*, 11(6):3083, 2004.

[84] X H Yuan, Y T Li, M H Xu, Z Y Zheng, Q Z Yu, W X Liang, Y Zhang, F Liu, Jens Bernhardt, S J Wang, Z H Wang, W J Ling, Z Y Wei, W Zhao, and J Zhang. Effective fast electron acceleration along the target surface. *Opt. Express*, 16(1):81–86, 2008.

[85] R. J. Gray, X. H. Yuan, D. C. Carroll, C. M. Brenner, M. Coury, M. N. Quinn, O. Tresca, B. Zielbauer, B. Aurand, V. Bagnoud, J. Fils, T. Kuhl, X. X. Lin, C. Li, Y. T. Li, M. Roth, D. Neely, and P. McKenna. Surface transport of energetic electrons in intense picosecond laser-foil interactions. *Applied Physics Letters*, 99(17):171502, 2011.

[86] http://physics.nist.gov/PhysRefData/Star/Text/ESTAR.html.

[87] P M Nilson, W Theobald, J F Myatt, C Stoeckl, M Storm, J D Zuegel, R Betti, D D Meyerhofer, and T C Sangster. Bulk heating of solid-density plasmas during high-intensity-laser plasma interactions. *Phys. Rev. E*, 79(1):16406, 2009.

[88] I Musgrave, W Shaikh, M Galimberti, Alexis Boyle, Cristina Hernandez-Gomez, Kate Lancaster, and Robert Heathcote. Picosecond optical parametric chirped pulse amplifier as a preamplifier to generate high-energy seed pulses for contrast enhancement. *Applied Optics*, 49(33):6558–62, 2010.

[89] J R Davies. Laser absorption by overdense plasmas in the relativistic regime. *Plasma Physics and Controlled Fusion*, 51(1):014006, 2009.

[90] Erik Lefebvre and Guy Bonnaud. Nonlinear electron heating in ultrahigh-intensity-laserplasma interaction. *Physical Review E*, 55(1):1011–1014, 1997.

[91] W Kruer. *The Physics Of Laser Plasma Interactions*. Frontiers in Physics. Westview Press, 2003.

[92] D. W. Schumacher, G. E. Kemp, a. Link, R. R. Freeman, and L. D. Van Woerkom. The shaped critical surface in high intensity laser plasma interactions. *Physics of Plasmas*, 18(1):013102, 2011.

[93] D. Neely, P. Foster, A. Robinson, F. Lindau, O. Lundh, A. Persson, C.-G. Wahlstrom, and P. McKenna. Enhanced proton beams from ultrathin targets driven by high contrast laser pulses. *Applied Physics Letters*, 89(2):021502, 2006.

[94] M Kaluza, J Schreiber, M I K Santala, G D Tsakiris, K Eidmann, J Meyer-ter Vehn, and K J Witte. Influence of the Laser Prepulse on Proton Acceleration in Thin-Foil Experiments. *Physical Review letters*, 93(4):45003, 2004.

[95] Hong-bo Cai, Kunioki Mima, Atsushi Sunahara, Tomoyuki Johzaki, Hideo Nagatomo, Shao-ping Zhu, and X. T. He. Prepulse effects on the generation of high energy electrons in fast ignition scheme. *Physics of Plasmas*, 17(2):023106, 2010.

[96] R. H. H. Scott, F. Perez, J. J. Santos, C. P. Ridgers, J. R. Davies, K. L. Lancaster, S. D. Baton, Ph. Nicolai, R. M. G. M. Trines, A. R. Bell, S. Hulin, M. Tzoufras, S. J. Rose, and P. A. Norreys. A study of fast electron energy transport in relativistically intense laser-plasma interactions with large density scalelengths. *Physics of Plasmas*, 19(5):053104, 2012.

[97] T. Esirkepov, M. Borghesi, S. Bulanov, G. Mourou, and T. Tajima. Highly Efficient Relativistic-Ion Generation in the Laser-Piston Regime. *Physical Review Letters*, 92(17):175003, 2004.